GERMANIUM-SILICON RATIOS AS A RECORD OF MID MIOCENE SILICA FLUXES TO THE OCEANS

A Thesis

Presented to the Faculty of the Graduate School

of Cornell University

In Partial Fulfillment of the Requirements for the Degree of

Master of Science

by

Jinyi Li

August 2019

ABSTRACT

A warm climate interval from 17 to 14.8 Ma is known as the Mid Miocene Climatic Optimum (MMCO). This interval was followed by a progressive cooling that continued to the Pleistocene. Several isotopic tracers indicate global climate and possibly weathering changes during the mid-Miocene. Germanium-silicon (Ge/Si) ratios are fractionated by silicate weathering processes and so can be an effective tracer of weathering intensity, and one potential consequence of a warm climate is increased silicate weathering intensity. We present a Ge/Si ratio record of 81 samples from IODP U1337A for ~12-18 Ma. The Ge/Si data for this interval do not show an overall temporal trend, but they are higher than present day ratio in seawater. The data show considerable scatter outside of analytical precision, and this scatter data may be in part result from diagenetic alteration. With a box model of the oceanic balance of Ge/Si and δ^7Li we find that mid-Miocene weathering fluxes and weathering intensity were likely higher than at present, consistent with a warmer climate at that time.

BIOGRAPHICAL SKETCH

Jinyi Li, was born and grew up in a coastal city in China. She began to get interested in chemistry in High School. Both her parents work in a national oil company, influenced by her parents, she decided to study geology in China University of Petroleum. In the senior year of her college, she planned to pursue further education and stepped her feet over to the other side of the earth. She acquired her first Master of Engineering degree at Cornell University in 2016, and continued to pursue her second Master degree in the same year. In her first Master degree, she worked on a project of special application of Petrel and Eclipse software. She developed a manual on generating streamlines of fluid in the ground. In the second Master degree, she transitioned her interest to biogeochemistry and started doing research on paleoceanography. Her research focused on analyzing Ge/Si ratio of diatoms in Mid Miocene and using it as a tracer for continental weathering.

ACKNOWLEDGMENTS

I would first like to thank my advisor Professor Louis A. Derry for consistently providing me support, encouraging me to explore the geochemistry world and steering me to the right direction in my research. Second I would like to thank Professor Ian Hewson for being on my committee and sharing his biological knowledge with me. Next I would like to thank my lab mates Katherine Grant, Alida Perez Fodich and Andrés Aguirre. They taught me how to do the lab work and help me measure samples. Also thanks to other people who helped me in the lab. A lot of thanks to my parents for their unconditional love and support. Last but not least, I would like to thank IODP for their amazing work.

TABLE OF CONTENTS

CHAPTER 1

GLOBAL GE AND SI CYCLE

The Global Silica Cycle

Silica is transported between land, atmosphere and ocean reservoirs through several paths. Weathering provides the source of silica, in dissolved and particulate form. Weathering produces secondary clay minerals, opal or amorphous silica, and dissolved silica. These weathering products can be transported by rivers and streams where additional modifications can take place prior to reaching the oceans. Rivers provide the largest Si contribution to the ocean. Dissolved Si produced by weathering is also transported as groundwater, which can end up in the ocean as well. The river Si flux is controlled by weathering factors like temperature, rainfall, vegetation, lithology, glaciation and erosion rate. Biological processes also have an impact on the concentration of dissolved Si in the river, with uptake by diatoms (siliceous algae) and aquatic plants (Sutton et al., 2018).

Weathering and Terrestrial Silica Cycling

The riverine Si flux largely depends on weathering and secondary mineral formation and dissolution. Silica transported from bedrock is either physically eroded or dissolved during weathering process. Total silica export is the sum of transport as sediment (physical erosion) and as dissolved silica (chemical erosion):

$Si(tot) = Si(part) + Si(aq)$

where *Si(tot)* is the total mass of silica exported form a landscape, *Si(part)* is the mass exported as sedimentary particulates, and *Si(aq)* is the mass exported as dissolved silica. The extent to which dissolved Si contributes to the total weathering flux can be described by "weathering intensity". Weathering intensity is the fraction of Si dissolved from silicate bedrock during weathering (Murnane and Stallard, 1990). Solutes derived from carbonates and evaporites are not included because they can weather congruently. The greater fraction of silica dissolved, the higher the weathering intensity will be (Froelich et al., 1992). During weathering and erosion of primary bedrock some cations are dissolved and exported in the solution, some are dissolved and partitioned into secondary minerals by neoformation and the rest is very resistant and remain in primary minerals (Lugolobi et al., 2010). Only a small fraction of silica is transported to the ocean in dissolved form. Weathering reactions can be divided into two types in terms of the product phase. One is "congruent weathering" and another is "incongruent weathering". For carbonates, weathering reactions yield no solid phase, carbonate minerals dissolve completely, and this is referred to as *congruent weathering*. For weathering of alumino-silicates, primary minerals are transformed to secondary minerals and solutes. The formation of both a secondary sold phase and a dissolved phase is called *incongruent weathering*. It is useful to conceptualize two weathering regimes: "weathering limited" and "transport limited" (Stallard, 1987; Murnane et al., 1990). *Weathering limited* regimes occur when physical erosion rates are much higher than chemical weathering rates. In this case, weathering tends to be more incongruent, because the regolith has limited time to react within the weathering zone. Dissolution

of primary minerals is limited by chemical reaction rates, and most erosion products stay as primary minerals, thus weathering intensity is low. Weathering-limited denudation happens in landscapes with steep slopes and only a thin layer of soil is developed in this kind of area. The total Si flux is high, but dominantly in the particulate form. A *transport limited* regime occurs when chemical weathering rates are high relative to the rate of erosion that removes weathered material. This weathering regime usually occurs in area with low topographic gradients, and thick soils can develop with time. The chemical weathering rate is limited because of the limited supply of fresh material to the weathering zone. Both Si flux and Si concentration are low, whereas weathering intensity is high. Weathering is under these conditions more often approaches congruent.

Vegetation plays an important role in terrestrial Si cycle. Dissolved Si can be taken up by plants and deposit in stems, leaves, and roots to help support the plant structure. Most biogenic Si in plants is in the form of small opal bodies called “phytoliths” (Conley, 2002). The concentration of Si in the plants ranges from 1% up to 10% (Epstein, 1994). Decomposition of plant litter releases phytoliths to soils. Soil environments are commonly undersaturated with respect to opal, so the dissolution of biogenic silica (phytoliths) is an important source of dissolved Si to soils. Some silica in the soil reservoir can recycled as a plant nutrient, while some is stored in the soil pool. The Si stored by terrestrial vegetation is 60-200 Tmol/year (Struyf and Conley, 2012). Under appropriate hydrologic conditions dissolved silica is flushed from the soil to ground waters and stream waters. Not only terrestrial ecosystems but aquatic ecosystems have

an impact on Si flux to ocean. Diatom and siliceous sponges have been found in soil and terrestrial sediments (Clarke, 2003). Freshwater diatoms, siliceous sponges and plants that live in freshwater also take dissolved Si from river water. Diatom and aquatic plant production have a crucial impact on Si cycle. During the growing season, the Si concentration in stream water is lower than at other times of year (Opfergelt et al., 2011). Phytolith and diatom dissolution also can contribute Si to fresh waters. Not all biogenic opal will dissolve in rivers, some will be deposited and buried in sediments. Groundwater springs also provide Si to the freshwater system. Microbes, mainly bacteria, also have an impact on the solubility of Si in coastal region, due to their ability to remove organic matter coating from diatom frustules. Human activity is an important factor as well. As urban development can change landscapes and hydrologic flow paths, base flow and runoff fluxes are affected (Struyf et al., 2012). Anthropogenic activities also tend to increase erosion rates as well, which has an impact on terrestrial and oceanic Si cycle. More soil erosion tends to remove the biogenic Si stored in soil and carry it to the ocean. Durr et al. (2009) estimated global silica export from terrestrial landscapes at 371 Mt/yr of dissolved Si and 8835 Mt/yr of suspended particulate Si, or 13.3 Tmol/yr of dissolved Si and 315.5 Tmol/yr of particulate Si, with Si(aq) representing 4.0% of total Si export. Some of the river flux of Si is sequestered in coastal and estuarine regions, primarily by biological uptake (Struyf and Conley, 2012). The overall flux of silica to the oceans from rivers and groundwater discharge is estimated to be ca. 7.9±2.0 Tmol/yr (Treguer and De La Rocha, 2013)

Other Sources of Dissolved Silica to the Ocean

Particulate silica such as primary minerals, clays and biogenic opal can be carried by wind as mineral aerosol ("dust") over long distances prior to deposition on land or in the oceans. Most of the dust comes from two places. One is the Sahara Desert that supplies dust to the North Atlantic and Mediterranean Sea, the other is central Asian (especially the Gobi Desert, Taklamakan, and Loess Plateau) dust blown into western Pacific. The dust contains both lithogenic and biogenic silica. The amount of dust is much smaller than river loads, however, the significance of aerosol input is pronounced in the center of open oceans. The total dust deposition can contribute 2.8~4.6 Tmol/year of Si (Tegen et al., 2006). However, only a small amount of dust is dissolved in ocean. The solubility of dust varies greatly depending on several factors such as aerosol source, suspended particle concentration and atmospheric processing which particles have experienced (Baker, 2006). Saharan dust is enriched in quartz whereas Gobi Desert dust has more feldspar. The quartz-rich dust has very low solubility of 0.02%-1.1% (Baker, 2006), while dust rich in feldspar and biogenic Si have higher solubility of ~10% (Harrison, 2000). The dissolved Si flux from dust is estimated to be 0.5±0.5 Tmol/year based on the dust fluxes and dissolution rates (Treguer, 2013).

Another important input of Si comes from hydrothermal reactions near mid ocean ridges. There are two types of hydrothermal fluids which react with submarine basalt. One is axial hydrothermal fluids, the other is off-axis hydrothermal fluids. Mid-ocean ridges

have a layered structure. The surface layer is pelagic sediments with underlying basaltic rocks, and below this is a sheeted dike complex. Beneath are the gabbroic rocks formed by slow cooling of magma. At the ridge, the cold water infiltrates toward the magma chamber and is heated to ~350℃. High-temperature hydrothermal fluids exchange with basalt resulting in a release of dissolved Si. The convection is driven by magmatic-source heat advected to the upper crust. The fluid temperature can reach 350-400℃. This high-temperature alteration occurs mainly in the sheeted dike and plutonic section (Elderfield & Schultz, 1996). The high-temperature hydrothermal Si flux is 0.55±0.25 Tmol/year (Elderfield & Schultz, 1996). Low-temperature alteration of basalt occurs at ridge flanks involving diffusive exchange and fluid flow. Seawater enters the basaltic basement and is warmed up from 2℃ to 10-50 ℃ (Wheat and McManus, 2005). Seawater reacts with basalt and releases Si to the basement fluid. Si concentration is increased to supersaturation and can be precipitated to form clays and secondary quartz or amorphous silica. As seawater exits from the basaltic basement, it can interact with the overlying sediments. The pore water in sediment layer contains high concentrations of dissolved Si and Ge. Concentrations tend to increase downwards due to the increasing temperature (Wheat and McManus, 2005). The dissolved Si and Ge in pore water diffuse into the basement fluid and the concentration drops drastically at the sediment-basement interface. The precipitation of quartz happens through the entire process and buffers the Si concentration of basement fluid (Wheat et al., 2005). Reacted fluids can emerge at spring vents and return high concentrations Si to seawater. Si concentrations of high-temperature fluid is 16-23 mmol/kg, with a Ge concentration of 150-280 nmol/kg for 350℃ (Mortlock et al., 1993). The Ge/Si ratio of this ridge flux is

9±6μmol/mol (Wheat and McManus, 2005). In contrast, the low-temperature hydrothermal flux has an average Si concentration of 50-100 mmol/kg and Ge concentration of 120-250 nmol/kg (Wheat and McManus, 2008). This generates a Ge/Si ratio of 25±24 μmol/mol. The overall Si flux from hydrothermal vents is not well-constrained, and an estimation from Ge/Si and Ge isotopes budgets is 0.6±0.4 Tmol/year (Treguer and De La Rocha, 2013).

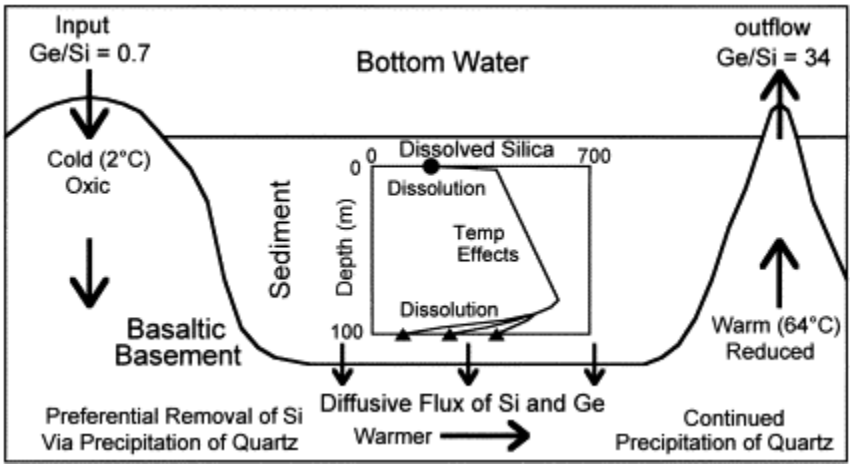

Figure 1.1 Schematic graph of hydrothermal alteration, Wheat and McManus, 2005

Diagenesis of marine sediment plays an important role in the silica cycle. Marine sediments contain lithogenic material and biogenic silica. Dissolution of biogenic silica occurs during early diagenesis of marine sediments and releases Si to pore water. Dissolved Si accumulates in the pore space and gradually diffuses upwards to the ocean, establishing a steady state profile (Wollast and Mackenzie, 1983). Batch experiments of dissolution of basaltic particles in seawater indicates significant amount of Si and Sr can be released in months (Oelkers et al., 2011). Some studies show that 1-3% sediments along ocean margins can dissolve congruently as deduced from a neodymium isotope budget (Jeandel, et al., 2011). The isotopic analysis of Nd, Si and Fe from coastal regions suggests the dissolved elements are lithogenic (Lacan and Jeandel, 2005). Jeandel et al (2011) considered a large range of sediment composition, and estimated that 0.7-5.4 Tmol of dissolved Si are released to ocean annually from this "boundary layer" process. Treguer and De La Rocha (2013) estimated that the dissolved Si input to the oceans from marine sediment diagenesis is 1.9±0.7 Tmol/year.

Internal Biogeochemical Cycling

Biological uptake of silica by siliceous organisms followed by their burial is the largest sink for oceanic silica cycle. Dissolved silica in the form of silicic acid (H_4SiO_4) is taken up by diatoms and radiolarians to build their frustules. Siliceous sponges take up silica to grow spicules. After they die, they can sink to the seafloor. The sinking flux of biogenic particulate silica is sometimes called "opal rain". Most of sinking particulate

silica will be released to the water column by dissolution, and additional dissolution happens on the water-sediment interface, only ~3% of biological opal is preserved in sediments (Treguer et al., 2013).

Biogenic silica production in the oceans is around 240 Tmol/year (Treguer, 1995), and the terrestrial phytolith production is slightly lower, 60-200 Tmol/year (Conley,2002).

Reverse weathering

During early diagenesis, dissolved Si can react with other elements (Mg, K, Al and F) and form authigenic clays; this process is known as *reverse weathering*. Reverse weathering reactions requires the participation of Al and Fe in the form of oxides or oxyhydroxides. The reactants come from dissolution of biogenic silica, highly weathered aluminosilicates and other sediments. Reverse weathering removes dissolved silica with Al and Fe oxy-hydroxides to form alumino-silicate minerals, and this process is especially active in deltaic regions (Treguer, 2013). Some biogenic silica buried in deltaic region is rapidly converted to authigenic clays under certain circumstances, which includes reactive Si, mobilization of Fe and Al in early diagenesis and incorporation of other elements such as K, Mg, F, Li and etc. In high sedimentation rate environment, biogenic silica particles are coated with Al and Fe, and diatom frustules are filled with pyrite, which provides essential conditions for the formation of aluminosilicates. This process has been

successfully replicated in laboratory experiments by Michalopoulos and Aller (1995). The schematic reaction can be summarized as:

1.1) $6.47SiO_2 + 4.8Al(OH)_3 + 0.9Fe(OH)_3 + 0.225C_{org} + 0.96K^+ +$
$0.39Mg^{2+} + 0.05Na^+ + 0.03Ti(OH)_4 + 1.81HCO_3^- \rightarrow$
$(K_{0.96}Na_{0.05}) + (Al_{3.27}Fe^{2+}_{0.90}Mg_{0.39}Ti_{0.03})(Si_{6.47}Al_{1.53})O_{20}(OH)_4 +$
$2.035CO_2 + 7.52H_2O$

(Michalopoulos and Aller, 1995)

$6.47SiO_2 + 4.8Al(OH)_3 + 0.9Fe(OH)_3 + 0.225C_{org} + 0.96K^+ + 0.39Mg^{2+}$
$+ 0.05Na^+ + 0.03Ti(OH)_4 + 1.81HCO_3^-$
$\rightarrow (K_{0.96}Na_{0.05}) + (Al_{3.27}Fe^{2+}_{0.90}Mg_{0.39}Ti_{0.03})(Si_{6.47}Al_{1.53})O_{20}(OH)_4$
$+ 2.035CO_2 + 7.52H_2O$

Examples of radiolarians in deep sea sediment (Sayles and Bischoff, 1973; Hein et al., 1979; Cole, 1985; Odin and Frohlich, 1988) and diatoms in nearshore water and saline lakes (van Bennekom and van der Gast, 1976; Badaut and Risacher, 1982) are reported to show intergrowth of authigenic clays. The alteration products are classified into 2 groups: 1) frustules and tests coated with cation-rich aluminosilicates; 2) complete alteration of siliceous frustules to authigenic aluminosilicates. The complete alteration group are composed of: a) biogenic silica locally replaced by aluminosilicates and, b) pseudomorphs consist of authigenic clays and agglutinated sedimentary matrix. Between the end members of completely altered frustules and unaltered diatoms, there is a spectrum of intermediate degrees of transition (Michalopoulos and Aller, 2004). The morphology of diatom frustules can either be preserved or fragmented.

The conversion from fresh diatoms to authigenic aluminosilicates is associated with sulfate reduction, metal reduction and decomposition of organic carbon. The diatom cell provides a microenvironment for sulfate reduction (Michalopolous and Aller, 2003). K^+ and Mg^{2+} are incorporated into authigenic clays and Mg^{2+} will also be taken into carbonates. Other major and minor elements will also be involved in this precipitation process (Sutton et al., 2018). In tropical deltaic environments, the amount of authigenic clays produced is controlled by availability of reactive Si; Al and Fe phases are abundant. In deep sea sediments or carbonate rich sediments, the primary factor is the availability of Al and Fe-oxides. The output flux to reverse weathering has been estimated to be 1.5±0.5 Tmol/year (Treguer and De La Rocha, 2013). The estimate is based on pore water flux of K^+, F^- and Li^+; stoichiometric models of authigenic clay; non-steady-state diagenetic modeling; clay formation rate and composition from experiments; and a specially designed leach procedure to separate clays and biogenic silica (Treguer and De La Rocha, 2013). Reactive Si is a limiting factor during reverse weathering process, thus an estimate of the reactive Si sink is essential to solve for the reverse weathering flux. Laruelle et al. (2009) built a global-scale reactive Si box model to assessment the biogeochemical Si cycle and fluxes. Holland et al. (2005) estimates reverse weathering flux is 20-25% of total river input via K^+, Na^+, HCO_3^- and H_4SiO_4 balancing. The information from different models and experiment are mutually supportive. However, this value is still thought to be underestimated (Sutton et al., 2018). They argue that the Si sink in deltaic and continental margin region is more significant than previously expected. Due to low opal concentration from conventional Si extraction method with

Na_2CO_3, other complex mineral formation that can consume biogenic silica in marine sediments is not taken into consideration. The amount of Si removal may be 2~3 times bigger than that derived from diagenetic models (Rahman et al., 2016).

Other factors affecting Si cycle

The consumption of silica by radiolarians remains uncertain, because not all radiolarians produce a silica skeleton and there is not enough information to estimate how much dissolved Si radiolarians take in (Treguer and De La Rocha, 2013; Takahashi, 1981). The Si flux to sponges is thought to be a missing sink and has been mostly neglected. Recent estimates of the output flux to sponges are 3.6±3.7 Tmol/yr (Maldonado, 2011; Treguer and De La Rocha, 2013). The flux from diatom utilization is better estimated, with a value of 6.3±3.6 Tmol/yr. These estimates take several parameters into account. For some better-known species like diatoms, the production rate has been estimated through box models and stoichiometric calculations (Nelson, 1995). The upper limit of diatom Si flux is estimated from primary production rates in the open ocean and coastal regions. The Si/C ratio of diatom is the key for calculating Si production rate, but this can change with iron availability. Fe deficiency tends to increase Si uptake of diatoms, thus the Si:C ratio will be higher in Fe-limited environment (Hutchins and Bruland, 1998). To get the lower limit of Si production rate, the spatial distribution of silicic acid and deep ocean residence time are considered. Several box models with different surface layer depth and compartments were built to obtain a better idea of silicic acid distribution. The global surface ocean BSi production rate is 200~280 Tmol/yr, but only

~3% is preserved in the sediments (Nelson et al., 1995). The preservation of opal is unevenly distributed. In some areas where diatom opal production is high 15~25% of the annual Si production can be preserved (Nelson et al., 1995). Factors affecting Si preservation include: water depth, surface layer temperature, diatom species composition, frustule morphology, grazer characteristics, aggregate particle formation and trace element chemistry. For other unknown contributors, a rough estimate is derived from the density of some species, the depth of their habitat, and the mean weight of the skeleton of certain species.

Table 1.1 Global Si steady state fluxes

Component	Flux (Tmol Si/ yr)	Uncertainties (Tmol Si/ yr)
Inputs		
Rivers, dissolved Si	6.2	1.8
Rivers, biogenic SI	1.1	0.2
Groundwater	0.6	0.6
Aeolian	0.5	0.5
Hydrothermal	0.6	0.4
Marine sediments	1.9	0.7
Total net inputs	9.4	4.7
Outputs		
Diatoms	6.3	3.6
Sponges	3.6	3.7
Total net outputs	9.9	7.3
Total production	240	40

After Treguer and De La Rocha, 2013, Table 5

Summary of global Si fluxes

The global Si cycle is composed of 3 parts: inputs to the ocean, internal cycling and output fluxes. The input fluxes include riverine dissolved Si mainly from terrestrial weathering, groundwater, aerosols, hydrothermal fluxes, and diagenesis of marine sediments. The internal Si cycling involves both terrestrial ecosystem and marine ecosystem. On land, rock weathering supplies dissolved Si to rivers. Plants, freshwater diatom and aquatic plants will take up dissolved Si from soil and stream water and when they die, Si will be released to the environment and utilized by other plants and siliceous microbes. In the sea, the dissolved Si will be consumed by diatoms, radiolarians and siliceous sponges, and the Si will be released during decomposition and particle settling.

Germanium – silicon ratios (Ge/Si) as a tracer of the silica cycle

Germanium has similar properties and behavior to silica and their general biogeochemical cycles are closely linked. Ge and Si are both in the IV-A group of periodic table, and they exhibit very similar outer shells and ionic radii (Ge=47Å; Si=42Å) (Azam and Volcani, 1981). Ge has similar bond length with Si (Ge-O=1.75Å; Si-O=1.64Å) (Martin et al., 1996), thus Ge can replace Si in the tetrahedral lattice site of minerals (Goldschmidt, 1958). Molar Ge/Si ratios in natural systems are typically near ~ 10^{-6}. Ge has larger atomic radius than Si, thus Ge tends to partition in phyllosilicates rather than other dense silicate minerals. Ge and Si can be treated as a "pseudo-isotopic" pair and their properties make them an ideal geochemical tracer of

temperature and weathering rates (Shemesh et al., 1989). Ge/Si has several advantages as a tracer of reactions involving weathering, hydrothermal alteration and biologic cycling (Froelich et al., 1992). First, both dissolved Ge and Si come from weathering of silicate minerals. They exist in solution primarily in the form of silicic acid (H_4SiO_4) and germanic acid (H_4GeO_4). They have similar depth profiles in the ocean, indicating they are utilized by organisms in identical ways. Second, compared with some other indicators of weathering and alteration such as Sr or Li isotopes, Ge/Si has Si directly in this tracer, and thus should be a more direct indicator of changes in silica cycling and behavior.

Global Germanium Cycle

Bedrock Ge/Si ratios are typically ~1.5 μmol/mol (Kurtz and Derry, 2002). Ge/Si ratios in rivers are usually lower than the bedrock, and this can be explained by incongruent weathering and secondary mineral formation. Rivers contains dissolved primary minerals and suspended secondary clays. Weathering solutions have low Ge/Si ratios of ~0.1 to 0.5 μmo//mol while secondary clays have a much higher value of ~3 to 10 μmol/mol (Kurtz et al., 2001; Lugolobi et al. 2010; Aguirre et al., 2016; 2019). With increased weathering intensity secondary clays can dissolve, releasing solutes with a high Ge/Si. Therfore Ge/Si ratios in rivers can be a measure of weathering intensity (Murnane and Stallard, 1990; Mortlock and Froelich, 1987). Like silica, most Ge in the ocean comes from rivers and hydrothermal fluids. The Ge/Si ratio in rivers is 0.6±0.06 μmol/mol (Mortlock and Froelich, 1987), which is controlled by the weathering

intensity and parent material. The hydrothermal fluid at mid-ocean ridges has Ge/Si ratio of 4~25 μmol/mol (Baronas et al., 2017), but terrestrial hydrothermal sources are typically higher, and in extreme cases reach to 1000 μmol/mol (Evans and Derry, 2002).

Germanium sinks

There are three main processes by which Ge is removed from the oceans: 1) biogenic opal formation that does not significantly fractionate Ge from Si; 2) reverse weathering and authigenic clay formation, which produces very high Ge/Si ratio minerals, and 3) the "non-opal sink" that appears mostly to be the formation of authigenic Fe-oxyhydroxides that incorporate Ge and thus fractionate Ge from Si. Ge can be taken up by siliceous organisms. Diatoms are the primary biogenic opal producer in the ocean, and sponges come after. Unlike in fresh water, in most cases, marine diatoms smaller than 64 μm do not fractionate Ge/Si ratio in the ocean, so the ratio in diatoms is thought to be the same as in seawater (Froelich et al., 1992). However, Ge discrimination can occur when diatoms are stressed by strong Si limitation (Sutton, 2010). The Ge/Si of modern seawater has been estimated at 0.70 μmol/mol by Froelich et al. (1992) and as 0.76 μmol/mol by Sutton et al. (2010).

Another Ge removal mechanism is non-opal burial resulting from early diagenetic Fe reduction and opal dissolution. The Fe^{2+}, Si and Ge profiles in sedimentary pore

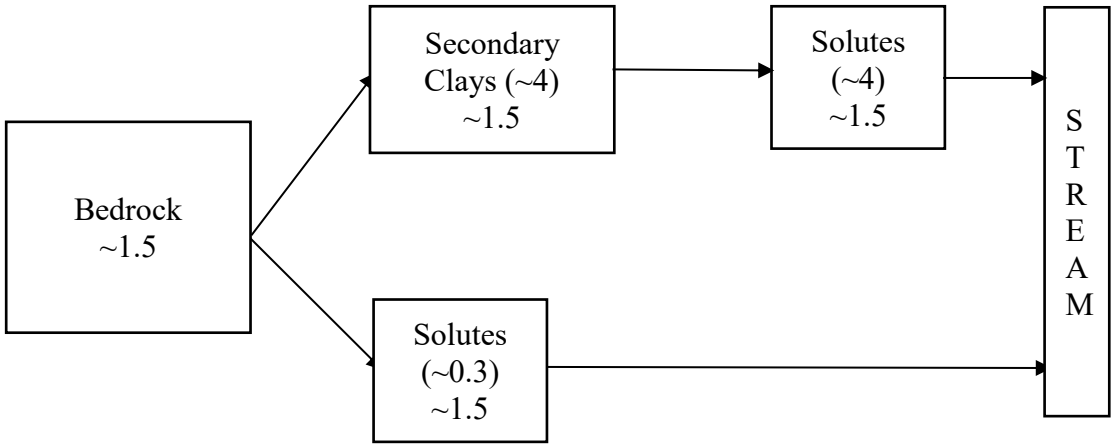

Figure 1.2 Schematic graph of weathering intensity and Ge/Si ratio of river Kurtz 2000

waters indicate that the sequestration is more effective at removing Ge than Si, and this sequestration can make a difference to global oceanic Ge/Si ratio (Hammond et al., 2000). Fe^{2+} rich pore water and an anoxic environment are necessary to sequester Ge. The non-opal burial process is similar to 'reverse weathering' of silica; Ge is sequestrated from sediment porewater to form authigenic minerals with very high Ge/Si ratio. In reducing sediments, soluble Fe^{2+} diffuses upwards from deeper sediments and oxygen diffuses down from the sediment-water interface. At a certain depth, usually several millimeters to centimeters below the surface, Fe^{2+} is oxidized to ferric oxyhydroxide, and coprecipitation or adsorption of Ge can occur. Where it occurs this process removes 20-90% of dissolved Ge released by opal dissolution (Hammond et al., 2000). This process occurs under very specific circumstances of high organic carbon input and efficient iron reduction. Ge-sequestration studies have been done in the Equatorial Pacific and a continental margin sites off coast of Southern California (Hammond et al., 2000). While organic carbon rich sites off of Southern California showed evidence of this non-opal sink, no evidence of Ge sequestration has been found in Tanner Basin and Patton Escarpment along California Margin. The sediments of these two sites are suboxic, however the concentration of remobilized Fe^{2+} is very low. These results indicate the presence of anoxic sediments and Fe^{2+} very near the sediment-water interface are required for the formation of non-opal sink. Experiments have been implemented to study the composition and structures of Ge authigenic minerals. In the process of non-opal mineral formation, Fe is an indispensable element. Ge coprecipitates with Fe-oxyhydroxide when it is adsorbed to goethite and interacts with

iron hydroxide (Pokrovski, et al., 2006). Ge tetrahedra can bond with goethite by edge-sharing or incorporate with iron hydroxide by double-corner-sharing.

Hammond et al. (2000) proposed that temperature is an important control on the Ge/Si ratio of seawater. The mechanism behind this hypothesis is that temperature has an effect on how much opal rain can reach to the seafloor. When temperature is low, the opal dissolution rate decreases, which results in more opal rain sinking to the seafloor. With this larger flux of biogenic silica to the sea floor, potentially more Ge will go to the non-opal reservoir and the Ge/Si of seawater will decrease. This mechanism can account for the Ge/Si variations recorded in diatoms during glacial and interglacial intervals, such as Mid-Miocene and LGM (Hammond, 2004). However, more recent work suggests that 90% of opal dissolution currently occurs at the sediment-water interface and not during settling through the water column (Treguer and De La Rocha, 2013). If this is the case dissolution rates may be less sensitive to deep water temperatures. Alternatively, the precipitation of Ge correlates with the detrital fraction and detrital to opal ratio of sediments. More Ge is sequestered when there is a larger fraction of detrital material in the sediments (King, et al., 2000). Thus, an increase of aeolian detritus in the sediments might also be responsible for the reduction of Ge/Si ratio due to enhanced Ge removal, i.e. during glacial periods.

Ge/Si can be fractionated by secondary mineral formation, which involves weathering and soil formation, reverse weathering and removal via what is termed the “non-opal” sink (Kurtz et al., 2001; Michalopoulos et al., 1995; Hammond et al., 2000). Authigenic

minerals produced by three processes all have high Ge/Si ratios. Ge and Si transported by rivers from land to ocean can be deposited in deltas or on the continental shelf. When they encounter Fe-rich and organic C-rich sediments, they react with Fe- and Al-bearing minerals and form clays. This reaction can occur with dissolved Ge and Si, diatom frustules and quartz. Debris containing Ge and Si buried in the sediments can dissolve in the pore water, diffuse to the water-sediment interface and react with Fe-oxyhydroxide. The significance of early diagenetic processes has been considered in our work to build the Ge and Si box model and to interpret the Ge/Si of seawater.

Ge/Si ratios of other fluxes are not well constrained. Some assumptions are made due to the lack of data of fluxes from other sources. The Ge and Si in groundwater are generated by the same weathering system with river, thus the Ge/Si of groundwater should be similar to the value of riverine input, which is 0.5 μmol/mol. The dust input is a variable affected by the glacial and interglacial cycle, and a fractionation occurs with partial dissolution of aerosols. More Si is released to sea water from dust dissolution, and a Ge enriched solid is left in marine sediments. During glacial period, the aeolian flux increases by a factor of 3 to 5 while the Ge/Si of aerosols is relatively constant (Kurtz, 2000). We estimate that the Ge/Si ratio of the input from dust is around 0.4 μmol/mol. The ratio of low temperature hydrothermal fluid is included in that of warm hydrothermal fluid, because the low temperature alteration is less significant. (Hammond, 2004). The Ge flux values are calculated as Si flux times Ge/Si ratio. Baronas et al. (2017) developed a global Ge budget using better constrained Si fluxes

and the assumption of a steady state for the oceanic Ge mass balance, Ge/Si ratios, and $\delta^{74}Ge$.

In sum, germanium and silica cycles are closely coupled. The riverine fluxes of Ge and Si are estimated relatively accurately, the hydrothermal fluid flux of silica is also well estimated, but the low-temperature fluxes of Ge and Si are poorly constrained. The Si cycle is better studied and other fluxes are also calculated based on mass balance or box model. Estimates of Ge cycle still need to be improved to make Ge/Si a more powerful indicator of weathering.

Table 1.2 Global Ge and Si fluxes and Ge/Si ratio

	sources	Si flux(Tmol/y)	Ge/Si(μmol/mol)	Ge flux(Mmol/y)
Input	river	7.3±2.0	0.5	3.65±1
	groundwater	0.6±0.6	0.5	0.3±0.3
	marine sediments	1.9±0.7	0.6	1.14±0.42
	dust	0.5±0.5	0.4	0.2±0.2
	hydrothermal fluids	0.6±0.4	10.5	6.3±4.2
Output	burial	9.9±7.3	0.76	7.5±5.5
	reverse weathering	1.5±0.5	3.5	5.25±1.75
	non-opal sink	/	/	13.3±10.6

Silica fluxes are from Treguer, 2013;
Ge/Si ratio is from Baronas, 2017, Table 4
Ge/Si ratio of dust and marine sediments are from Kurtz (2000), Ge/Si and trace element studies of silicate weathering and aerosol deposition (Ph.D. Thesis).

CHAPTER 2

MID-MIOCENE CLIMATIC OPTIMUM

Overview of Cenozoic Climate History

The Cenozoic Era covers the last 65 million years in the Earth's history. This period is well known for its complex and continuous climatic variation. Multiple kinds of proxies allow us to reconstruct the climatic history during this period. One of the most important proxies is the oxygen isotope composition of marine benthic foraminifera. The fractionation of $\delta^{18}O$ between calcite and water is temperature-dependent. O'Neil et al. (1969) experimentally determined the relationship between the fractionation factor α, defined as

$$2.1)\quad \alpha = \frac{\left(\frac{^{18}O}{^{16}O}\right)_{CaCO_3}}{\left(\frac{^{18}O}{^{16}O}\right)_{H_2O}}$$

and temperature, T as

$$2.2)\qquad 1000\ln\alpha = 2.78(10^{-6}\ T^{-2}) - 3.39$$

The term $1000\ln\alpha \approx \Delta_{CaCO3\text{-}H2O}$, $= \delta^{18}O_{calcite} - \delta^{18}O_{H2O}$, i.e. the observed difference between the isotopic composition of calcite and water in equilibrium (Criss, 1999, Principles of Stable Isotope Distribution). The calcite-water fractionation curve is shown in Figure 2.1. The fractionation decreases with temperature. If the $\delta^{18}O_{H2O}$ is known and constant, then the isotopic composition of foraminiferal calcite can provide an estimate of water temperature. Benthic foraminifera are calcium-carbonate forming zooplankton that live in deep water. As a consequence, their $\delta^{18}O$ can provide an

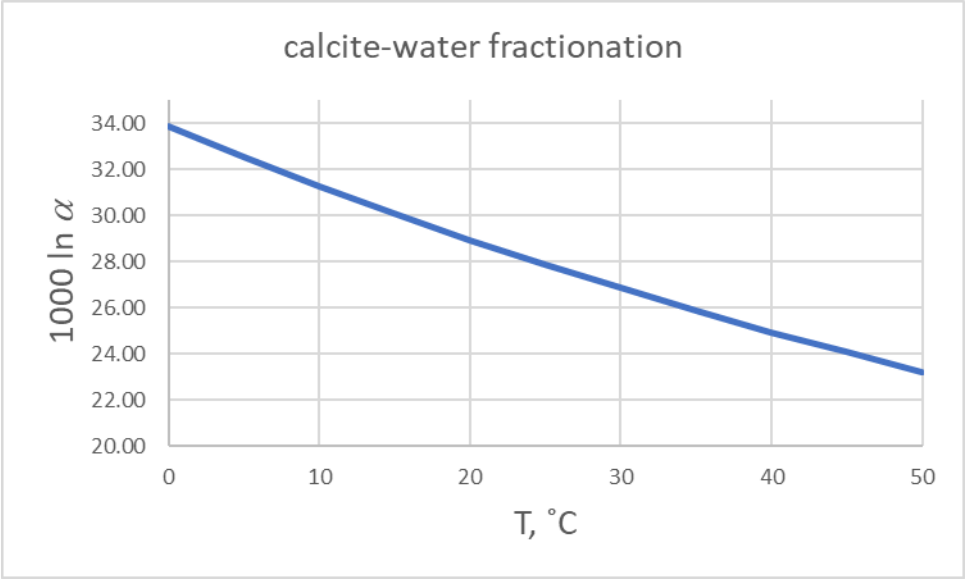

Figure 2.1 Calcite-water fractionation curve for oxygen isotopes (^{18}O and ^{16}O), O'Neil et al., (1969)

estimate of deep-water temperatures since deep water has a fairly uniform temperature

However, the presence of glaciers impacts the $\delta^{18}O$ of the oceans. Water molecules with ^{16}O are easier to evaporate and those with ^{18}O more readily condense. As a consequence, high latitude ice sheets have a lower $\delta^{18}O$ value than seawater. In an ice age, the ice sheet expands and more ^{16}O is stored in glaciers, consequently heavy oxygen isotopes are left in seawater. In sum, $\delta^{18}O$ value of seawater is relatively higher when ice volume grows. When ice sheets are present, the $\delta^{18}O$ value of foraminifera depends both on the deep-water temperature and the volume and isotopic composition of the ice. Both cooler temperatures and increasing ice volumes push $\delta^{18}O$ of benthic foraminifera to higher values, so overall higher $\delta^{18}O_{foram}$ is consistent with cooling. But it can be difficult to separate the effects of cooling deep water from increasing ice volume.

For most of the time, Cenozoic presents a cooling trend. However, two warming events and several excursions stand out. The two major warming events are EECO (early Eocene climatic optimum, 50-52Ma) and MMCO (mid-Miocene climatic optimum, 15-17 Ma) indicated by benthic foraminiferal $\delta^{18}O$ data (Zachos et al, 2001). From 52-59 Ma, the earth's climate exhibits a warming trend and reaches a peak, the EECO. This was followed by a general cooling trend culminating in the onset of significant glaciation on Antarctica at the Eocene-Oligocene boundary, at 34 Ma. The benthic $\delta^{18}O$ record increased 3‰ from middle Eocene to early Oligocene, 1.8‰ of the increase reflects the ice volume expansion (Zachos et al., 2001). Benthic $\delta^{18}O$ values remained

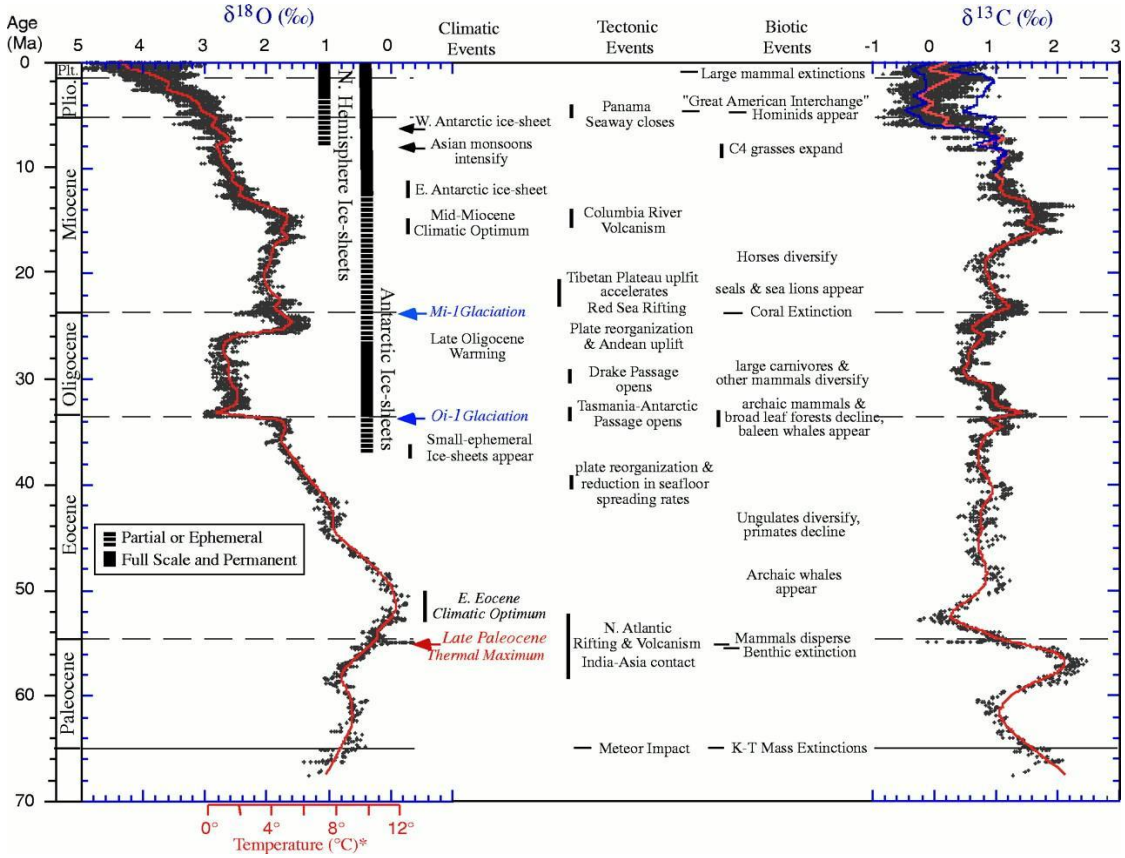

Figure 2.2 Cenozoic global deep-sea δ13C and δ18O record based on data compiled from more than 40 DSDP and ODP sites. Most of the data are derived from analysis of two benthic taxa, Cibicidoides and Nuttallides in pelagic, fine-grained, carbonate-rich oozes or chalks. The raw data were smoothed using a five-point mean value and curve-fitted with a locally weighted mean. For carbon isotope record, separate curve fits for Atlantic (blue) and Pacific above the middle Miocene to illustrate the increase in basin-to-basin fractionation that exceeds 1‰ in some intervals. Some key tectonic and biotic events are listed above. Zachos et al., 2001

high indicating a cool phase and permanent ice sheet with mass as much as 50% of present-day ice sheet until ~27 Ma followed by a late Oligocene warming (Zachos et al., 2001). The climate underwent a mild cooling then started to warm again from ~20 Ma. This later the warming trend culminates in the MMCO at 15-17 Ma. After the MMCO, gradual cooling persisted until the early Pliocene and Antarctic ice sheet expanded. A short warming began from early Pliocene until ~3.2 Ma. The cooling continued and benthic $\delta^{18}O$ increased to ~4 to 5‰ in the late Pleistocene, reflecting the onset of North Hemisphere Glaciation (Zachos et al., 2001).

MMCO $\delta^{18}O$ and $\delta^{13}C$

The Mid-Miocene Climatic Optimum (MMCO) is a short warming period between 14.8-17 Ma, followed by a long-term cooling trend and glaciation. The MMCO has attracted interests from researchers due to its significant climate and carbon cycle perturbation. This period is characterized by a negative ™^{18}O shift, positive ™^{13}C shift, shoaling of the carbonate compensation depth (CCD) and high atmospheric carbon dioxide levels (pCO_2) (Lear et al., 2010; Holbourn et al., 2016; Campbell et al., 2018; Foster et al., 2012). Large variations of different indicators show that climate in MMCO is very unstable. Both planktonic (surface water) and benthic foraminiferal ™^{18}O decrease during this period (Woodruff and Savin, 1991). Model simulation indicates that global average ocean surface temperatures were 2-4 ℃ warmer than pre-industrial values (You et al., 2009). Evidence suggests that several events happened during that time, including retreating of East Antarctic Ice Sheets, intensification of East Asia

summer monsoon, carbon cycle perturbations, and eruption of the Columbia river flood basalts. The amplitude of ™^{18}O fluctuation is ~1‰ and a sharp rise of δ^{13}C in marine carbonates occurred at the onset of MMCO (Vincent and Berger, 1985; Holbourn. et al, 2015). However, the temperature does not account for all the δ^{18}O change, because ice volume contributes to the δ^{18}O shift as well. The ™^{18}O value increased ~5.4‰ over the entire Cenozoic, but only 3.1‰ is derived from deep water cooling, the rest (2.3‰) corresponds to ice sheet expansion (Zachos et al., 2001). Palynological data shows high abundances of pollen and spores ~15.5 Ma in Antarctica, which provides evidence for warming event and ice sheet reduction (Warny et al., 2009). ™^{18}O records from Indian Ocean, Equatorial Pacific and South Pacific, Atlantic and Antarctic exhibit similar signals, indicating the global impact of the MMCO (Woodruff and Savin, 1991). ™^{18}O excursions divide the early and middle Miocene into several stages. Miller et al (1991) proposed 7 ™^{18}O Mi-events, and Woodruff and Savin (1991) recognized 6 globally correlated ™^{18}O excursions. Mi2 is recognized to be a ™^{18}O increase of 0.6‰-0.8‰ at ~16.5-16Ma for benthic and planktonic record; it is within MMCO and the amplitude is smaller than Mi1 (Miller et al., 1991). Immediate cooling at the end of MMCO is recognized as the Mi3 event, with an amplitude of ~0.5-0.8‰; this period implies a transition from warm to cool climate from 14.9-13.6 Ma. Ice sheet expansion and lower sea level are associated with Mi events as well (Miller et al. 1991). These events mark part of the series of Cenozoic cooling steps, while suggesting highly variable climate in Miocene (Holbourn et al., 2007). Carbon isotope (δ^{13}C) excursions reflect perturbations of the carbon cycle during MMCO. The interpretation of the positive δ^{13}C events is that

they reflect intervals of increased burial of organic carbon. The carbon isotope mass balance for the oceans is given by:

2.3) $\delta^{13}C_{in} = f_{org} \times \delta^{13}C_{org} + f_{carb} \times \delta^{13}C_{carb}$

Where $\delta^{13}C_{in}$ is the mean isotopic composition of carbon entering the ocean, $\delta^{13}C_{org}$ is the isotopic composition of organic carbon, $\delta^{13}C_{carb}$ is the isotopic composition of carbonate carbon, f_{org} is the fraction of carbon leaving as organic carbon and f_{carb} is the fraction of carbon leaving as carbonate. In this two-component model

2.4) $f_{org} + f_{carb} = 1$

The input term $\delta^{13}C_{in}$ is typically assigned a value close to that of mantle carbon, ca. -5 ‰ (Derry, 2014). $\delta^{13}C_{carb}$ is close to that of dissolved inorganic carbon (DIC) in the oceans. The net fractionation arising from photosynthetic uptake of dissolved CO_2, biosynthesis and early diagenesis is given by

2.5) $\Delta_B = \delta^{13}C_{carb} - \delta^{13}C_{org}$

i.e. the mean difference in the isotopic composition of carbonate and organic carbon entering the sedimentary reservoir at any moment in time. For the Neogene this value (Δ_B) is near 23 ‰ (Derry and France-Lanord, 1996).

$$2.6a)\ \ \delta^{13}C_{in} = f_{org} \times (\delta^{13}C_{carb} - \Delta_B) + (1 - f_{org}) \times \delta^{13}C_{carb}$$

$$2.6b)\ \ \delta^{13}C_{in} = -5\ ‰, \Delta_B = 23‰$$

$$2.6c)\ \ -5‰ = f_{org}\delta^{13}C_{carb} - 23‰ f_{org} + \delta^{13}C_{carb} - f_{org}\delta^{13}C_{carb}$$

$$2.6d)\ \ -5‰ = -23‰ f_{org} + \delta^{13}C_{carb}$$

$$2.6e)\ \ f_{org} = \frac{5‰ + \delta^{13}C_{carb}}{23‰}$$

This equation (2.6e) shows that $\delta^{13}C_{carb}$ correlates with f_{org}, i.e the fractional rate of C_{org} burial. Since the ocean must be at approximate steady state with input carbon fluxes equal to output carbon fluxes, increases in $\delta^{13}C_{carb}$ are indicating increases in organic carbon burial. The organic carbon-rich sediments corresponding to the middle Miocene were first identified in North Pacific margin and Monterey Formation in California. Thus, this event was initially proposed as the "Monterey Excursion" (Vincent and Berger, 1991). Vincent and Berger (1991) proposed the "Monterey hypothesis" to illustrate a potential mechanism of Miocene cooling and incorporate $\delta^{13}C$ and $\delta^{18}O$ record. They suggest that plate tectonic events triggered the change of oceanic current circulation and resulted in the cooling of polar area (Shackleton and Kennett, 1975; Blanc et al., 1980). Coastal upwelling was intensified presumably by cooling threshold. Excess organic matter burial was developed during middle Miocene and consequently lowered the pCO_2. The low pCO_2 in atmosphere subsequently enhanced global cooling, leading to the step-like cooling trend (Vincent and Berger, 1991). Evidence for enhanced primary production was found in sediments from worldwide, including Caribbean, Pacific and Mediterranean sites (Mutti et al., 2005; Woodruff and Savin.

1985; Follmi et al., 2008). However, there is a time lag between the carbon excursion at 17 Ma and the cooling after 14 Ma. Additionally, the estimated amount of buried organic carbon in MMCO cannot fully explain the drawdown of pCO_2 (Follmi et al., 2005). The carbon isotope maxima (CM) events occur with a strong ~400 kyr eccentricity cycle, and most CM events coincide with oxygen excursion events, while the benthic $\delta^{13}C$ record shows that the interval of the first three CM events is ~850 kyrs (Woodruff and Savin, 1991), and the timing of the CM1-CM3 events correspond to ~16.4-15.5 Ma. The onset of CM1 occurred at 16.9 Ma which marks the beginning of MMCO; the ™^{18}O dropped ~1‰ at the same time, indicating the carbon cycle perturbation was triggered by climate change. Benthic foraminiferal $\delta^{13}C$ values indicate high carbonate accumulation rates from 16-13 Ma for Pacific, and 16-14 Ma for Atlantic; the timing is roughly consistent with MMCO, this suggests pCO_2 is high during that period (Woodruff and Savin, 1991). Carbonate dissolution and a short CCD shoaling at ~17 Ma followed by an abrupt CCD deepening suggest the acidification of ocean and high pCO2 at the beginning of MMCO (Woodruff and Savin, 1991; Campbell et al., 2018). Overall, evidence from proxies and model suggest the perturbation of carbon cycle during MMCO.

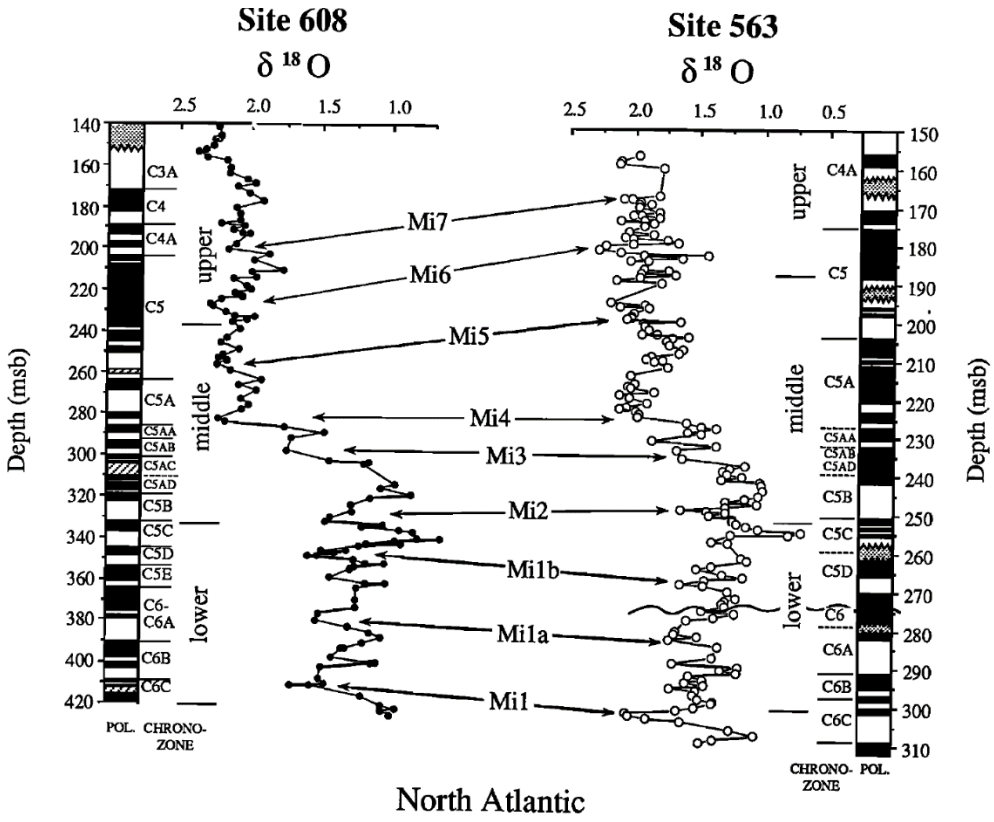

Figure 2.3 Mi-events. Miocene oxygen isotope stratigraphy and magnetostratigraphy for eastern North Atlantic Site 608 and western North Atlantic Site 563. Miller et al., (1991)

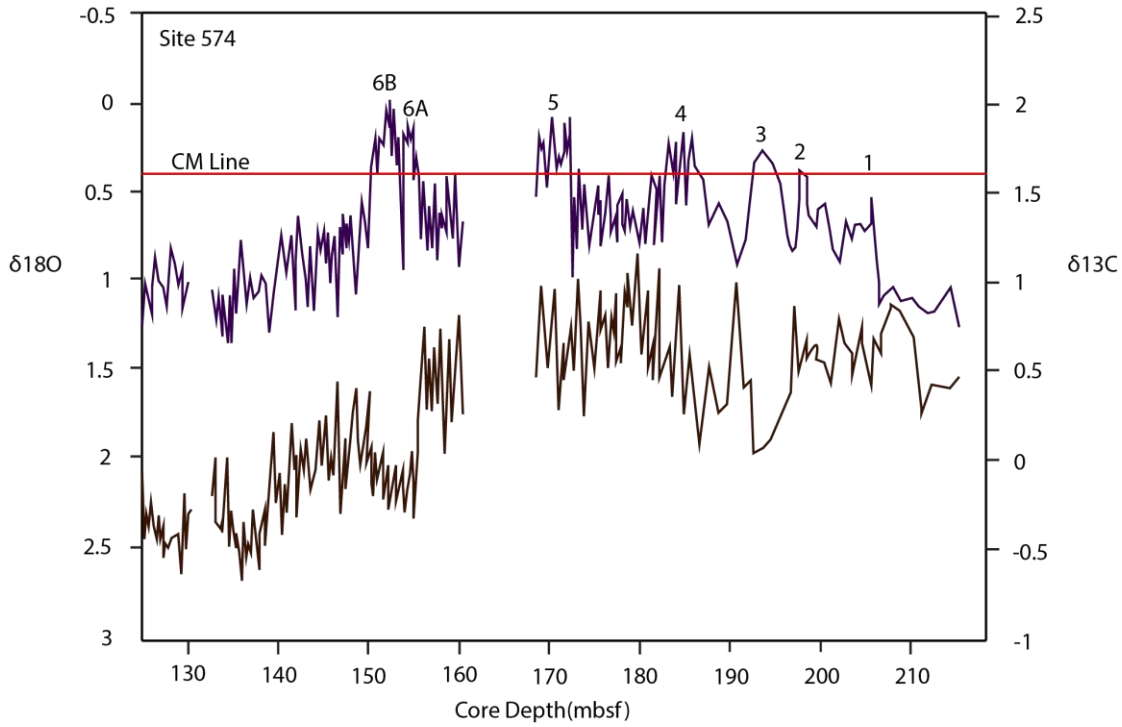

Figure 2.4 CM-events, Benthic (Cibicidoides) oxygen (lower) and carbon (upper) records, biostratigraphic datums and carbonate dissolution intervals for DSDP Site 574 in the eastern equatorial Pacific. Triangles above the isotope curves show the location of dissolution intervals. Triangles below the isotopic curve show the locations of biostratigraphic datums and the age and fossil type of each. The uncertainty of the location is indicated by the length of the triangle. Locations of 13C maxima CM1 through CM6B are indicated in the upper isotope curve, and locations of 18O events A through F are indicated in the lower isotope curve. Woodruff and Savin, 1991.

Temperature and pH in MMCO

Pagini et al. (1999) reconstructed the pCO_2 over Miocene via alkenone records and concluded that pCO_2 was ~140-300 ppm, lower than preindustrial value. They did not find a clear rise of pCO_2 during MMCO, nor an obvious drop after 14 Ma. More recent pCO_2 reconstructions based on a variety of proxies including boron isotopes, leaf stomata and alkenones suggest that pCO2 was ~400-500ppm during MMCO, higher than preindustrial level, then gradually decreased to 200 ppm by 12 Ma (Foster et al., 2012; Zhang et al., 2013; Super et al., 2018). Boron isotopes are pH sensitive and B has a residence time in the ocean of 11-17 Ma (Lemarchand et al., 2000). Thus, $\delta^{11}B$ data can provide a connection between atmosphere CO_2 and ocean pH, these records are essential for understanding ocean carbonate system during MMCO. The pH reconstruction from $\delta^{11}B$ in planktonic foraminifera indicates that the surface ocean pH was ~7.6-7.7 in the MMCO, which appears to be the most acidic for the last 22 Ma, corresponding to a low aragonite saturation state (Sosdian et al., 2017). B/Ca ratios increases from 15.5 Ma, which indicates increasing $[CO_3^{2-}]$ and alkalinity input from continental weathering (Kender, 2014). In addition, the rise of $[CO_3^{2-}]$ implies an increase in pH that will cause CO_2 drawdown in the atmosphere and the data is in agreement with the $\delta^{11}B$ reconstruction of pCO_2 after 15Ma.

Not all the proxies show apparent changes in MMCO, however, the amplitude of fluctuation is high and Antarctic ice sheet is dynamic (Holbourn et al., 2015; Foster et al., 2017). The atmospheric CO_2 level is closely coupled with global temperature.

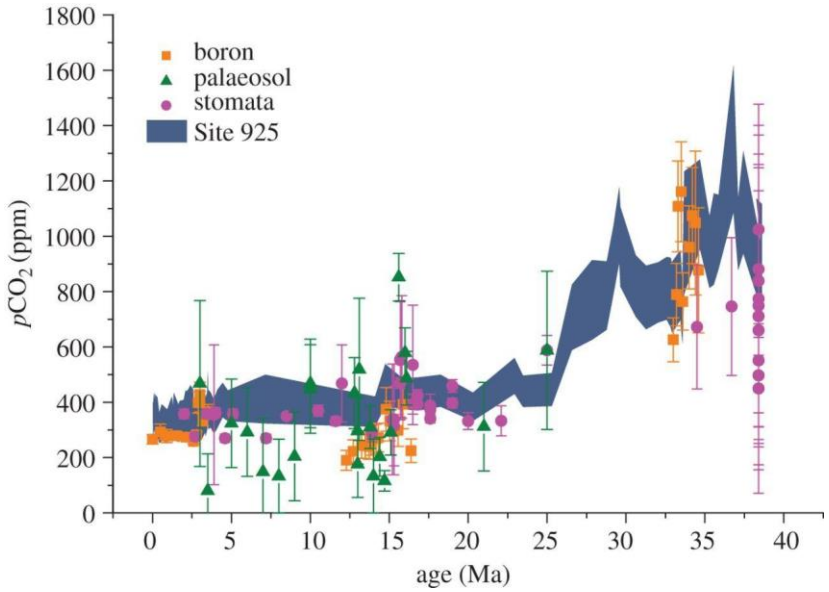

Figure 2.5 pCO2 estimates for the past 40Ma using different proxies, Zhang et al. (2013).

Estimated temperatures in MMCO exhibit a wide range. Sea surface temperature in the mid latitude North Atlantic during MMCO was 28-35 ℃ based on Tex86 reconstruction (Super et al., 2018). Alkenone proxies and climate models suggest that the sea surface temperature was ~15℃ warmer than modern at Site 608 in the North Atlantic Ocean (Super et al., 2018), mean average temperature was ~4℃ above preindustrial values based on 400 ppm pCO_2 modeling, and peak global temperature was ~8℃ above present values (Goldner et al., 2014). Benthic foraminiferal Mg/Ca is a powerful proxy to help deconvolve the temperature change from the $\delta^{18}O$ signal, because Mg/Ca ratios depend on calcification temperature and are not directly sensitive to ice volume (Lear et al., 2015). An increase 1℃ of seawater will cause 0.22‰ increase in seawater surface $\delta^{18}O$ (Wang et al., 1995). This relationship is derived from lab calibration of fractionation factors without considering ice volume effects, and the sea surface temperature was reconstructed with planktonic *foraminifera G. ruber*. A 1℃ increase of the estimated bottom water temperature results in 0.09±0.04 mmol/mole benthic foraminifera Mg/Ca increase using equation 10 of (Lear et al., 2015). The benthic Mg/Ca is ~2.4 mmol/mol at 15 Ma, and gradually decreased to 2 mmol/mol at 13 Ma, corresponding to ~4.4℃ decrease in bottom water temperature. Collectively, several proxies suggest the MMCO was a relatively warm and humid period. This warmer climate is expected to affect the weathering rates and is reflected by some other indicators.

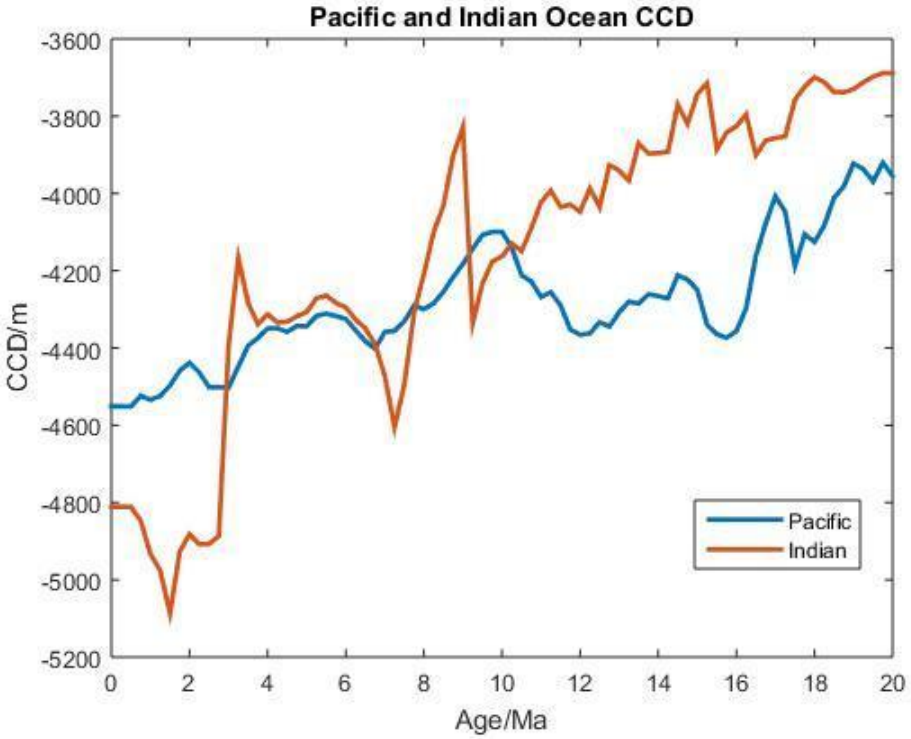

Figure 2.6 Pacific and Indian Ocean CCD reconstructions over past 20Ma using seismic model TX2007, and viscosity model V2 for dynamic topography corrections. Blue line is Pacific CCD reconstruction and red line is Indian Ocean CCD reconstruction, Campbell et al., 2018

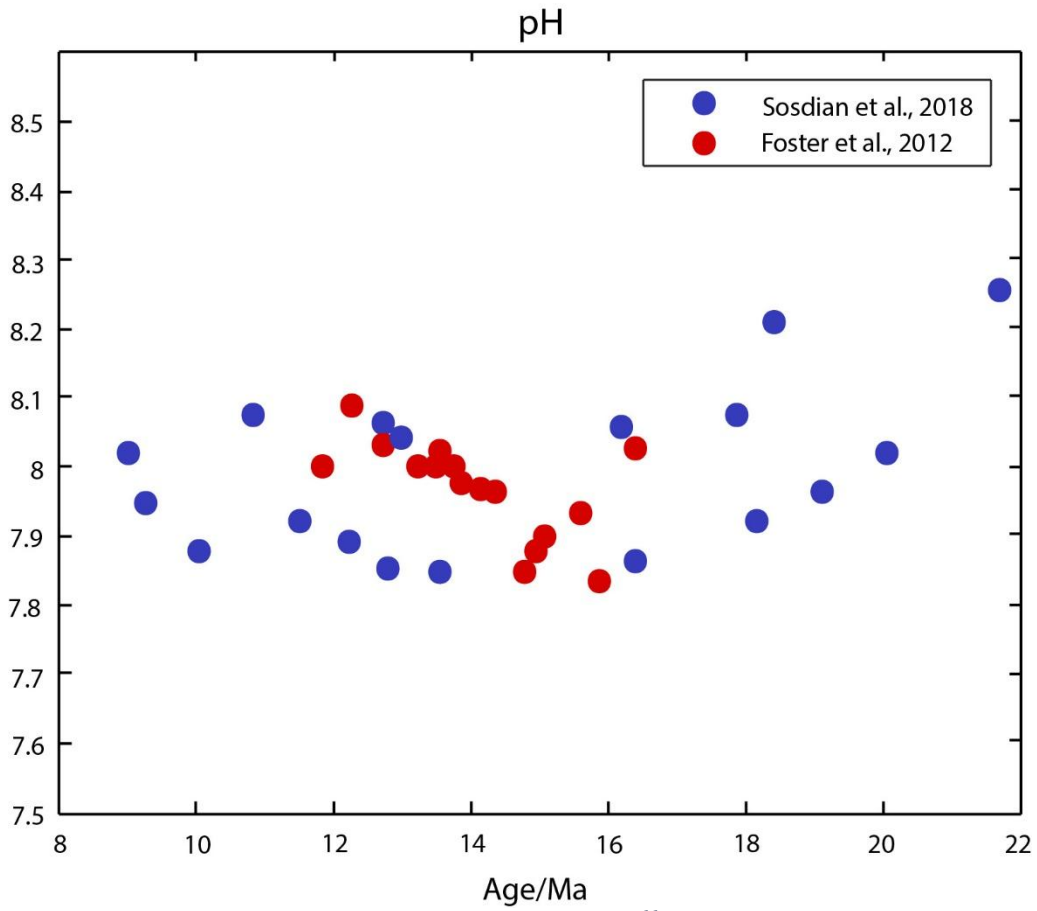

Figure 2.7 Ocean pH reconstruction using $\delta^{11}B_{sw,}$ Foster et al., 2012

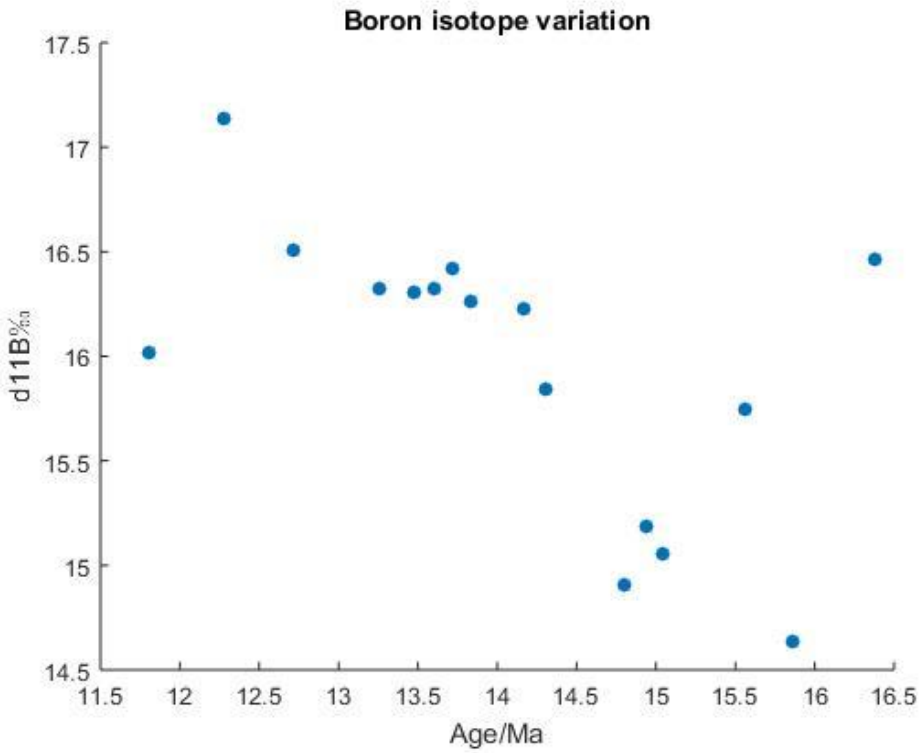

Figure 2.8 $\delta^{11}B$ record of G.Sacculifer (300-355μm, planktic) from ODP 761, Foster et al., 2012

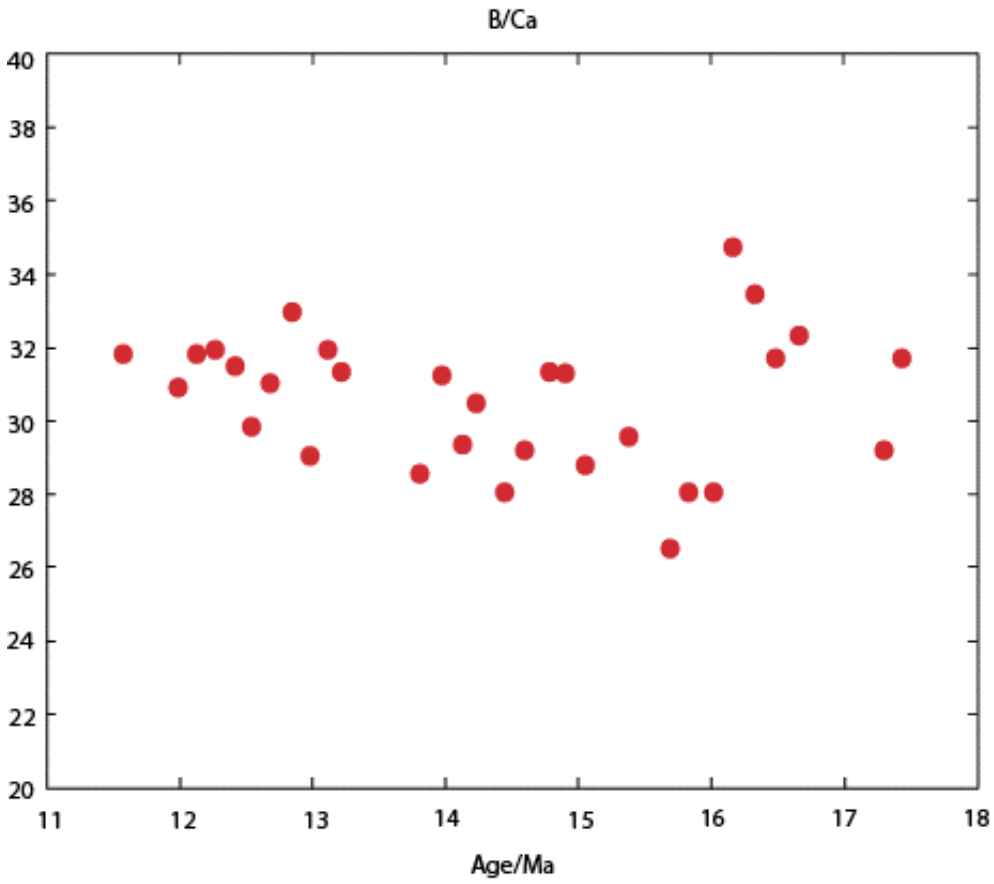

Figure 2.9 Deep-ocean B/Ca record as carbonate proxies in MMCO. Kender et al., 2015

Weathering Tracers in MMCO

$^{87}Sr/^{86}Sr$, Os isotopes and δ^7Li are widely used to reconstruct weathering fluxes. The marine $^{87}Sr/^{86}Sr$ record reported by Hodell et al. (1994) increases from early to middle Miocene. $^{87}Sr/^{86}Sr$ increases rapidly from 19 Ma to 16 Ma, and the growth rate peaks at ~17 Ma then gradually falls through 15 Ma. The growth rate is nearly constant at 15-13 Ma. Starting from 12 Ma, the growth rate slows until 9 Ma. The variation of the growth rate of $^{87}Sr/^{86}Sr$ record corresponds well to climate change trend in Miocene. However, part of the variation results from exhumation of upper Lesser Himalaya strata at 16 Ma and reflect erosion of carbonates (Myrow et al., 2015). $^{187}Os/^{188}Os$ was at steady state from 28 to 19 Ma, the ratio is 0.7337 (Myrow et al., 2015). The $^{187}Os/^{188}Os$ begins to increase at 16 Ma. The rise after 16 Ma may result from the weathering of old organic-rich shales that contains radiogenic Os (Myrow et al., 2015). δ^7Li increases ~5‰ overall through Neogene, while a minima occurred at MMCO, indicating enhanced continental weathering during that time (Froelich and Misra, 2014).

It is likely that the Si cycle interacted with the climate change and experienced a perturbation during this period. Many indicators such as $^{87}Sr/^{86}Sr$, $^{187}Os/^{188}Os$ and δ^7Li had suggested some continental weathering and Si cycle changes during this period (Hodell et al., 1994; Reusch et al., 1998; Misra and Froelich, 2012). However, the lack of high-resolution data and the complexity of the indicators make them difficult to interpret. Ge/Si ratio is potentially a more straightforward indicator since it includes Si directly. Si has a residence time of 10000-15000 years while Ge has a shorter residence

time of ~4300 years (Treguer et al., 2013; Baronas et al., 2017). The oceanic Ge/Si ratio is the result of dynamic balance of inputs including river, aeolian, hydrothermal, groundwater and dissolution of marine sediments, and outputs including biogenic opal production, authigenic clay formation and the "non-opal sink" for Ge. Fluxes from all types of inputs and outputs as well as Ge/Si of different fluxes can vary with time. Ge/Si ratios of seawater are recorded in diatom frustules. Shemesh et al. (1989) presents some late Cenozoic Ge/Si data from Southern Ocean diatoms, but their data from 14 to 17 Ma is quite sparse and no further work has been done to study the Ge/Si ratio during this period. We believe high-resolution data will help us to better constrain variations in oceanic Ge/Si and get an idea of how Si cycle and continental weathering responded to the MMCO. To get a better record of Ge/Si ratio, we requested opal-rich samples from ODP. Site U1337 was selected due to its good continuity and well constrained time correlation.

Multiple events seem to be associated with the global warming during mid-Miocene. The Columbia River basalt (CRB) eruption occurred coincidentally with MMCO (Barry et al.,2010). Eruptive activity started ~17 Ma, and lasted for ~4 Ma. The eruptive events themselves occupy only about 1% of total duration and the frequency of eruption is ~4000 years. The eruptions are not evenly distributed during the 4 million years, it is very likely that eruptions happened more often in the beginning and became less frequent with time. Simulations have been carried out to estimate the impact of CO_2 degassing from CRB eruption. They found that the CRB eruption could have increased atmospheric pCO_2 by 90 ppm, and this would have caused a 0.9-1.9°Cincrease in global

average temperature by 15.9 Ma (Armstrong Mckay et al., 2014). A significant amount of sulfur was released from the eruption, but the residence time of sulfur is relatively short. It takes decades to remove the effect of sulfur released from an eruption (Davis, 2017). CO_2 degassed from eruption has a much longer residence time and has a prolonged warming effect. This can account for part of the pCO_2 and temperature increase of MMCO.

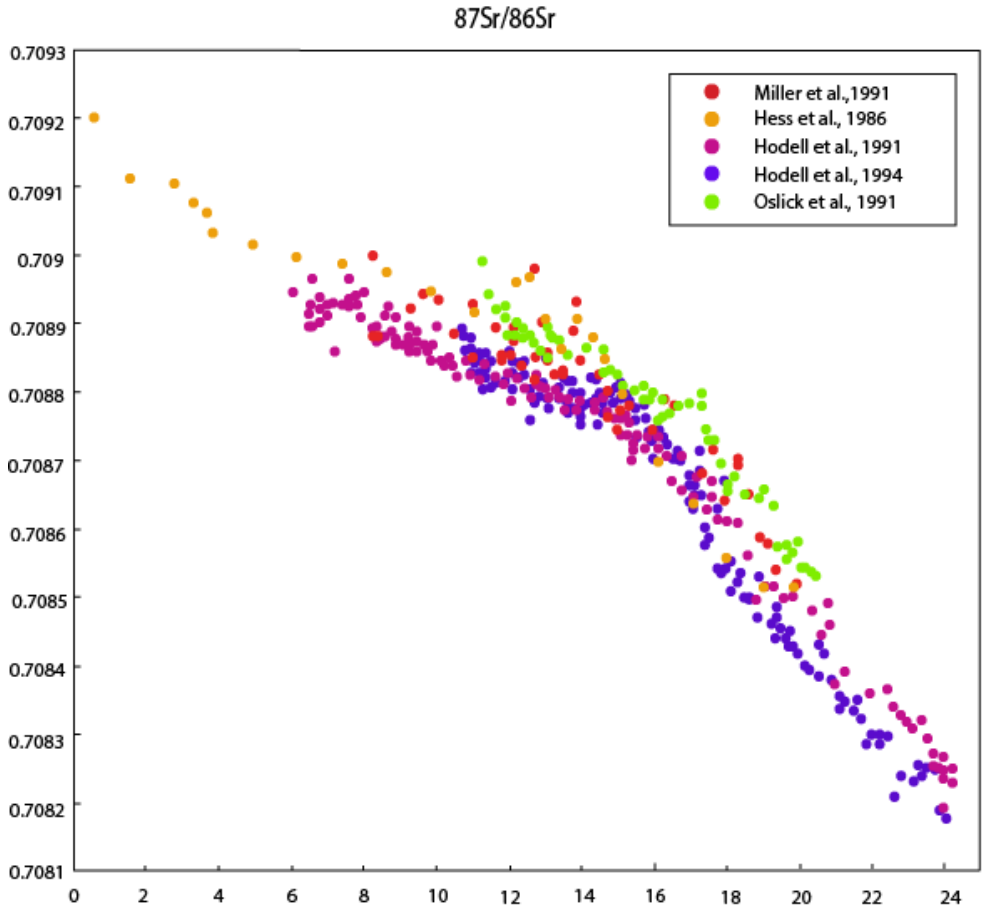

Figure 2.10 Seawater $^{87}Sr/^{86}Sr$ ratio record, blue dots are from Miller et al., 1991; orange dots are from Hess et al., 1986; yellow dots are from Hodell et al., 1994; purple dots are from Hodell et al., 1991; green dots are from Oslick et al., 1994

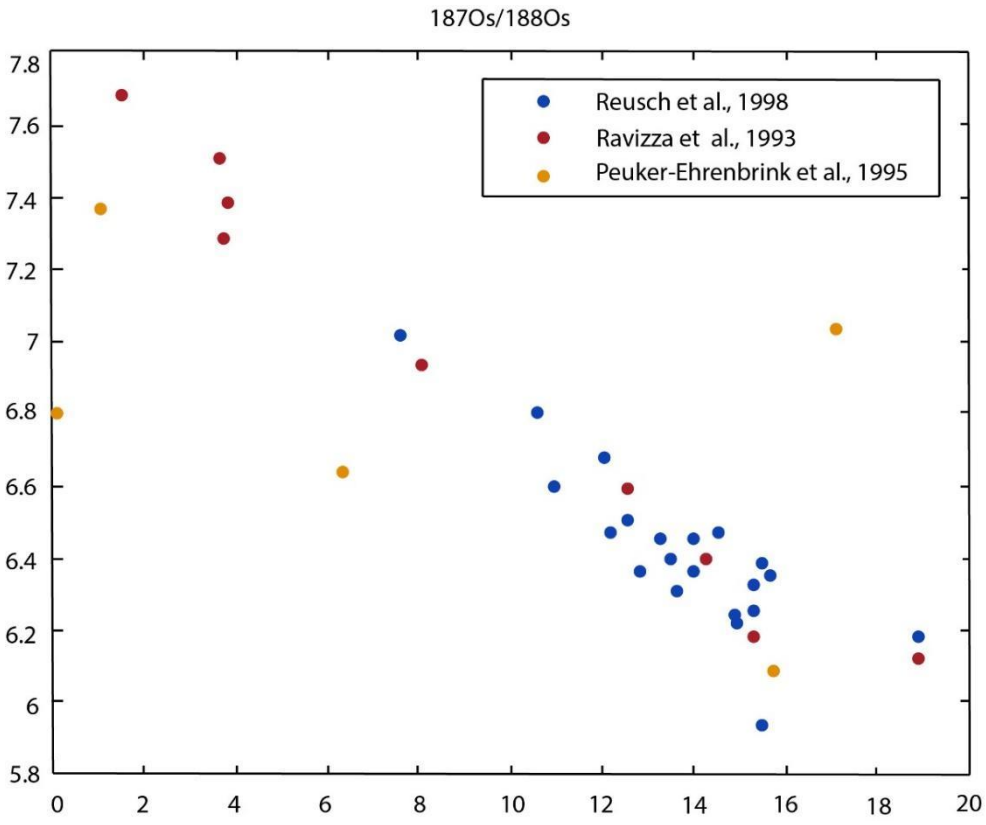

Figure 2.11 $^{187}Os/^{188}Os$ *ratio of seawater inferred from analysis of metalliferous carbonates. Blue dots are from Reusch et al., 1998; orange dots are from Ravizza et al., 1993 and yellow dots are from Peuker-Ehrenbrink et al., 1995*

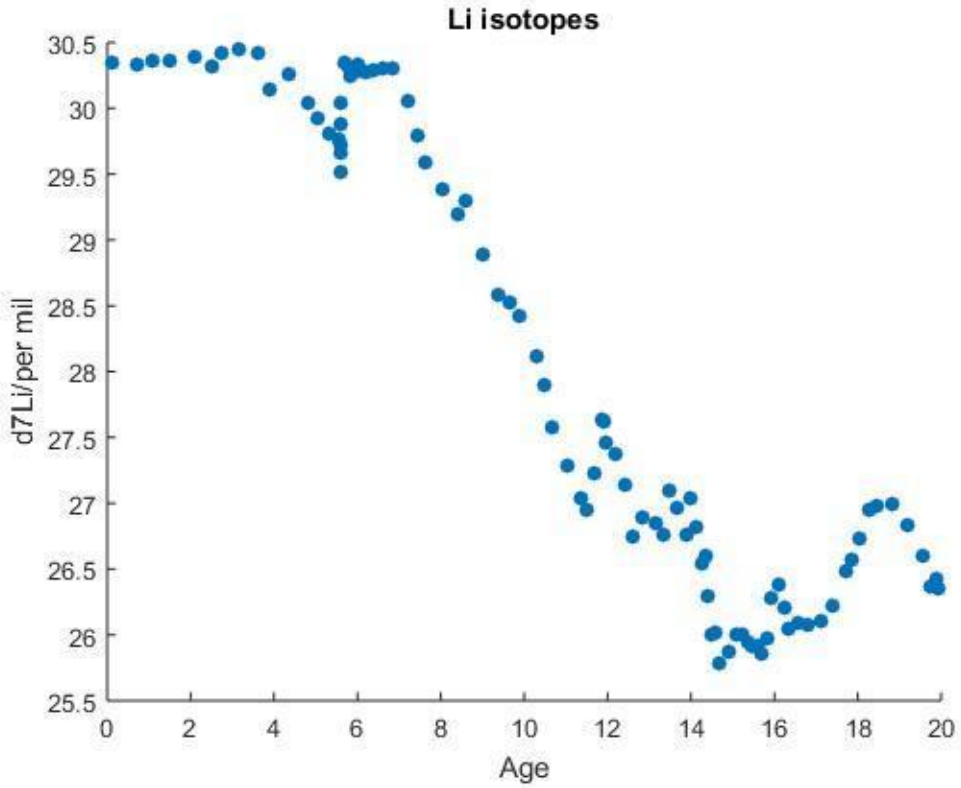

Figure 2.12 5-point-running mean of δ^7Li foraminfera record. Data are from Misra and Froelich, 2012

Study site

IODP Leg 320/321, Site U1337A (3°50.009′N, 123°12.352′W; 4463 meters below sea level [mbsl]) was selected to be the study site for our purpose. This site was drilled in May 2009 to study paleoceanography events from early to middle Miocene and it is on 24 Ma crust. This site is part of the Pacific Equatorial Age Transact and is on a plateau with thick sediments accumulated. Site U1337 had been within ±2° of equator between 8 to 24 Ma, and its location is currently north of the equatorial high productivity zone. Site U1337 is 1.6° east and 1.3° south of the best age-control DSDP site 79 and they are on the same ridge segment. The Oligocene-Miocene boundary also marks the beginning of an increase in the abundance of diatoms. Hole U1337A section 25X-section 40X, 30-35 cm intervals were selected for this study. The age covers 11.1-18 Ma, the depth is between 245 to 409 m CCSF-A (core composite depth below seafloor). The sedimentation rate is ~21 m/Ma during middle Miocene. The diatom assemblage is primarily pennate taxa, *Thalassiothrix spp.*

Age Model

The age model was constructed by Tian et al. (2013). The initial age model of U1337 was a polynomial fit of planktonic foraminifera datums, radiolarian datum events, nannofossil datums and magnetic events. A standard biostratigraphic event used for the Miocene chronology, B *Discoaster petaliformis* with middle point of EAIE - East Antarctic Ice sheet Expansion (a sharp increase in the benthic $\delta^{18}O$) is adopted to better

constrain the depth interval of 272.64- 355.77 mcd (meters composite depth). The depth of middle point of B *D.petaliformis* datum is 352.82 mcd, and the corresponding age is 15.7 Ma (Exp 320/321 shipboard scientific party, 2010). The EAIE event is globally comparative and the middle point of this event is at 316.93 mcd corresponding to 13.86 Ma (Tian et al., 2009; Holbourn et al., 2005). The initial age model was improved by tuning $\delta^{18}O$ to the obliquity cycles of the astronomical solution from Laskar et al. (2004). The $\delta^{18}O$ record displays strong cycles of eccentricity (100 ka) and obliquity (41 ka) while the precession cycle (21 ka) is weak. The tuning was done by aligning the data time series to that of the obliquity frequency with the "Linage" module from the software Analyseries 1.2 (Paillard et al., 1996). The tuned records have the same phase relationship between $\delta^{18}O$ and $\delta^{13}C$ as the untuned record at specific orbital cycles. Applying this model to Site U1337A depth interval of 245.08-407.4 mcd, the corresponding age is 11.32-18.30 Ma.

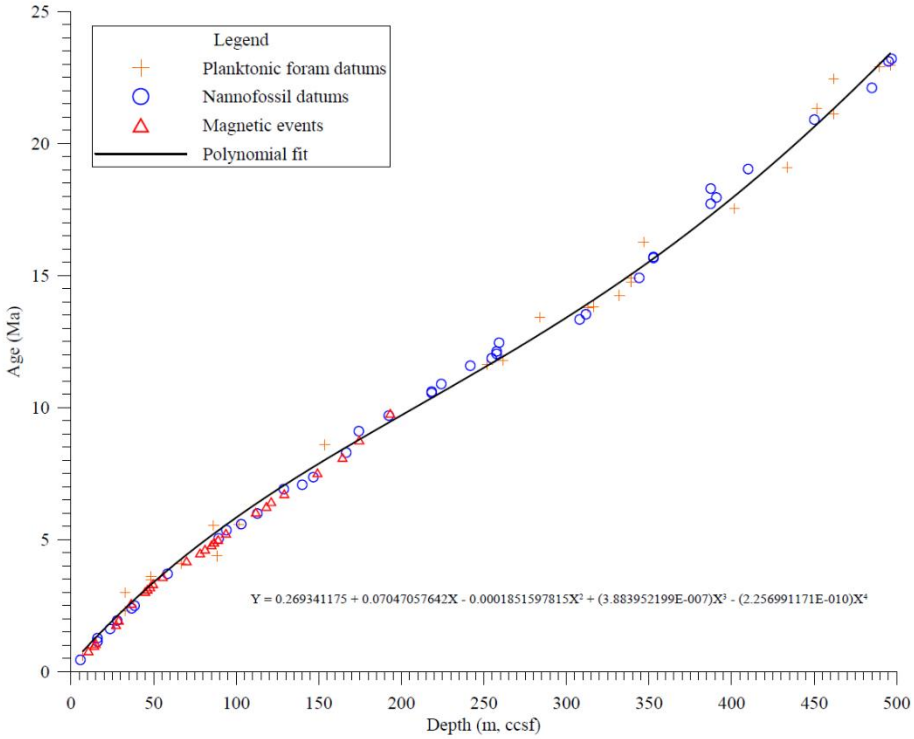

Figure 2.13. Site U1337 age model, Tian et al., 2014

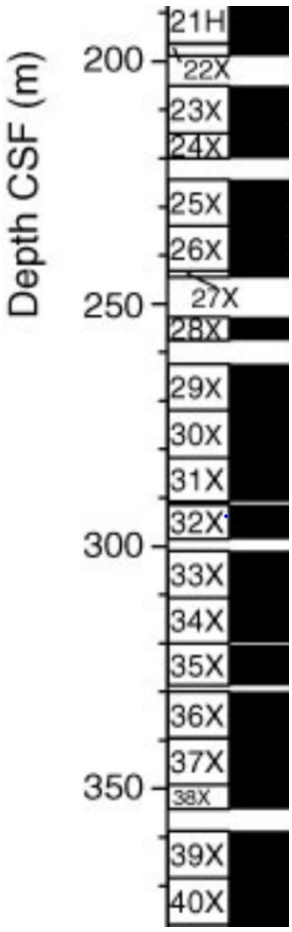

Figure 2.14 ODP SiteU1337A core summary of selected samples, Proceeding of the Integrated Ocean Drilling Program, Volume 321/321

Table 2.1 Depth and age summary of for selected samples

Sample ID	Depth	Age	Sample ID	Depth	Age
25-1S	245.08	11.322	33-6S	335.98	14.899
25-2S	246.78	11.384	34-1S	339.36	15.046
25-4S	249.6	11.487	34-2S	340.85	15.112
25-5S	251.09	11.541	34-3S	342.35	15.177
25-6S	252.58	11.596	34-4S	343.85	15.244
25-7S	253.6	11.634	34-5S	345.35	15.310
26-1S	254	11.648	34-6S	346.89	15.378
26-2S	255.9	11.718	35-1S	348.33	15.443
26-3S	257.4	11.774	35-2S	349.83	15.510
26-4S	258.9	11.829	35-3S	351.33	15.577
26-5S	260.44	11.886	35-4S	352.83	15.645
26-6S	261.9	11.940	35-5S	354.33	15.713
26-7S	262.9	11.978	35-6S	355.83	15.781
27-1S	266.96	12.129	36-2S	360.25	15.984
28-1S	272.61	12.342	36-3S	361.76	16.053
28-2S	274.12	12.399	36-4S	363.25	16.122
28-3S	275.63	12.457	36-5S	364.74	16.192
28-4S	276.62	12.494	36-6S	366.25	16.262
29-1S	284.9	12.812	36-7S	367.65	16.328
29-2S	286.42	12.871	37-1S	368.86	16.385
29-3S	287.94	12.930	37-2S	370.37	16.456
29-4S	289.44	12.988	37-3S	371.86	16.527
29-5S	290.94	13.047	37-4S	373.35	16.597
29-7S	293.41	13.144	37-5S	374.89	16.671
30-1S	300.42	13.421	37-6S	376.34	16.740
30-2S	301.89	13.480	37-7S	377.36	16.789
30-3S	303.41	13.541	38-1S	379.01	16.869
30-4S	304.9	13.601	38-2S	380.5	16.941
30-5S	306.42	13.662	38-3S	382.05	17.017
30-6S	307.88	13.721	38-4S	382.99	17.062
30-7S	309.39	13.783	39-1S	388.05	17.311
31-3S	313.2	13.939	39-2S	389.54	17.385
31-4S	314.68	13.999	39-3S	391.03	17.459
31-5S	316.18	14.061	39-4S	392.55	17.535
31-6S	317.68	14.123	39-5S	394.03	17.609
32-1S	319.475	14.198	40-2S	401.34	17.980
32-2S	321.27	14.273	40-3S	402.87	18.058
32-5S	325.81	14.464	40-4S	404.3	18.132
33-2S	329.98	14.641	40-5S	405.9	18.215
33-4S	333	14.770	40-6S	407.4	18.292
33-5S	334.5	14.835			

CHAPTER 3

METHODS

Cleaning Procedure

We followed the cleaning method developed by Shemesh and Mortlock (1988). 3 to 5 g of sediment sample was weighed into a Teflon beaker. 100 ml of 1M HCl and 100 ml of 10% H_2O_2 were added to the beaker. Then the beaker was placed on a hot plate for 5 hours at 50°C. This step is to remove carbonates and organic matter from the sample. The beaker was removed from hot plate and covered for 3 to 4 hours to cool and allow sediments to settle. The supernatant was decanted and discarded. 200 ml of 5% sodium hexametaphosphate was added to the beaker followed by 3-minute sonication. The beaker was placed on hot plate and covered with a Teflon disk. The mixture was brought to a boil for 15 minutes, then removed and cooled down for ~3 hours until the solids settled to the bottom. The supernatant was decanted and discarded.

The solids were washed through 62 μm sieves first, and the >62 μm portion was washed twice to remove residual clays. This part was collected and kept in a 50 ml centrifuge tube. The >62 μm portion contains large diatoms, coarse detrital grains and radiolarians that fractionate Ge/Si from that of seawater value (Shemesh et al., 1988). The <62 μm portion was passed through a 40 μm sieve; the <40 μm part contains diatoms, sponge spicules and some clay residuals, this fraction was collected and washed through 10 μm sieve to remove clays. The 40-62 μm solids were discarded due to low opal content. The

<40 μm fraction was transferred to a Teflon beaker. 200ml of 1% sodium hexametaphosphate solution was added to the beaker, this fraction was boiled for 15 min then sonicated for 2 min and set aside for 1-2 hours until most diatoms settle out. The supernatant was removed with a syringe and the process repeated for multiple times as needed. The final products were visually examined (they should be transparent or white), then saved in a 50ml centrifuge tube. The >62 μm portion and <40 μm portion were dried in a drying oven overnight at 60 ℃. At this point, several samples had been checked under optical microscope to see if clays were removed and what sort of material remained in the opal samples.

1g of hydroxylamine hydrochloride ($HN_2OH•HCl$) was dissolved in 10 ml DI water, then transferred into 100 ml 20% glacial acetic acid. 5 ml of 1% $HN_2OH•HCl$ in HOAc and 20 ml DI water were then added to the tube. The mixture was capped and swirled, then placed in a boiling water bath for 1 hour. Tubes were removed from water bath, and 20 ml DI water was added to each tube immediately. Next, tubes were sonicated for 1 min and centrifuged for 3 min at 3500 rpm. The supernatant was syringed off and discarded. 45 ml DI water was added to tubes, and tubes were sonicated and centrifuged. The supernatant was again syringed off and discarded. This DI water wash-sonication-centrifuge procedure was repeated 3 times. The tubes were placed in drying oven overnight at 60 ℃.

Opal Extraction

15-18 mg of dry cleaned opal sample was weighed into a 50 ml centrifuge tube. 40 ml of 2M Na_2CO_3 solution was added to the tube. The tube was capped and swirled then placed in water bath at 85℃ for 5 hours. Every 1 or 2 hours, the tube was shaken and sonicated for 1 min to promote opal dissolution. The opal solution was centrifuged for 3 min immediately after the water bath. 5 ml of the supernatant was transferred to another 50 ml tube and acidified to neutral pH. The solution was diluted to 20 ml for Ge and Si analysis. The final Na_2CO_3 concentration is 0.5M.

Ge/Si determination

Dissolved Si was determined by ICP-OES (AMETEK Spectroblue), and dissolved Ge was determined by hydride-generation ICP-MS (Thermo-Finnigan Element 2). For Ge determination, instrument tuning was carried out by introducing a 100 ng/L Ge standard into the hydride generation system and adjusting gas flows and other parameters to optimize the count rate between 250,000-500,000 cps. All measurements were made in ion counting mode. Samples and standards were introduced to the hydride system with 4% $NaBH_4$ solution. During this process, germanic acid ($Ge(OH)_4$) was reduced to volatile germane (GeH_4) by $NaBH_4$. Then the GeH_4 was transported by argon gas into ICP-MS for determination. Check standards of 100 ng/L were bracketed throughout the analysis in order to monitor signal intensity drift and $^{70}Ge/^{74}Ge$ ratio drift. The isotope dilution method was adopted to obtain a precise Ge analysis. A small amount of high

$^{70}Ge/^{74}Ge$ ratio spike was added to each sample and equilibrated overnight at room temperature. The ratio of $^{70}Ge/^{74}Ge$ in the spike is 162 and that of natural abundance is 0.56. The target $^{70}Ge/^{74}Ge$ ratio of sample is 10, and the actual spiked samples were made up to a $^{70}Ge/^{74}Ge$ between 5 to 10, near the geometric mean of the spike and normal values (9.5247). The uncertainty of isotope dilution analysis is lowest near this target ratio (Mortlock and Froelich, 1996). Ge was quantified both by a standard curve method using ^{74}Ge, and by isotope dilution using $^{70}Ge/^{74}Ge$ ratio. The standard curve is composed of analysis of Ge standard with concentration at 5, 20, 50, 100, 200 and 500ng/L. Corrections for background, mass bias and signal drifting were done using sample-standard bracketing. The background signal at mass (*m/z*) 70 is ~4400 cps, 7.6% of total counts, for *m/z* = 72 is ~6500 cps, 8% of total counts and for *m/z* = 74 is ~1400 cps, 1.6% of total counts. The typical mass bias is ~1% per amu, the lowest mass bias is around 0.5%, and the highest is around 1.4%. A 100 ng/L Ge solution was prepared by serial dilution of a 1000 µg/ml standard solution (*SPEX CertiPrep*) and was used for a check standard. The final results were calibrated under both standard curve regression and isotope dilution for cross check. The standard curve corresponds to ^{74}Ge, since the $^{70}Ge/^{74}Ge$ ratio is 162, the contribution from spike is negligible to samples. A 10 ppt (ng/L) Ge standard spiked to a $^{70}Ge/^{74}Ge \approx 10$ was checked through multiple analysis. The results from multiple analysis of the spiked 10 ppt Ge standard are stable and reproducible; most of the differences between calculated standard and measured value are less than 1%, and the largest difference is 1.6%.

Si concentrations were calibrated using a standard curve that includes 1, 2, 5, 10, and 20 ppm Si standards. Samples were bracketed by a 1 ppm check standard. The standard solutions were made in a Na_2CO_3 matrix of 0.5M which is the same with that of samples.

Table 3.1 Ge measurement uncertainties for multiple runs

date	measured	standard	difference
7/27/2018	10.05	10.12	-0.70%
	9.96	10.12	-1.60%
	10.03	10.12	-0.90%
	10.14	10.12	0.20%
	10.23	10.12	1.10%
8/3/2018	10.25	10.12	1.30%
	10.12	10.12	0.00%
10/9/2018	9.98	10.01	-0.30%
	10	10.01	-0.10%
	9.97	10.01	-0.40%
	10.01	10.01	0.00%
	9.96	10.01	-0.50%

The trace elements aluminum and iron were analyzed by both ICP-OES and ICP-MS to confirm whether the cleaning procedure is effective. In all cases Al and Fe were below detection limit for the ICP-OES.

Sponge spicules were found in the sample by microscopic inspection. The fraction of sponge to total biogenic silica was estimated by image analysis using an optical microscope and "Image J" software. 5 samples were selected for this analysis, see results in Appendix Table 16. Pictures of sample were taken under the microscope, then each sponge and diatom frustule were outlined and the area of the polygon were calibrated by "Image J". The average value obtained from multiple fields of view was

taken for the same sample. The purpose of this estimation is to have a better knowledge of Ge/Si measured from the sample, because sponge spicules tend to have different Ge/Si ratio from diatom. The Ge/Si of modern sponges is 0.23±0.12μmol/mol (Baronas et al., 2017). A Ge/Si ratio correction was made for the Ge/Si ratio we measured.

3.1) $R_{sp}F_{sp}+R_{dm}F_{dm}=R_{measure}$

3.2) $R_{dm}=(R_{measure}-R_{sp}F_{sp})/F_{dm}$

Where R_{sp} is Ge/Si ratio of sponge, R_{dm} is Ge/Si ratio of diatom. F_{sp} is the fraction of sponge in total biogenic opal and F_{dm} is the fractionation of diatom in total biogenic opal. $R_{measure}$ is Ge/Si ratio we measured.

Here we assign $R_{sp}=0.2$, $F_{sp}=10\%$, $F_{dm}=90\%$.

3.3) $R_{dm}=(R_{measure}-0.02)/0.9$

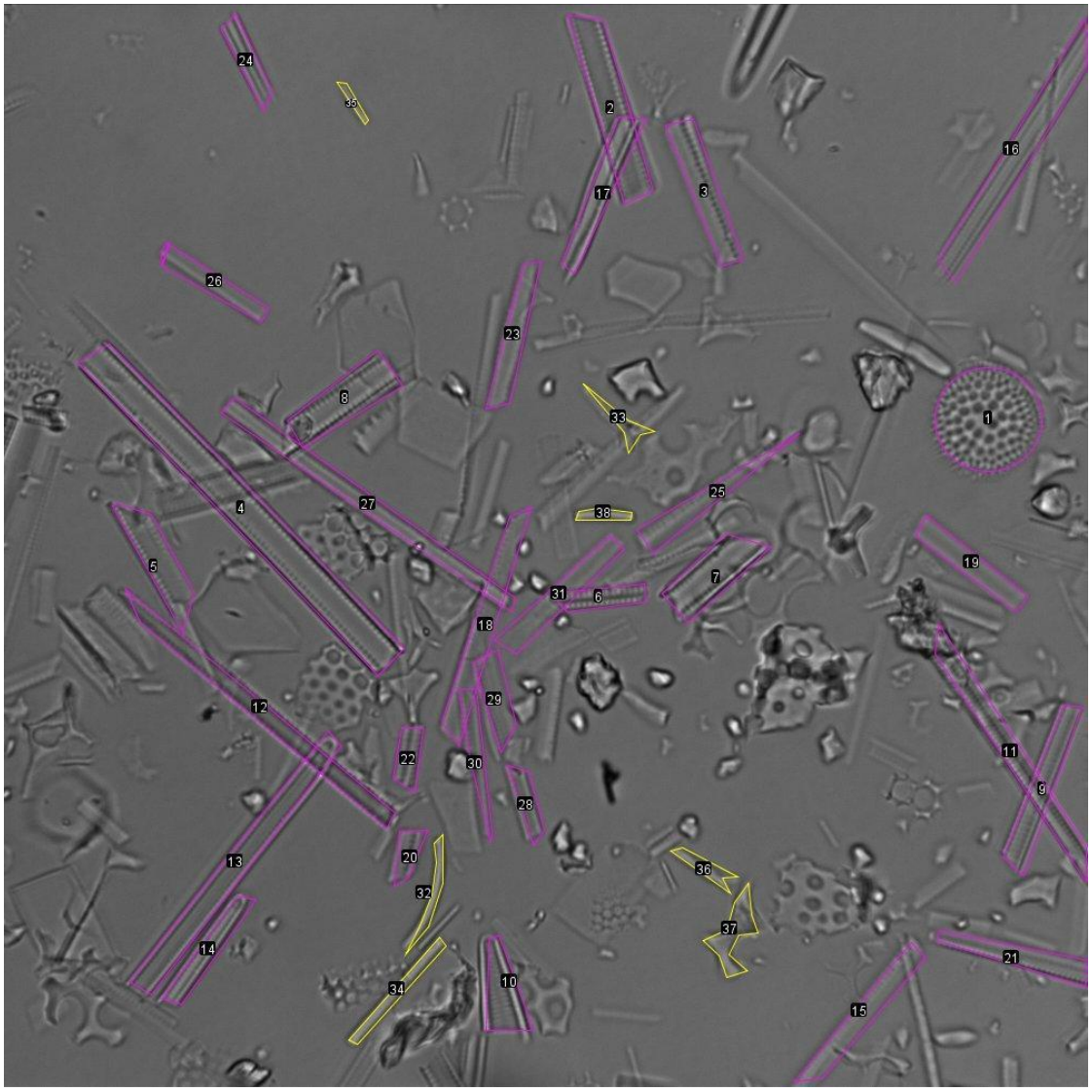

Figure 3.1 Samples under optical microscope, diatoms are outlined by red lines, and sponge spicules are outlined by yellow lines

CHAPTER 4

BOX MODEL

Ge/Si Box Model

This model was constructed to test different weathering regimes and see which of them can lead to Ge/Si ratios that are consistent with our data. The model consists of a single box representing the oceans, consistent with the well mixed and uniform values of Ge/Si in the oceans (Froelich et al., 1992). The model has specified inputs (sources) of Ge and Si. Outputs are either specified or treated as a first-order rate law with respect to Ge and Si in the oceanic reservoir.

Inputs of Ge and Si to the oceans (sources)

The sources of this model come are the river flux, groundwater flux, axial and low-T hydrothermal fluids, dissolution of marine sediments and dissolution of aeolian input. The river flux is the largest flux and has dominant effect on Ge/Si in the ocean. The groundwater flux is 0.6 Tmol/yr (Treguer and De La Rocha, 2013), and we assume this flux does not vary during MMCO. No evidence suggests the hydrothermal flux changed and affected seawater Ge/Si during MMCO, so we assume this flux is also constant. The aeolian flux varies with the glacial - interglacial cycle. Aeolian fluxes are higher during glacial period and lower during interglacial periods. However, for purpose of constructing this model we assume that the effects at million-year scale average out,so

we assume this flux is fixed. Marine sediment dissolution is assumed to be congruent and does not change in this model.

Removal of Ge and Si from the oceans (sinks)

There are two processes that remove dissolved Ge and Si from seawater: biogenic opal production and authigenesis. Plankton, microorganisms, animals and plants can take up Si from seawater. Our model includes Si and Ge removal by sponges and diatoms. Authigenesis is a process that traps Ge and Si and converts them into secondary clays, involving reverse weathering and Ge sequestration. Biogenic opal production is the major sink for Si in the ocean and removes Ge, but marine authigenesis removes Ge more efficiently than Si.

Conceptual Description

The Si fluxes are estimated by Treguer et al. (2013). The non-opal sink is based on the Ge sequestration associated with iron oxides estimated by Baronas et al. (2017); Si export is negligible in this process. The initial ocean Ge/Si is set to be 0.7 μmol/mol. The Ge/Si ratio of river, groundwater, marine sediment, hydrothermal flux and sponges are from Baronas et al (2017). The aeolian Ge/Si ratio is from Kurtz (2000), and diatom Ge/Si ratio is from Mortlock et al. (1989). The Ge/Si ratio associated with reverse weathering is assigned to make the model at steady state. Small adjustments within uncertainties have been made to make output fluxes balance input fluxes. The Si

reservoir has 97000 Tmol of Si (Treguer et al., 2013), the total input flux is 11.3 Tmol/yr, yielding the residence time of 8584 years. The Ge reservoir size is 67900 Mmol, the total input is 22.3 Mmol/yr, and the residence time is therefore 3044 years.

The box model is based on several equations

4.1) $\frac{dSi}{dt} = Si_{input} - Si_{output}$

where

4.2) $Si_{input} = F_{river} + F_{groundwater} + F_{marinesediment} + F_{dust} +$

$F_{axial\ hydrothermal} + F_{low-T\ hydrothermal}$,

and

4.3) $Si_{output} = F_{diatom} + F_{Sponge} + F_{reverseweathering}$

The terms F_i refer to silica fluxes into or out of the oceans.

4.4) $\frac{dGe}{dt} = Ge_{input} - Ge_{output}$

where Ge_{input} has the same sources as Si, and the Ge fluxes are defined by Ge/Si ratio of different sources.

4.5) $Ge_{input} = Ge_{river} + Ge_{groundwater} + Ge_{marinesediment} + Ge_{dust} +$

$Ge_{axial\ hydrothermal} + Ge_{low-T\ hydrothermal}$

where

4.6a) $Ge_{river} = Ge/Si_{river} \times F_{river}$,

4.6b) $Ge_{groundwater} = Ge/Si_{groundwater} \times F_{groundwater}$,

4.6c) $Ge_{marinesediment} = Ge/Si_{marinesediment} \times F_{marinesediment}$,

4.6d) $Ge_{dust} = Ge/Si_{dust} \times F_{dust}$,

4.6e) $Ge_{axial\ hydrothermal} = Ge/Si_{axial\ hydrothermal} \times F_{axial\ hydrothermal}$,

4.6f) $Ge_{low-T\ hydrothermal} = Ge/Si_{low-T\ hydrothermal} \times F_{low-T\ hydrothermal}$

4.7) $Ge_{output} = Ge/Si_{sw}\left(Ge_{diatom} + Ge_{sponge}\right) + reverse\ weathering + nonopal\ sink$

Here, we simulated the Si and Ge reservoir respectively, and we can calculate Ge/Si ratio by dividing the results of equation (4.1) with equation (4.4).

4.8) $\frac{Ge}{Si_{sw}=\frac{M_{Ge}}{M_{Si}}}$

Where M_{Ge} is the amount of Ge in the ocean, and M_{Si} is the amount of Si in the ocean. The unit here is Tmol (10^{12} moles).

The weathering intensity is associated with Ge/Si_{river}, and weathering extent is linked to F_{river}. When weathering is more incongruent, the riverine silica flux F_{river} increases which tends to decrease the Ge/Si of seawater. When weathering is more congruent, the Ge/Si_{river} increases, if F_{river} does not change, Ge/Si_{sw} increases as well. Reverse weathering is a sensitive control on Ge/Si ratio, because it is a sink with a high Ge/Si ratio. The oceanic Ge/Si ratio increases with lower reverse weathering extent or Ge/Si ratio. However, the scale of the flux and Ge/Si ratio of reverse weathering still has large uncertainties. More work is required to estimate the Ge/Si ratio and the reverse

weathering flux, especially on how climate change may affect the intensity and extent of reverse weathering. A big ecological community shift could also change oceanic Ge/Si ratio. If the dominant marine silica species were sponges rather than diatoms, the Ge removal efficiency will be low, and Ge/Si ratio of seawater will increase. There is no clear evidence which shows significant long term change in hydrothermal flux over the last 20 Ma. Because we lack a robust estimate for dust fluxes during 15-17 Ma, we begin by using the modern flux of 0.5±0.5 Tmol/yr (Treguer et al., 2013). We think the Miocene dust flux was probably smaller than modern, because northern hemisphere glaciation was much smaller or even absent. Aeolian records from Rea et al. (1994) suggests the dust flux is low during MMCO. The Ge/Si ratio of the dust flux was assigned to be 0.4 μmol/mol. This is lower than the river Ge/Si ratio since only part of the dust dissolves in the ocean, i.e. dust weathering is incongruent (Kurtz, 2000).

Table 4.1 Ge/Si model parameters

Components	Si Flux (Tmol/ka)	Ge/Si (μmol/mol)	Ge Flux (Mmol/Ka)
river	7300	0.5	3650
groundwater	600	0.5	300
marine sediments	1900	0.6	1140
dust	500	0.4	200
axial hydrothermal	500	9	4500
low-T hydrothermal	500	25	12500
Total input	11300		22290
diatom	7000	0.7	4900
sponge	2800	0.49	1372
reverse weathering	1500	7.61	11415
nonopal sink	--	--	4600
Total output	11300		22287

Si flux from Treguer and De La Rocha, 2013
Ge flux and Ge/Si ratio from Baronas et al., 2017
Small adjustments are made to balance inputs and outputs

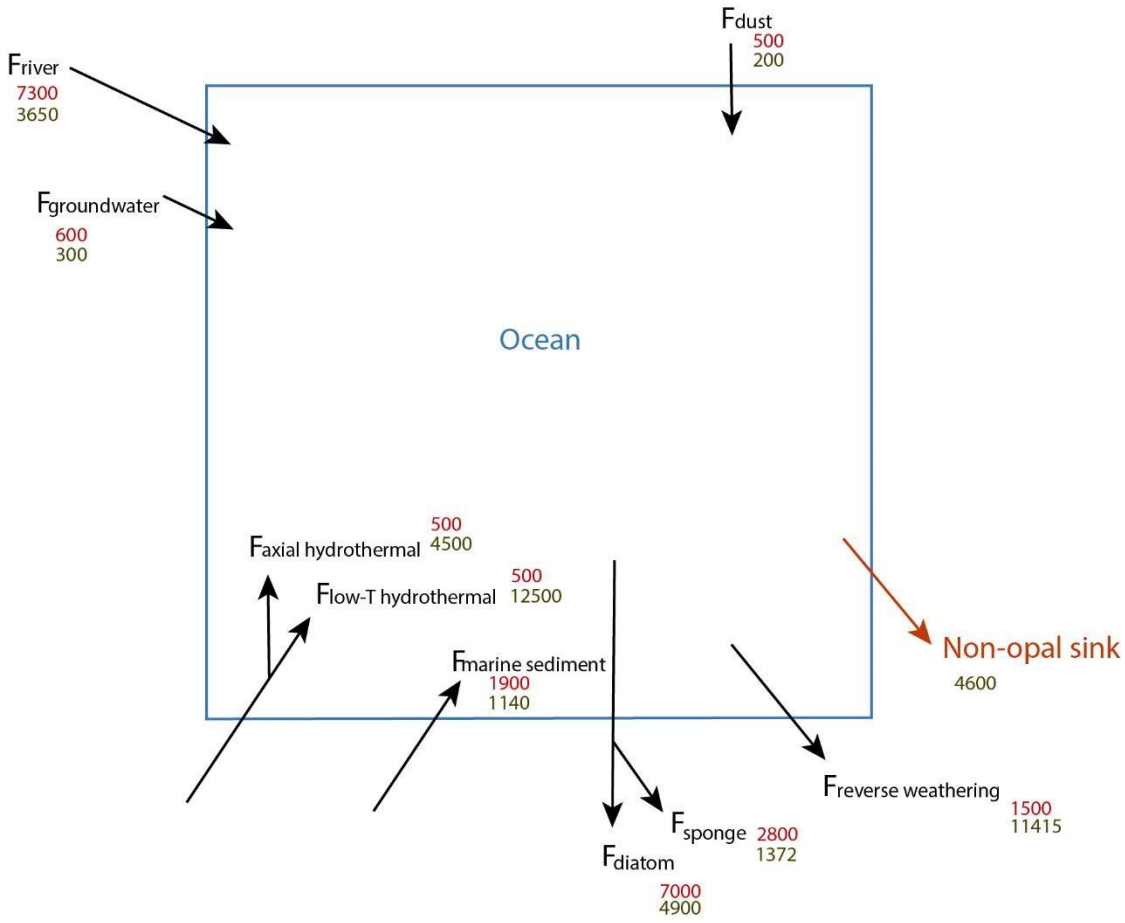

Figure 4.1 Schematic graph of Ge/Si box model. Arrows represent Si and Ge fluxes, red numbers are Si fluxes in Tmol/kyr, green numbers are Ge fluxes in Mmol/kyr

Li box model

The isotopic composition of marine lithium, expressed as δ^7Li, is another indicator of silicate weathering process. δ^7Li is introduced here because it is very similar to Ge/Si in terms of weathering. In addition, δ^7Li does not depend on biology. Li is believed to be closely related to silicate weathering (Misra and Froelich, 2012). Although a small amount of Li exists in carbonates, this tracer is barely affected by carbonate weathering. A Li box model was constructed to test our hypotheses and help us exclude some possibilities. The residence time of Li in the ocean is ~1.2 Ma, much longer than mixing time of seawater (~1000 years). All these features make Li isotopes a potentially useful weathering tracer.

We adapted the Li box model built by Misra and Froelich, 2012. The input fluxes of Li box model include river flux, high-temperature hydrothermal flux and subduction reflux. The output fluxes include the formation of marine authigenic aluminosilicate clays (MAACs) and altered oceanic crust (AOC). The fluxes and Li isotopic signature of each fluxes are based on present values from Misra and Froelich (2012). The flux of river and hydrothermal fluids are on the same scale, the river flux is 10 Gmol/yr and hydrothermal flux is 13 Gmol/year. The river flux has a higher δ^7Li signature than hydrothermal fluids, and high-temperature hydrothermal fluids have a Li isotope composition of 8.3‰. The δ^7Li of the river flux exhibits a wide spread in global rivers, but the average value is ≈23‰. The δ^7Li of river water is controlled by weathering intensity. Secondary minerals are enriched in ^{6}Li, thus when weathering intensity is high,

the δ^7Li of river will increase as more ^{6}Li is released from dissolution secondary clays. 60 Ma ago, the river δ^7Li is estimated to have been 3‰ at steady state and the ocean δ^7Li was 22‰ (Misra and Froelich, 2012). Assuming other fluxes and their isotopic composition are constants, based on the δ^7Li record, the ocean during the MMCO δ^7Li is ~25‰. To reach steady state of 25‰, the river δ^7Li needs to be 5.7‰ in our model. The subduction reflux term represents is Li released to seawater during subduction. The subduction reflux is estimates to be 6 Gmol/yr with a δ^7Li of 15‰. This term is assumed to be constant in this model and so does not have effect on the variation of seawater δ^7Li. Marine authigenic aluminosilicate clays (MAAC) and altered oceanic crust (AOC) are products formed during reverse weathering, and this Li sink has a δ^7Li dependent on seawater Li isotopic composition. The δ^7Li of MAAC and AOC is 16‰ lighter than seawater δ^7Li (Misra and Froelich, 2012). The model can be expressed as below:

4.9) $\frac{dLi}{dt} = F_{river} + F_{HT} + F_{sub} - F_{rw}$

4.10) $\frac{\delta^7 Li}{dt} = \frac{1}{Li}[\delta^7 Li_{riv} + F_{HT}\delta^7 Li_{HT} + F_{sub}\delta^7 Li_{sub} - F_{rw}(\delta^7 Li - 16‰)) -$

$\delta^7 Li(F_{river} + F_{HT} + F_{sub} - F_{rw})]$

where Li is Mass of Li in the ocean, F_{river} is Li river flux, F_{HT} is hydrothermal flux, F_{sub} is subduction reflux, and F_{rw} is MAAC and AOC fluxes. $\delta^7 Li$ is Li composition of seawater, $\delta^7 Li_{riv}$ is the isotopic composition of F_{river}, $\delta^7 Li_{HT}$ is the isotopic composition of F_{HT}, and $\delta^7 Li_{sub}$ is isotopic composition of F_{sub}.

F_{river} is dissolved Li transported by river to the ocean. This flux is associated with continental weathering. Similar to riverine flux of Si, F_{river} of Li is controlled by weathering extent, and F_{river} of Li increases as weathering extent increases. Only about one fifth of Li weathered from continental crust is dissolved in stream water, the rest is trapped in the secondary minerals (Froelich and Misra, 2014). $\delta^7 Li_{riv}$ is the isotopic composition of F_{river} of Li and it is dependent on weathering intensity. ^{6}Li is enriched in secondary clays, resulting in the offset of isotopic composition between river and continental crust. The δ^7Li of upper continental crust is 1.7‰ and $\delta^7 Li_{riv}$ is 23‰ (Misra and Froelich, 2012). When weathering intensity increases, the $\delta^7 Li_{riv}$ should decrease as more secondary clays dissolved and release ^{6}Li to stream water. F_{HT} is controlled by hydrothermal activities and spreading rate of seafloor and the $\delta^7 Li_{HT}$ is higher than the isotopic composition of MORB by 3.7‰ due to the sequestration of ^{6}Li into Mg-rich greenstone alteration minerals (Misra and Froelich, 2012). $\delta^7 Li_{sub}$ has the same isotopic composition of sediments, flux-weighted average input and reverse weathering. Thus, this flux does not fractionate δ^7Li of seawater. MAAC is responsible 70% of Li removal and AOC removes 30% of Li sinks from ocean. The two sinks have the same isotopic composition of 15‰, lighter than δ^7Li of seawater. This is thought to drive the isotopic composition of seawater to its present heavy value.

Table 4.2 Li isotope model parameters

Input(mol/yr)		δ^7Li(‰)	
Friv	8.00E+09	delriv	5.7
Fhyd	1.30E+10	delhyd	8.3
Fsub	6.00E+09	delsub	15
total input	2.70E+10		
Output(mol/yr)			
AOC+MAAC	2.70E+10	epsRW	16
Tau (years)	1.14E+06		
Mass_Li (moles)	3.08E+16		

After Misra and Froelich, 2012

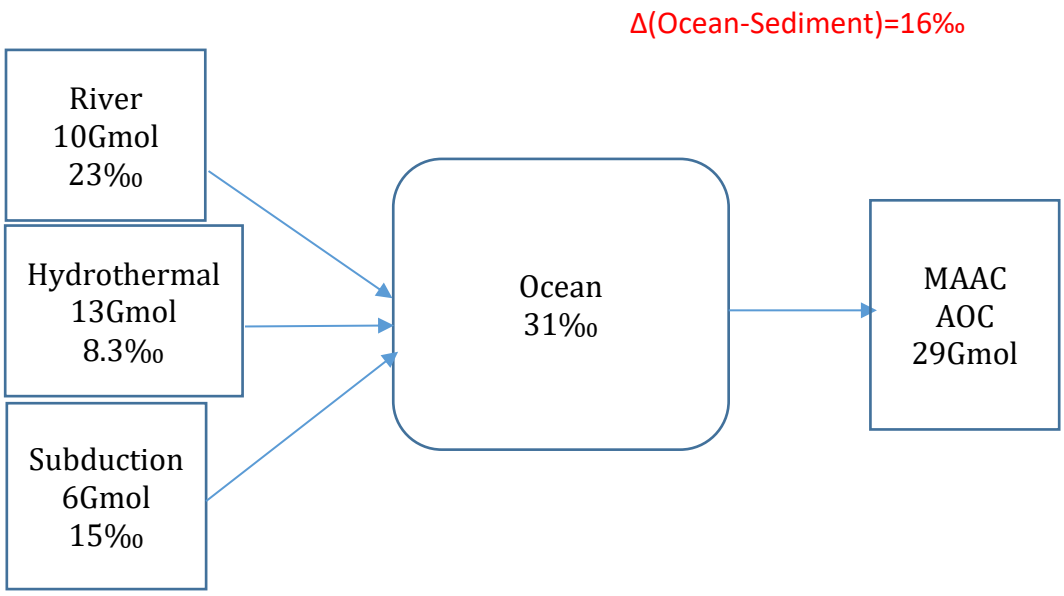

Figure 4.2 Schematic graph of Li box model. Rectangles represent for input and output fluxes of Li in the ocean. The rounded-corner rectangle represents ocean reservoir. Fluxes and isotopic composition are noted in each shape. 16‰ is fractionation factor of Li removal by reverse weathering. Δ represents difference between seawater and sediments. Data from Misra and Froelich,, 2012.

CHAPTER 5

RESULTS

Ge/Si ratio of diatoms from IODP site U1337A

Eighty-one samples of biogenic silica from IODP site U1337A were analyzed for Si, Al, Fe and Ge. The age range is between 11.32-18.29 Ma, with an average temporal resolution of ~0.087 Ma; at some intervals the resolution approaches ~0.05 Ma. Measured Ge/Si ratios are between 0.45-1.0 μmol/mol. Measured Al/Si ratios are between 0.2-16.25 mmol/mol. Measured Fe/Si ratios are between 0-3.67 mmol/mol. (Table 7). The low Al and Fe contents indicate that the cleaning procedures effectively removed detrital and oxide phases (Shemesh et al., 1988).

Table 5.1 Summary of measurement of Si, Ge, Al and Fe for 50 samples. These are the concentrations in the solutions analyzed.

Sample ID	Si (μM)	Ge(pM)	Al(10^{-9}M)	Fe(10^{-9}M)
25-1S	0.318	0.234	1.568	0.041
25-2S	0.266	0.199	2.168	0.215
25-4S	0.194	0.151	0.984	0.063
25-5S	0.285	0.212	1.034	0.066
25-6S	0.262	0.198	1.079	0.065
25-7S	0.281	0.211	1.575	0.104
26-1S	0.314	0.240	1.419	0.059
26-2S	0.135	0.084	0.800	0.058
26-3S	0.263	0.169	1.035	0.084
26-6S	0.194	0.108	0.879	0.062
26-7S	0.227	0.120	0.988	0.088
27-1S	0.293	0.263	0.787	0.045
28-1S	0.160	0.142	1.191	0.096
28-2S	0.318	0.232	1.257	0.073
28-3S	0.131	0.090	0.294	0.005
29-1S	0.189	0.097	0.161	0.003
29-2S	0.318	0.190	0.901	0.089

29-3S	0.284	0.153	0.812	0.153
29-4S	0.180	0.175	0.695	0.070
29-5S	0.180	0.162	0.682	0.069
29-7S	0.277	0.172	0.629	0.068
30-1S	0.297	0.192	1.083	0.274
30-2S	0.196	0.181	0.121	0.003
30-3S	0.319	0.248	0.593	0.067
30-4S	0.256	0.196	0.972	0.127
30-5S	0.192	0.148	0.346	0.045
30-7S	0.138	0.116	0.316	0.045
31-3S	0.134	0.110	2.183	0.288
31-5S	0.315	0.221	0.089	0.004
31-6S	0.298	0.173	0.953	0.084
32-1S	0.323	0.185	0.180	0.001
32-2S	0.272	0.180	0.825	0.092
32-5S	0.344	0.256	1.195	0.070
33-2S	0.248	0.164	0.630	0.122
33-4S	0.205	0.130	0.466	0.045
34-1S	0.328	0.238	0.494	0.098
34-2S	0.276	0.142	0.521	0.095
34-6S	0.387	0.229	0.077	0.002
35-3S	0.184	0.140	1.339	0.232
35-4S	0.192	0.141	0.306	0.002
35-5S	0.275	0.202	1.233	0.093
35-6S	0.281	0.229	0.252	0.001
36-2S	0.156	0.108	1.323	0.573
36-3S	0.173	0.094	1.091	0.162
36-4S	0.246	0.193	1.048	0.214
36-5S	0.294	0.142	0.508	0.010
36-6S	0.182	0.077	0.480	0.108
36-7S	0.181	0.130	0.584	0.070
38-2S	0.329	0.177	0.116	0.002
39-5S	0.272	0.236	0.278	0.009
mean	0.247	0.172	0.811	0.090
error	0.065	0.049	0.492	0.097

Table 5.2 Summary of Ge/Si ratio, Al/Si ratio and Fe/Si ratio for 50 samples

Sample ID	Ge/Si (μmol/mol)	Ge/Si corrected	Al/Si (mmol/mol)	Fe/Si (mmol/mol)
25-1S	0.735	0.794	4.932	0.130
25-2S	0.747	0.807	8.145	0.808
25-4S	0.780	0.844	5.069	0.324
25-5S	0.742	0.803	3.630	0.233
25-6S	0.756	0.818	4.119	0.246
25-7S	0.751	0.813	5.601	0.371
26-1S	0.764	0.827	4.513	0.188
26-2S	0.622	0.669	5.942	0.431
26-3S	0.640	0.689	3.928	0.317
26-6S	0.556	0.596	4.533	0.320
26-7S	0.529	0.566	4.351	0.387
27-1S	0.896	0.974	2.683	0.152
28-1S	0.888	0.965	7.452	0.603
28-2S	0.731	0.790	3.957	0.229
28-3S	0.690	0.744	2.246	0.041
29-1S	0.512	0.547	0.850	0.014
29-2S	0.599	0.644	2.835	0.279
29-3S	0.540	0.578	2.862	0.538
29-4S	0.971	0.578	3.868	0.390
29-5S	0.902	0.979	3.798	0.387
29-7S	0.619	0.666	2.271	0.244
30-1S	0.646	0.696	3.643	0.923
30-2S	0.925	1.006	0.616	0.014
30-3S	0.779	0.843	1.860	0.210
30-4S	0.768	0.831	3.803	0.498
30-5S	0.772	0.835	1.800	0.236
30-7S	0.837	0.908	2.282	0.323
31-3S	0.823	0.892	16.251	2.141
31-5S	0.703	0.759	0.282	0.012
31-6S	0.581	0.624	3.196	0.280
32-1S	0.572	0.613	0.558	0.004
32-2S	0.660	0.711	3.028	0.338
32-5S	0.743	0.803	3.474	0.203
33-2S	0.662	0.714	2.545	0.492
33-4S	0.636	0.685	2.273	0.220
34-1S	0.726	0.785	1.509	0.299
34-2S	0.514	0.549	1.890	0.345
34-6S	0.592	0.636	0.198	0.004
35-3S	0.761	0.823	7.266	1.259

35-4S	0.737	0.797	1.594	0.009
35-5S	0.734	0.793	4.488	0.338
35-6S	0.814	0.883	0.898	0.005
36-2S	0.689	0.744	8.459	3.665
36-3S	0.541	0.579	6.306	0.936
36-4S	0.784	0.849	4.265	0.871
36-5S	0.482	0.513	1.726	0.035
36-6S	0.424	0.448	2.635	0.591
36-7S	0.720	0.777	3.224	0.388
38-2S	0.537	0.575	0.353	0.007
39-5S	0.868	0.942	1.021	0.033
mean	0.700	0.746	3.581	0.426
error	0.124	0.133	2.695	0.593

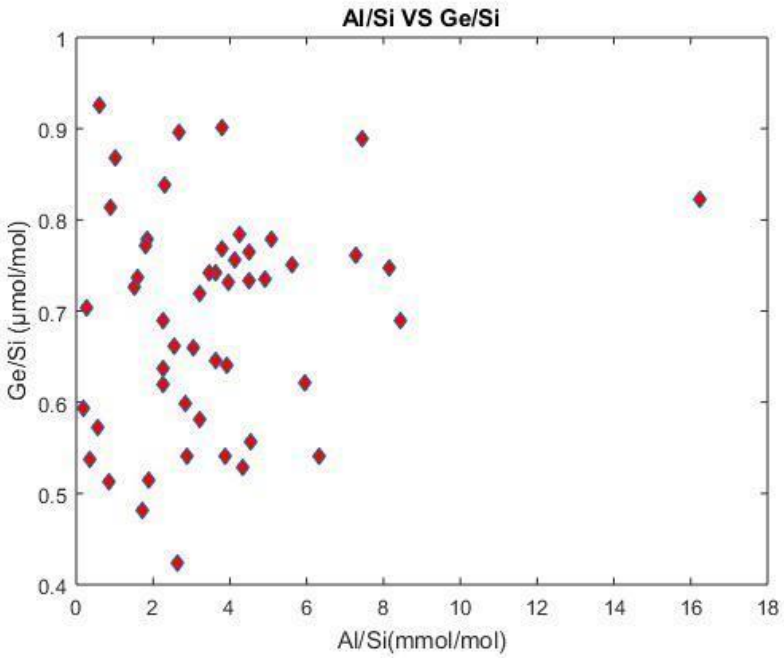

Figure 5.1 plot of Al/Si vs, Ge/Si

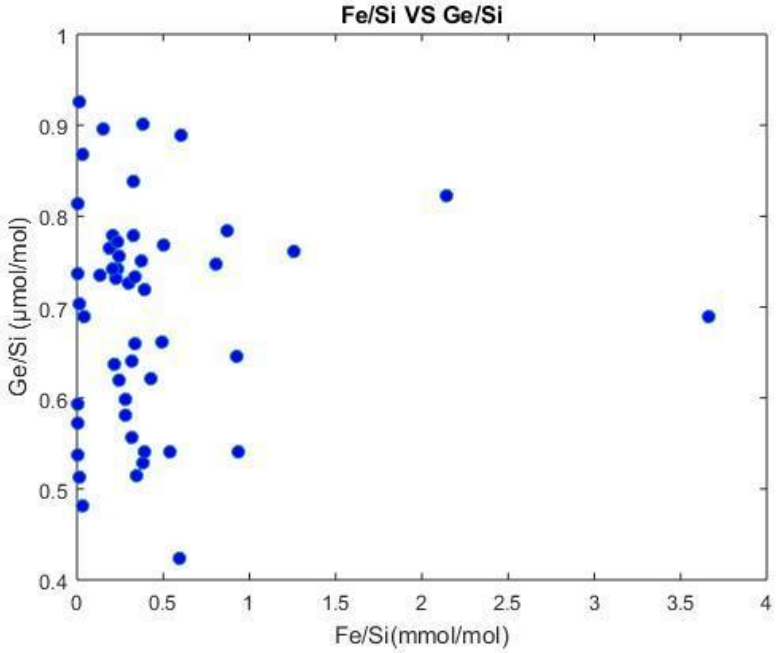

Figure 5.2 plot of Fe/Si vs. Ge/Si

The size fractionation procedure appears to have been effective at removing radiolarians, but it remains possible that there are some unidentified radiolarian fragments in the cleaned samples. Sponges comprise ~10% of total biogenic opal based on inspection by optical microscopic. (Appendix Table 16) The measured Ge/Si ratios were corrected for a contribution from sponge spicules because sponge spicules do not directly record ambient seawater values (Baronas et al., 2017). The correction is implemented using the equation 3.3 described in Methods (Chapter 3).

The Ge/Si value of the sponge component is assumed to be 0.2 (Ellwood et al., 2006). Generally, the correction increased the estimated Ge/Si value of the diatom component by 6-9%. The Ge/Si ratios of the diatom opal (i.e. after correction for the sponge spicule component) range from 0.45 to 1.04 μmol/mol (Appendix Table A1). There is no apparent long-term trend in the data. A linear regression of Ge/Si on age yields a slope of -0.0060 ± 0.0073 (p = 0.41), statistically insignificant and not different from zero. The mean value of all the data is 0.734 ± 0.029 (2 S.E.). Smoothing the data with 3- and 5-point running means does not significantly change the mean or standard error, but does result in a less noisy data set (Figure 5.3, 5.5, 5.6, show all data, 3-pt mean, and 5-pt mean).

There is, however, some evidence for quasi-periodic variations in the Ge/Si ratios from this time interval which are easier to see in the smoothed data. To test whether there could be periodic variation in the data a MATLAB routine was used to fit a 1 term

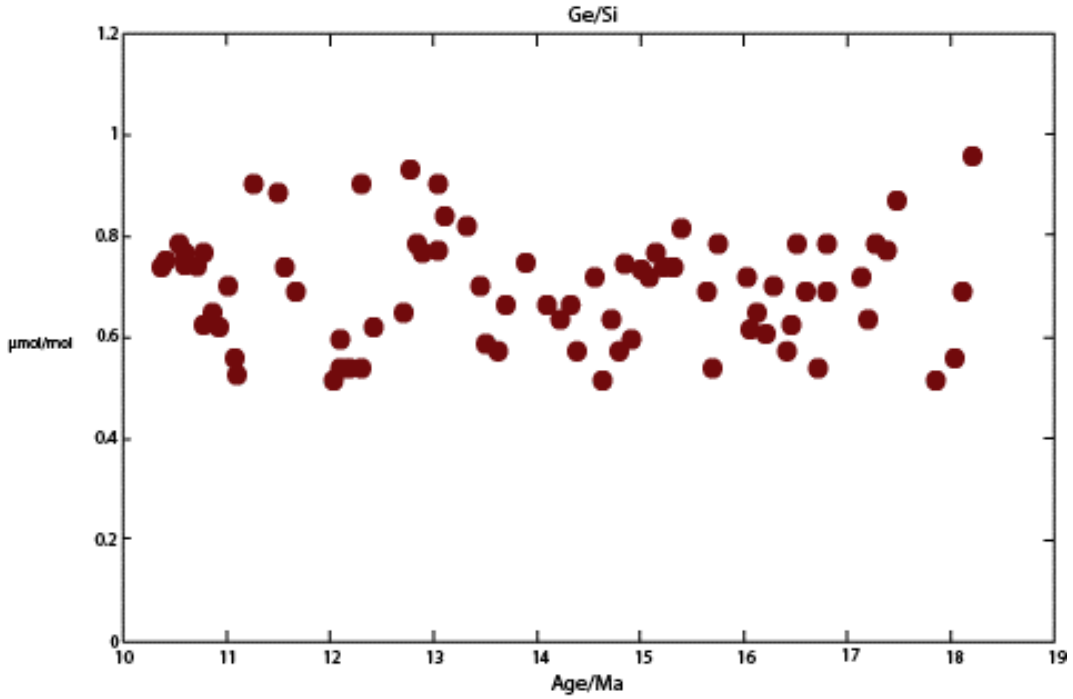

Figure 5.3 Original Ge/Si of U1337A

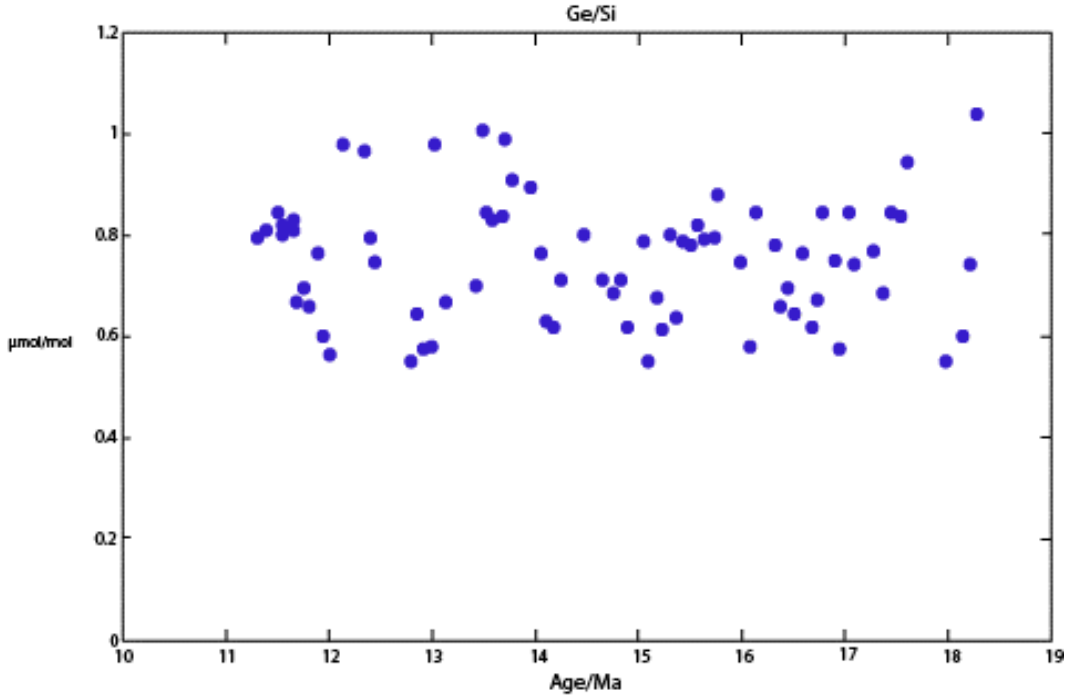

Figure 5.4 Ge/Si corrected with sponge content

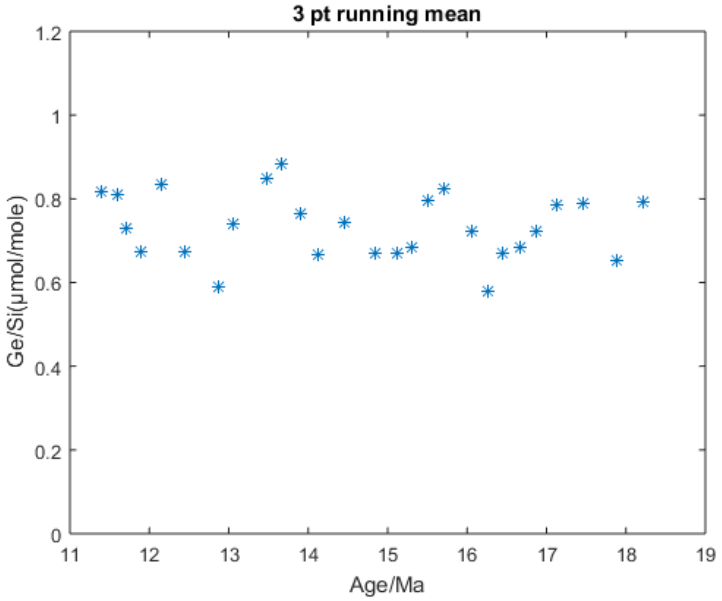

Figure 5.5 3-point running mean of Ge/Si ratio of U1337A

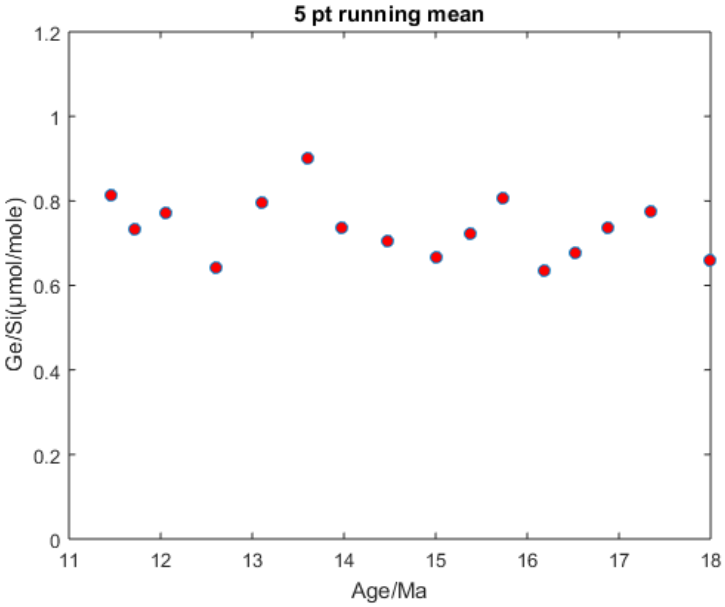

Figure 5.6 5-point running mean of Ge/Si ratio of U1337A

Fourier series model to the entire and smoothed data sets. The 1 term Fourier series model has the form:

5.1) $y = a_0 + a_1\ cos\ cos\ (xp)\ + b_1 sin(xp)$

5.2) $p = 2\pi/[(X)\ - min(X)]$

The MATLAB "fit" routine was used to find a non-linear least squares solution for the Fourier coefficients *a0, a1, b1* and ω, the angular frequency. The algorithm was applied to the full data set (n = 81) and the 3- and 5-point running means (n = 27 and 16, respectively). The results are presented in Figure 5.7 and Table 5.3. Higher order terms did not significantly improve the fit statistics, and the higher order coefficients were mostly within uncertainty of zero, so these results are not presented. The goodness of fit as measure by the r^2 parameter improves with the smoothed data (running means). The Fourier analysis suggests that there is a periodicity to this data of approximately 1.9 Ma. However, the analysis also is near the limit of significance, with even the first Fourier coefficients (a1, b1) not significantly different from zero at the 95% CI. Thus, it remains uncertain whether the apparent periodic signal is robust or meaningful. The variability in the data suggests that diagenesis could have impacted Ge/Si ratios in the opal. Early work on the transition from opal-A (synthesized by diatoms) to more ordered opal-CT indicated that the rate of this transition was significantly controlled by alkalinity and Mg^{++} ions (Kastner et al. 1977). The reaction to opal-CT was believed to be quite slow at low temperature. The samples in this study are from 245 – 407 mbsf.

Table 5.3 Fourier Fit coefficients

		coefficient	uncertainty	R2
3pt	a0	0.727	0.6995	0.3401
	a1	0.03591	-0.2041	
	b1	0.05185	-0.1153	
	w	3.299	2.99	
5pt	a0	0.7226	0.6938	0.5741
	a1	-0.02377	-0.3129	
	b1	0.0681	-0.04055	
	w	3.367	3.08	
all	a0	0.7276	0.699	0.1179
	a1	-0.03047	-0.3067	
	b1	0.05458	-0.1024	
	w	3.379	3.037	

Measured present day down hole temperatures for U1337 form a linear trend from the seafloor (0 m) to 298.1 mbsf (Figure 5.8), which can be given by the following regression:

5.3) T(z), ˚C $= 0.0324(z) + 1.793$

(data from Proc. IODP vol 320/321 doi: 10.2204/iodp.proc.320321.109.2010)

Using this relationship the present day temperatures experienced by the samples in this study (z = 245 to 407 m) range from 8.1 to 13.3 ˚C. A study of silicon isotope variations in pore water and siliceous sediments found that

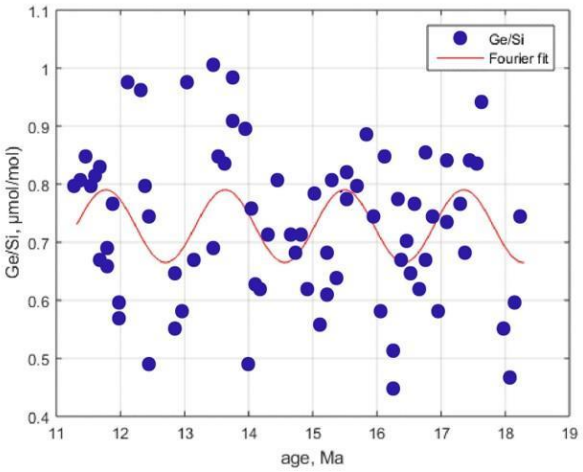

Figure 5.7a Fourier fit for all data

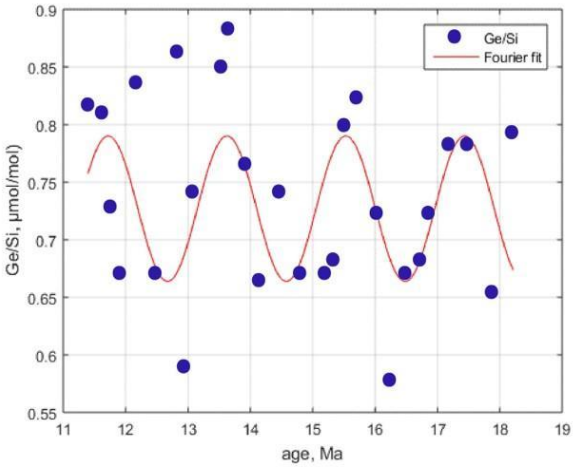

Figure 5.7b Fourier fit for 3-pt running mean

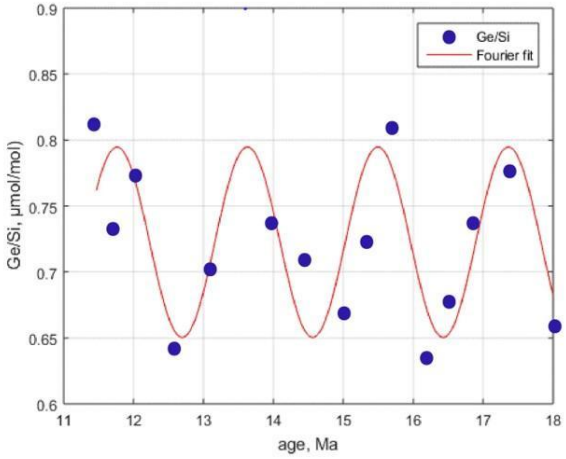

Figure 5.7c Fourier fit for 5-pt running mean

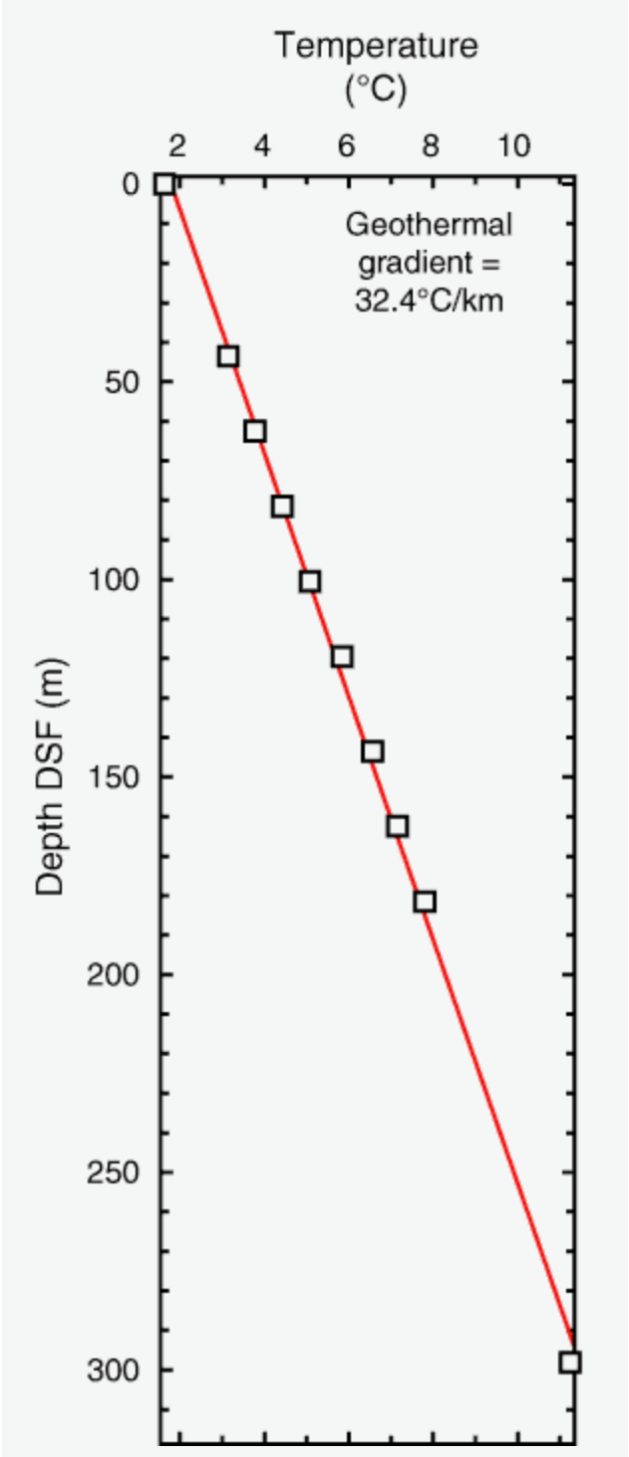

Figure 5.8 U1337 temperature gradient, Sources: Proceedings of the integrated ocean drilling program,volume 320/321, Figure F47

opal-CT recorded pore water values of $\delta^{30}Si$ and that these can be different from seawater (Tatzel et al., 2015 EPSL). It is possible that Ge/Si ratios are also impacted, but the temperatures experienced by the samples are low enough that they should not have transitioned to opal-CT. An alternative hypothesis is that there is variable contamination by sponge spicules (with low Ge/Si relative to diatoms) and radiolarian fragments (high Ge/Si relative to diatoms), and that this is responsible for the variability. This issue requires further investigation.

Comparison with Previous Studies

The data in this study can be compared to the data in Shemesh et al. (1989) (Figure 5.9). Shemesh et al. only have 13 data points in this interval. Their data fall within the range defined by the new data in this study, with the exception of one high outlier at ca. 15 Ma. In general, Shemesh et al.'s data for the period older than 14.5 Ma are in the high part of the range of the data from this study. Their data indicate a drop in marine Ge/Si at around 13.5 Ma from values near 0.9 to 1.0 µmol/mol to values closer to 0.7 µmol/mol, but that shift is not supported by the new data in this study. We do not find clear evidence for this decrease. If we arbitrarily compare the new data for the older interval from 18.29 to 14.00 Ma versus the younger interval from 13.94 to 11.32 the older interval has a mean Ge/Si = 0.711±0.035, while the younger has a mean Ge/Si = 0.768±0.049 (uncertainties are 2 S.E.). For the older interval either Shemesh's low sampling resolution missed the lower values found in this study, or the data in this study

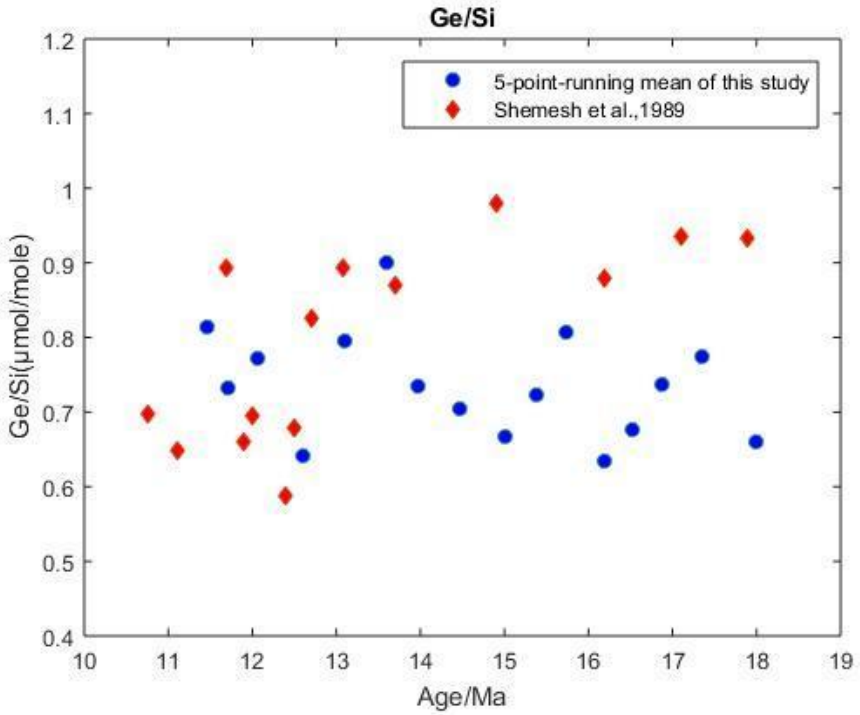

Figure 5.9 Ge/Si ratio. Pink dots are 5pt running mean of this study and red dots from Shemesh et al., 1989.

are more impacted by either diagenesis or incomplete accounting of sponge spicules. The means from the two intervals in the present study do overlap at the 95% CI, and are not statistically distinguishable.

The modern river value for Ge/Si is ca. 0.54 μmol/mol (Froelich et al., 1992, Baronas et al., 2017). Consequently, values in the present data set < 0.6 appear unlikely to be primary, as they are too close to the river value. Removing the samples with Ge/Si ≤ 0.6 (equivalent to a filter with a lower limit of 0.6) leaves 64 samples with a mean Ge/Si = 0.78±0.03 μmol/mol. Including the Shemesh et al. data from 11.1 to 17.9 Ma yields essentially the same result with a mean Ge/Si = 0.78±0.02 μmol/mol, with $n = 77$. This may be a better estimate of the mean value for the mid-Miocene, derived from the present data set and the data of Shemesh et al., 1989. This new filtered combined data set weakens the case for periodic behavior, with r^2 of the 1 term Fourier fit for the filtered data set of only 0.08, and still shows no significant overall temporal trend.

There does appear to be a difference between the mid-Miocene data and the Pleistocene data of Shemesh et al. (1989) and Froelich et al. (1992). Shemesh reported 9 samples younger than 2.78 Ma, with a mean Ge/Si = 0.62±0.02 μmol/mol. Froelich et al. (1992) show clear glacial-interglacial variation, with a total range from 0.54 to 0.78 and a mean near 0.67 (close to the modern value for seawater). The mean Pleistocene value appears to be distinct from the mean mid-Miocene value, although the difference is not as large as suggested by the pre 13.5 Ma data from Shemesh et al. (1989), and the interglacial values overlap with the mid-Miocene values. The mid-Miocene data set does not have

the temporal resolution to capture glacial-interglacial variations that may have existed at that time.

Model experiments

We tested several scenarios that might drive changes in the seawater Ge/Si ratio over time, including for the MMCO, as indicated by proxies discussed in the Chapter 1. Using the mass balance model, we evaluate the impact of flux changes more quantitatively. The same forcing was applied to both the Ge/Si and Li box models as they should respond to similar forcings, although not necessarily in the same way. Based on climate proxies and other weathering indicators during Mid-Miocene, weathering flux and weathering intensity are expected to change in this period. As reverse weathering is an important sink for Ge, Si and Li, this flux should adjust to achieve a new steady state in the ocean. Thus, the changes of weathering flux, weathering intensity and reverse weathering are tested in the model. We use river flux, river isotopic composition to represent weathering flux and weathering intensity as most weathering products are transported by river. Reverse weathering flux of Ge and Si are based on estimation by Treguer et al. (2013) in agreement with estimation from Michalopolous and Aller (2004) and Laruelle (2009). In all tests, hydrothermal fluxes, groundwater flux, marine sediment flux, dust flux and their isotopic composition in Ge/Si box model are fixed. Hydrothermal flux, subduction reflux and their isotopic signature are constant in Li model.

Changes in weathering and reverse weathering fluxes

Results are listed in Figure 5.10 and 5.11. River flux changes for Si and Ge reflect variation in continental weathering. For Scenario 1(a), 1(b), 1(c) and 1(d), the river flux of Si, Ge and Li is increased by 20%, 50%, 100% and 130% when other fluxes are constant. An increase in river fluxes will lower Ge/Si ratio and δ^7Li of seawater, as rivers have low Ge/Si and δ^7Li compared to most of the other inputs. However, the capacity of the river flux to influence the isotopic composition of seawater is limited. In scenario 1(d), a 130% river flux increase leads to only a 0.1 decrease in Ge/Si ratio and 0.1‰ decrease in δ^7Li, corresponding to a decrease of 14.3% and 3.6% with respect to their initial ratios.

Reverse weathering and Ge sequestration are classified as authigenesis, and only reverse weathering flux changes in our model tests. During authigenesis, Ge, Si and Li are removed from seawater via the formation of secondary clays. How this flux is linked to weathering or climate is not clear. In the Ge/Si model, the reverse weathering flux is determined by balancing the global mass budget. In Li model, this Li removal term is dependent on the residence time of Li and the total mass of Li in the ocean. For scenario 2(a), 2(b), 2(c) and 2(d), reverse weathering flux increased by 2%, 4%, 6% and 8%, while other fluxes remain constant. Reverse weathering forms clays with a high Ge/Si ratio and low δ7Li from seawater. Consequently, increasing weathering intensity will reduce the Ge/Si ratio and raise δ7Li of seawater. In scenario 2(d), an 8% increase in reverse weathering flux yields 13.1% decrease in Ge/Si ratio and 1.2% increase in δ^7Li within 2.5Ma, which is 0.61 and 25.3‰ respectively.

Changes in Ge/Si ratio or δ^7Li for different scenario

Besides flux changes, isotopic composition variation is another reason of seawater isotopic signature evolution. An increase in weathering intensity results in river waters with higher Ge/Si ratios and lower δ^7Li values. For scenario 3(a), 3(b), 3(c) and 3(d), the Ge/Si ratio of river flux increases by 10%, 20%, 30% and 40%, and δ^7Li decreases by 10%, 20%, 30% and 40%. Other fluxes are set to be constant. In Scenario 3(d), a 40% Ge/Si increase of river flux results in 0.16 increase in seawater Ge/Si ratio. A 40% δ^7Li decrease of river flux reduces seawater δ^7Li to 24.3‰. Compared with original steady state value, Ge/Si ratio increases by 22.9% and δ^7Li decreases by 2.64%. In scenario 3 group, isotopic composition of other fluxes remains constant.

Table 5.4 Ge/Si model experiment scenarios. From left to right, column 1 is ID for different model experiments, Scenario 1 corresponds to river flux increase. Scenario 2 increases reverse weathering flux and Scenario 3 increases weathering intensity (Ge/Si ratio of river). From a to d, the amount increases from small to large. Column 2 tells which variable is changing in the scenario. Column 3 tells how much the variable in column 2 changes. Column 4 is the flux or Ge/Si ratio used in the corresponding scenario. Column 5 is the Ge/Si ratio of ocean at steady state for each scenario.

scenario	variable	% increase	flux or ratio	result
1a	Friver	20%	8760	0.673
1b		50%	10950	0.643
1c		100%	14600	0.61
1d		130%	16790	0.599
2a	RW	2%	1530	0.677
2b		4%	1560	0.654
2c		6%	1590	0.63
2d		8%	1620	0.608
3a	Ge/Si ratio	10%	0.55	0.74
3b		20%	0.6	0.78
3c		30%	0.65	0.82
3d		40%	0.7	0.86

Table 5.5 Li model experiment scenarios. From left to right, column 1 is ID for different model experiments, Scenario 1 corresponds to river flux increase. Scenario 2 increases reverse weathering flux and Scenario 3 increases weathering intensity (δ^7Li of river). From a to d, the extent of changing increases from small to large. Column 2 tells which variable is changing in the scenario. Column 3 tells how much the variable in column 2 changes. Column 4 is the Li flux or δ^7Li used in the corresponding scenario. Column 5 is the δ^7Li of ocean at steady state for each scenario.

scenario	variable	% increase	flux or ratio	result
1a	Friver	20%	9.60E+09	24.83
1b		50%	1.20E+10	24.59
1c		100%	1.60E+10	24.25
1d		130%	1.84E+10	24.1
2a	RW	2%	8.16E+09	25.09
2b		4%	8.32E+09	25.16
2c		6%	8.48E+09	25.22
2d		8%	8.64E+09	25.29
3a	δ^7Li	10%	5.13	24.85
3b		20%	4.56	24.68
3c		30%	3.99	24.51
3d		40%	3.42	24.34

Summary of changes that could explain seawater Ge/Si ratio and δ^7Li record

Reproducing the Ge/Si ratio and δ^7Li record during the Mid-Miocene period requires interaction of river flux, reverse weathering flux and changes in isotopic composition of river flux. The MMCO is a relatively wet and warm period, and weathering intensity is believed to increase under these circumstances, leading to Ge/Si ratio increase and δ^7Li decrease of seawater. δ^7Li decreased ~ 1‰ from 17 -14.5Ma in data from Misra and Froelich (2012). In our model test, scenario 3(c) implies that 30% isotopic composition change results in 0.49‰ decrease of δ^7Li and 0.12 increase of Ge/Si ratio. However, a Ge/Si increase is not observed in this study around 15 Ma. This result might suggest that a weathering intensity increase alone cannot produce the record we

observed. However, the scatter in the record makes it difficult to resolve whether the Ge/Si of seawater changes in this interval. A river flux increase will decrease Ge/Si ratio and δ^7Li of seawater. Scenario 1(b), a 50% increase of river flux can cause 0.41‰ decrease in δ^7Li and 0.06 decrease in Ge/Si ratio. This scenario combined with scenario 3(d) can produce a 1‰ reduction in δ^7Li but only balance 0.06 of 0.16 Ge/Si increase. In scenario 1(c), a 100% increase in river flux can cause 0.75‰ decrease in δ^7Li and 0.09 decrease in Ge/Si ratio. The 100% increase in river flux is an extreme setting, even this cannot fully compensate for the increase of Ge/Si ratio from scenario 3(c). The combination of increased weathering flux and increased weathering intensity cannot achieve the mild increase of the Ge/Si ratio we observed in MMCO compared to present.Because seawater Ge/Si ratio is very sensitive to changes in weathering intensity, the weathering flux needs to double to offset the effect of a 30% weathering intensity increase. Doubling the river flux of silica is unexpected, suggesting the reverse weathering flux also changes in the mid-Miocene. A slight reverse weathering increase has a strong effect of reducing the Ge/Si ratio while increasing δ^7Li moderately. When adjusting parameters to the scenario 1(b), 2(c) and 3(c), that is 50% increase in river flux, 6% increase in reverse weathering flux and 30% increase in weathering intensity, the Ge/Si ratio is 0.72 μmol/mol, and the δ^7Li is 23.7‰. Other combinations can generate similar results, scenario 1(b), 2(b) and 3(b) yields Ge/Si ratio of 0.697 and δ^7Li of 23.9‰. Scenario 1(a), 2(a) and 3(b) yields Ge/Si ratio of 0.73 and δ^7Li of 24.3‰. Other parameters that are not listed in test results can also make this model work and generate data similar to Ge/Si ratio and δ^7Li record.

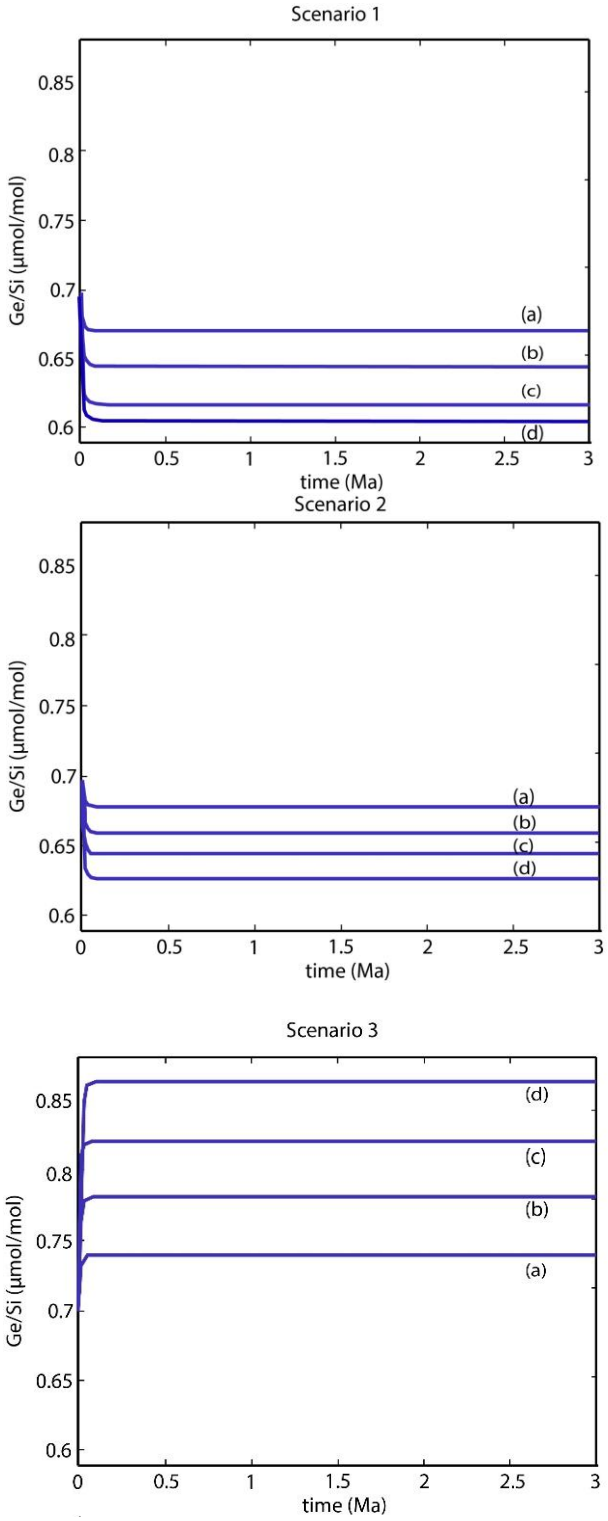

Figure 5.10 Ge/Si box model simulation results. Scenario 1 corresponds to river flux increase, Scenario 2 corresponds to reverse weathering flux increase and Scenario 3 corresponds to weathering intensity increase (Ge/Si ratio of river increase). From (a) to (d), the extent of changing increases

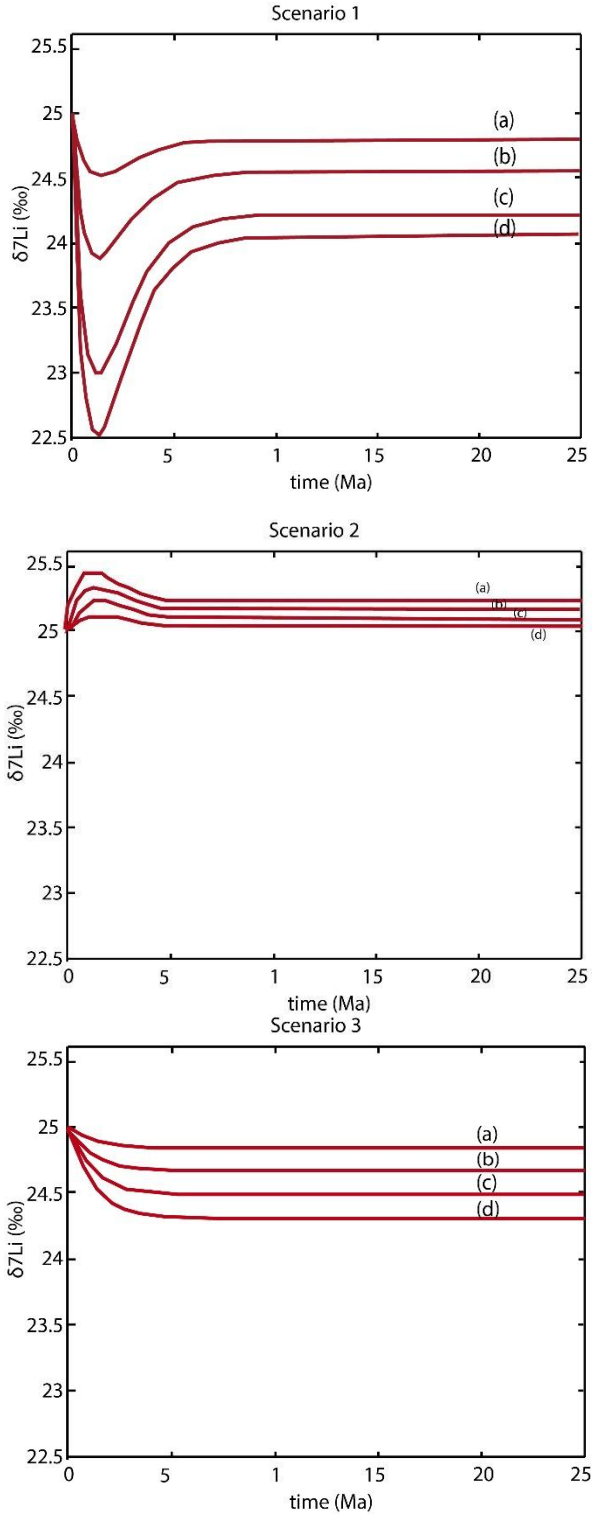

Figure 5.11 Li box model simulation results. Scenario 1 corresponds to river flux increase, Scenario 2 corresponds to reverse weathering flux increase and Scenario 3 corresponds to weathering intensity increase (δ^7Li of river decrease). From (a) to (d), the extent of changing increases

CHAPTER 6

MODEL DISCUSSION

Considering the MMCO background, proxy records and model simulation, we believe the slightly decreasing Ge/Si ratio and δ^7Li during the MMCO result sfrom: (1) higher weathering intensity; (2) increasing river flux F_{river} and (3) increasing reverse weathering flux F_{rw}. High weathering intensity is consistent with the warm and wet climate condition during MMCO. The total continental flux delivered to the sea by river increases as well. Reverse weathering responds to the increasing input to the ocean reservoir and adjusts to reach a new steady state. The key question is how "intense" the weathering was and how much the river flux increased in MMCO.

Changes in Ge/Si ratio of river flux

The isotopic composition of river flux directly reflects the ratio of primary mineral to secondary mineral dissolved in streams, as a result, weathering intensity can also be inferred from variations of isotopic composition. The present river Ge/Si ratio and δ^7Li are lower than seawater isotopic composition. Thus, when Ge/Si ratio of river increases, seawater Ge/Si ratio increases as well. The present river Ge/Si ratio displays an average value of ~0.56 μmol/mol (Froelich et al., 1992), and the bedrock Ge/Si ratio varies from 1 to 3 μmol/mol. Since the river Ge/Si ratio is derived from the mixture of dissolved

primary minerals and secondary clays, we express the relationship between bedrock, river, secondary clays and weathering intensity as this equation developed by Murnane and Stallard (1990):

6.1) $Ge/Si_{bedrock} = W \cdot Ge/Si_{river} + Ge/Si_{sec}(1 - W)$

We assume a simple linear relationship between W and Ge/Si_{sec}, with the intercept of $Ge/Si_{bedrock}$ at W=0. The slope of the line is an empirical partitioning factor that can be calculated from data:

6.2) $Ge/Si_{sec} = Ge/Si_{bedrock} + AW$

Substituting equation (6.1) with equation (6.2):

6.3) $Ge/Si_{river} = Ge/Si_{bedrock} + A(W - 1)$

6.4) $W = \frac{Ge/Si_{river} - Ge/Si_{bedrock}}{A} + 1$

where A is an empirical Ge partitioning factor, the slope of the linear relationship between W and Ge/Si_{sec}. W is weathering intensity, the fraction of Si released to stream from bedrock by chemical weathering. When W=1, the weathering is congruent and $Ge/Si_{river}=Ge/Si_{bedrock}$. When W approaches 0, most Ge is sequestered into secondary clays, and $Ge/Si_{river}=Ge/Si_{bedrock}$ - A. If we assume $Ge/Si_{bedrock}$=1.5, Ge/Si_{river} can be as low as 0.3, so when W=0, A=1.2. At steady state Ge/Si_{river}=0.5 μmol/mol, W is calculated to be 0.16. In our scenario 3 group, the weathering intensity is listed in Table 6.1. The relationship of how Ge/Si_{riv} changes with weathering intensity is shown in Figure 6.1.

Table 6.1 Weathering intensity calculated for Scenario3

Scenario	Ge/Si_{river}	W
3 (a)	0.55	0.21
3 (b)	0.6	0.25
3 (c)	0.65	0.29
3 (d)	0.7	0.33

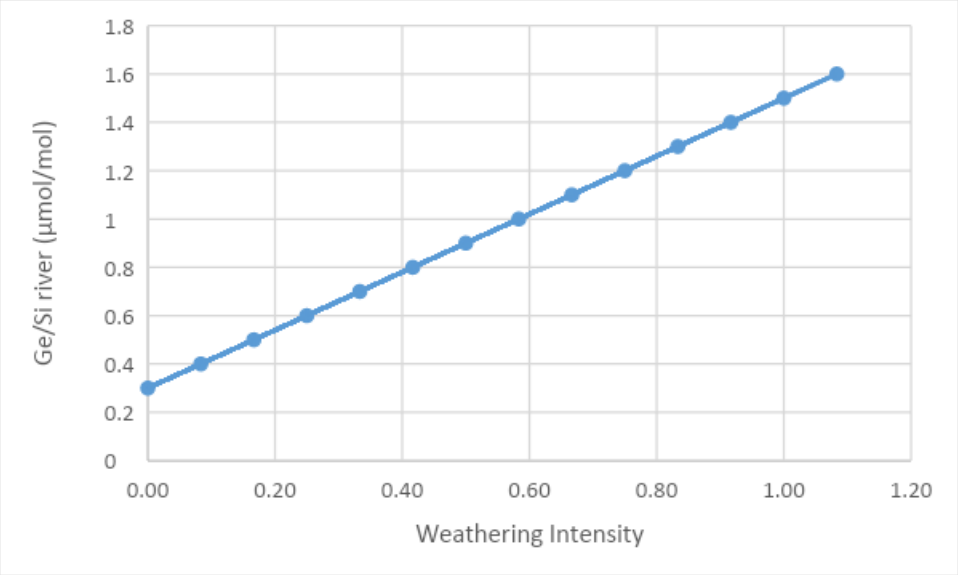

Figure 6.1 Ge/Si ratio of river and weathering intensity curve

For scenario 3(d), Ge/Si_{river} is close to the present seawater Ge/Si ratio, so to balance the impact from enhanced weathering intensity, it requires F_{river} to increase to 2.7 times of present value and 14% increase in reverse weathering. Such high F_{river} is very unusual, we do not think it realistic during MMCO. In our model cases, most results include scenario 3(b) and 3(c), which indicates *W* is probably lower than 0.3.

As for Li isotopes, the δ^7Li of river for present is 23‰, and the estimate of river δ^7Li at 60 Ma ago is 3‰, we select a value that is in between, fits the record well and can achieve a pseudo steady state when ocean δ^7Li is 25‰. However, the actual δ^7Li of rivers at 25 Ma and how it changes with time is not clear. This adds uncertainty to our model and affects the model results.

Effect of river flux

The river flux reflects how much dissolved Si and Li is transported by river to the ocean, and the effect of river flux variation depends on its isotopic composition. The Ge/Si ratio of rivers is always lower than seawater Ge/Si ratio, so increasing river flux will lower Ge/Si ratio of seawater. The effect of river flux for Li is more complicated, it depends on the relationship with δ^7Li of hydrothermal input. When $\delta^7Li_{river}<\delta^7Li_{HT}$, the increasing river flux will reduce δ^7Li of seawater. When $\delta^7Li_{river}>\delta^7Li_{HT}$, the increasing river flux will raise δ^7Li of seawater. In our model, δ^7Li_{river} is set to be 5.7‰, lower than δ^7Li_{HT} 8.3‰. With higher weathering intensity, δ^7Li_{river} decreases to even lower value, so greater river flux also decreases δ^7Li of seawater.

Effect of authigenesis

Authigenesis is an important sink for both Ge and Li. It sequesters Ge, removes isotopically light Li and some Si. The intensification of this process will lower the Ge/Si ratio and increase δ^7Li of seawater. However, the fractionation factor of this process is uncertain. In our Li model, we use model parameters from Misra and Froelich (2012), who proposed that the MAAC sink and AOC sink have the same fractionation factor of 16‰. This might not be always the case. In the model developed by Li and West (2014), MAAC sink has different fractionation factor from AOC sink. Their model tests suggest that fractionation into MAAC should be greater than AOC, and there was a sink shift from AOC to MAAC in the past 60Ma (Li and West, 2014). The magnitude of authigenesis flux is proportional to the mass of Li in the ocean in our model, and it is likely that the proportion of MAAC to AOC varied during MMCO. The mechanism that controls the fractionation factor is not known. If the proportion of MAAC and AOC changed during MMCO, it would affect isotopic composition of seawater.

Other factors that affect seawater isotopic composition

Temperature is a vital factor that many processes are dependent on. Temperature can affect dissolution of biogenic opal and other minerals, and can also have an impact on the scale of reverse weathering. For example, if seawater temperature increased, more biogenic opal is dissolved during sinking, and less reaches the seafloor, thus less Ge

may be available to be sequestered into secondary clays. Under this scenario more Ge exists in seawater and the Ge/Si ratio of seawater will be elevated. Temperature is likely to influence the fractionation factor of other processes.

Moreover, so far we mainly talked about the geochemical side of Ge/Si ratio evolution, the biological side is not considered. The knowledge we have of how the abundance of siliceous organisms has varied in time is limited, and diatoms and sponges are not the only species that uptake Si in the ocean. Evidence shows that some smaller organisms also take up Si. The abundance of other siliceous organisms is not known, so we cannot evaluate the effect from other species on seawater Ge/Si ratio.

CHAPTER 7

CONCLUSION

Based on indicators from $\delta^{18}O$, alkenones, boron isotopes, pCO_2 and pH reconstructions, the climate during the MMCO was relatively warm and seawater was more acidic than at present. Weathering proxies like $^{87}Sr/^{86}Sr$, $^{187}Os/^{186}Os$ and $\delta^{7}Li$ suggests that weathering intensity was high during mid-Miocene. In this study, Ge/Si ratios of 81 samples from ODP U1337A were analyzed. The data show a wide range from Ge/Si = 0.45 to 1.04 umol/mol. There is no clear temporal trend in Ge/Si data from the diatoms at this site. There is some evidence of a circa 1.9-Maperiod in the Ge/Si data, but the statistical significance of this periodic component is low. Comparing our Ge/Si data with the data from Shemesh et al. (1989) during 11-13.9 Ma, our data average ~0.76 μmol/mol, similar to Shemesh's data within uncertainty. Before 13.9 Ma, our data is ~0.72 μmol/mol, lower than Shemesh's data by 0.2 μmol/mol. Filtering the data by removing samples with Ge/Si < 0.6 μmol/mol generates a mean of Ge/Si ratio for 0.78± 0.02 μmol/mol, consistent with the results from Shemesh et al (1989). Overall, the Ge/Si ratio in MMCO is still higher than modern seawater ~0.7. Model experiments combining Ge/Si and Li isotopes make it possible to test effects of varying weathering flux, weathering intensity and removal flux during MMCO. The model was built using modern Si and Li budgets with their present Ge/Si ratio and isotopic composition. The effect of river flux, weathering intensity and reverse weathering flux on seawater Ge/Si and $\delta^{7}Li$ are observed in model runs:

(1) Increasing river flux reduces seawater Ge/Si ratio in all cases and δ^7Li when $\delta^7Li_{riv} < \delta^7Li_{HT}$

(2) Increasing weathering intensity increases Ge/Si ratio and reduces seawater δ^7Li

(3) Increasing reverse weathering flux decreases Ge/Si ratio and increases seawater δ^7Li

Model simulation results indicate that the combination of increasing river flux, reverse weathering flux and weathering intensity can replicate the Ge/Si and δ^7Li record. However, the effect of variations in the river flux is very weak, which can be compensated by small increasing in reverse weathering.

The high Ge/Si ratio and slightly low δ^7Li during the MMCO suggests high weathering intensity, high reverse weathering flux, and a weathering flux of silica that was at approximately the same level during MMCO compared to the present.

APPENDIX

Table A1 Ge/Si ratio of U1337A

Sample ID	depth	age	Ge/Si	Ge/Si corrected
25-1S	245.08	11.3219	0.7347	0.7941
25-2S	246.78	11.3839	0.7467	0.8075
25-4S	249.6	11.4869	0.7796	0.8440
25-5S	251.09	11.5415	0.7424	0.8027
25-6S	252.58	11.5961	0.7561	0.8179
25-7S	253.6	11.6336	0.7514	0.8126
26-1S	254	11.6483	0.7639	0.8265
26-2S	255.9	11.7183	0.6219	0.6687
26-3S	257.4	11.7737	0.6403	0.6892
26-4S	258.9	11.8292	0.6137	0.6597
26-5S	260.44	11.8863	0.7052	0.7613
26-6S	261.9	11.9405	0.5564	0.5959
26-7S	262.9	11.9777	0.5292	0.5658
27-1S	266.96	12.1294	0.8964	0.9738
28-1S	272.61	12.3421	0.8881	0.9646
28-2S	274.12	12.3993	0.7312	0.7902
28-3S	275.63	12.4566	0.6896	0.7440
28-4S	276.62	12.4942	0.4574	0.4860
29-1S	284.9	12.8119	0.5120	0.5467
29-2S	286.42	12.8708	0.5992	0.6436
29-3S	287.94	12.9298	0.5402	0.5780
29-4S	289.44	12.9883	0.5402	0.5780
29-5S	290.94	13.0469	0.9015	0.9794
29-7S	293.41	13.1437	0.6193	0.6659
30-1S	300.42	13.4214	0.6460	0.6955
30-2S	301.89	13.4801	0.9252	1.0058
30-3S	303.41	13.5411	0.7790	0.8433
30-4S	304.9	13.6010	0.7677	0.8308
30-5S	306.42	13.6624	0.7717	0.8352
30-6S	307.88	13.7215	0.9047	0.9830
30-7S	309.39	13.7828	0.8374	0.9082
31-3S	313.2	13.9385	0.8227	0.8919
31-4S	314.68	13.9994	0.4654	0.4948
31-5S	316.18	14.0613	0.7030	0.7588
31-6S	317.68	14.1234	0.5814	0.6238
32-1S	319.475	14.1980	0.5717	0.6130

32-2S	321.27	14.2729	0.6602	0.7113
32-5S	325.81	14.4638	0.7428	0.8032
33-2S	329.98	14.6410	0.6622	0.7136
33-4S	333	14.7705	0.6363	0.6847
33-5S	334.5	14.8351	0.6579	0.7088
33-6S	335.98	14.8992	0.5773	0.6192
34-1S	339.36	15.0463	0.7261	0.7845
34-2S	340.85	15.1115	0.5143	0.5492
34-3S	342.35	15.1774	0.6311	0.6790
34-4S	343.85	15.2436	0.5704	0.6116
34-5S	345.35	15.3100	0.7422	0.8024
34-6S	346.89	15.3785	0.5924	0.6360
35-1S	348.33	15.4427	0.7287	0.7874
35-2S	349.83	15.5099	0.7211	0.7789
35-3S	351.33	15.5773	0.7610	0.8233
35-4S	352.83	15.6450	0.7372	0.7969
35-5S	354.33	15.7129	0.7340	0.7933
35-6S	355.83	15.7811	0.8144	0.8826
36-2S	360.25	15.9836	0.6894	0.7437
36-3S	361.76	16.0533	0.5412	0.5791
36-4S	363.25	16.1224	0.7839	0.8487
36-5S	364.74	16.1917	0.4817	0.5130
36-6S	366.25	16.2622	0.4236	0.4484
36-7S	367.65	16.3278	0.7197	0.7774
37-1S	368.86	16.3847	0.6144	0.6605
37-2S	370.37	16.4560	0.6477	0.6974
37-3S	371.86	16.5266	0.6031	0.6479
37-4S	373.35	16.5974	0.7049	0.7610
37-5S	374.89	16.6709	0.5746	0.6162
37-6S	376.34	16.7404	0.6267	0.6741
37-7S	377.36	16.7895	0.7854	0.8504
38-1S	379.01	16.8691	0.6871	0.7412
38-2S	380.5	16.9412	0.5375	0.5750
38-3S	382.05	17.0166	0.7796	0.8441
38-4S	382.99	17.0624	0.6877	0.7419
39-1S	388.05	17.3112	0.7133	0.7703
39-2S	389.54	17.3850	0.6345	0.6827
39-3S	391.03	17.4591	0.7774	0.8416
39-4S	392.55	17.5351	0.7762	0.8402
39-5S	394.03	17.6093	0.8679	0.9421
40-2S	401.34	17.9799	0.5145	0.5494
40-3S	402.87	18.0583	0.4400	0.4667

40-4S	404.3	18.1319	0.5568	0.5965
40-5S	405.9	18.2145	0.6889	0.7432
40-6S	407.4	18.2923	0.9547	1.0386

Table A2 5pt running mean of Ge/Si U1337A

Sample ID	depth	age	Ge/Si 5 point average
1	249.026	11.47	0.813
2	255.96	11.72	0.731
3	264.962	12.05	0.772
4	279.538	12.61	0.642
5	292.43	13.11	0.699
6	304.9	13.60	0.900
7	314.226	13.98	0.736
8	325.907	14.47	0.705
9	338.608	15.01	0.668
10	346.85	15.38	0.723
11	354.914	15.74	0.808
12	364.73	16.19	0.633
13	371.866	16.53	0.677
14	379.052	16.87	0.737
15	388.832	17.35	0.775
16	401.688	18.00	0.660

Table A3 3pt running mean of Ge/Si U1337A

Sample ID	depth	age	Ge/Si 3point average
1	247.153	11.397	0.815
2	252.423	11.590	0.811
3	255.767	11.713	0.728
4	260.413	11.885	0.672
5	267.490	12.149	0.835
6	275.457	12.450	0.673
7	286.420	12.871	0.589
8	291.263	13.060	0.741
9	301.907	13.481	0.848
10	306.400	13.662	0.883

11	312.423	13.907	0.765
12	317.778	14.127	0.665
13	325.687	14.459	0.743
14	334.493	14.835	0.671
15	340.853	15.112	0.671
16	345.363	15.311	0.683
17	349.830	15.510	0.797
18	354.330	15.713	0.824
19	361.753	16.053	0.724
20	366.213	16.260	0.580
21	370.363	16.456	0.669
22	374.860	16.670	0.684
23	378.957	16.866	0.722
24	384.363	17.130	0.785
25	391.040	17.460	0.788
26	399.413	17.882	0.653
27	405.867	18.213	0.793

Table A4 Sponge fraction estimate (Unit: pixels)

sample	sponge	diatom	fraction
60-1	15286	129616	10.5%
60-2	5345	66584	7.4%
303-1	5257	39879	11.6%
303-2	2605	31029	7.7%
303-3	2985	31055	8.8%
mean	6295.6	59632.6	9.5%

REFERENCES

Aguirre, Arnulfo A., Louis A. Derry, Taylor J. Mills, and Suzanne P. Anderson. "Colloidal Transport in the Gordon Gulch Catchment of the Boulder Creek CZO and Its Effect on C-Q Relationships for Silicon: COLLOIDS AND C-Q RELATIONSHIPS FOR Si." *Water Resources Research* 53, no. 3 (March 2017): 2368–83. https://doi.org/10.1002/2016WR019730.

Armstrong McKay, David I., Toby Tyrrell, Paul A. Wilson, and Gavin L. Foster. "Estimating the Impact of the Cryptic Degassing of Large Igneous Provinces: A Mid-Miocene Case-Study." *Earth and Planetary Science Letters* 403 (October 2014): 254–62. https://doi.org/10.1016/j.epsl.2014.06.040.

Auer, Gerald, Werner E. Piller, Markus Reuter, and Mathias Harzhauser. "Correlating Carbon and Oxygen Isotope Events in Early to Middle Miocene Shallow Marine Carbonates in the Mediterranean Region Using Orbitally Tuned Chemostratigraphy and Lithostratigraphy." *Paleoceanography* 30, no. 4 (April 2015): 332–52. https://doi.org/10.1002/2014PA002716.

Azam, Farooq, and Benjamin E. Volcani. "Role of Silicon in Diatom Metabolism." *Archives of Microbiology* 101, no. 1 (January 1, 1974): 1–8. https://doi.org/10.1007/BF00455920.

Baker, A.R., T.D. Jickells, M. Witt, and K.L. Linge. "Trends in the Solubility of Iron, Aluminium, Manganese and Phosphorus in Aerosol Collected over the Atlantic Ocean." *Marine Chemistry* 98, no. 1 (January 2006): 43–58. https://doi.org/10.1016/j.marchem.2005.06.004.

Baronas, J. Jotautas, Douglas E. Hammond, James McManus, C. Geoffrey Wheat, and Christopher Siebert. "A Global Ge Isotope Budget." *Geochimica et Cosmochimica Acta* 203 (April 2017): 265–83. https://doi.org/10.1016/j.gca.2017.01.008.

Barry, T.L., S. Self, S.P. Kelley, S. Reidel, P. Hooper, and M. Widdowson. "New 40Ar/39Ar Dating of the Grande Ronde Lavas, Columbia River Basalts, USA: Implications for Duration of Flood Basalt Eruption Episodes." *Lithos* 118, no. 3–4 (August 2010): 213–22. https://doi.org/10.1016/j.lithos.2010.03.014.

Badaut D. and Risacher F. “Authigenic smectite on diatom frustules in Bolivian saline lakes.” *Geochim. Cosmochim. Acta* **47** (1982), 363–375.

Blanc, P.L., D. Rabussier, C. Vergnaud-Grazzini, and J.C. Duplessy, “North Atlantic Deep Water Formed by the Later Middle Miocene.” Nature (1980), 289, 553-555.

Campbell, Siobhan M., Robert Moucha, Louis A. Derry, and Maureen E. Raymo. “Effects of Dynamic Topography on the Cenozoic Carbonate Compensation Depth.” *Geochemistry, Geophysics, Geosystems* 19, no. 4 (April 2018): 1025–34. https://doi.org/10.1002/2017GC007386.

Clarke, Jonathan. “The Occurrence and Significance of Biogenic Opal in the Regolith.” *Earth-Science Reviews* 60, no. 3 (February 1, 2003): 175–94. https://doi.org/10.1016/S0012-8252(02)00092-2.

Clift, Peter D., Shiming Wan, and Jerzy Blusztajn. “Reconstructing Chemical Weathering, Physical Erosion and Monsoon Intensity since 25Ma in the Northern South China Sea: A Review of Competing Proxies.” *Earth-Science Reviews* 130 (March 2014): 86–102. https://doi.org/10.1016/j.earscirev.2014.01.002.

Cole T. G. “Composition, oxygen isotope geochemistry, and origin of smectite in the metalliferous sediments of the Bauer Deep, Southeast Pacific.” *Geochim. Cosmochim. Acta* **49** (1985), 221–235.

Conley, Daniel J. “Terrestrial Ecosystems and the Global Biogeochemical Silica Cycle: GLOBAL BIOGEOCHEMICAL SILICA CYCLE.” *Global Biogeochemical Cycles* 16, no. 4 (December 2002): 68-1-68–8. https://doi.org/10.1029/2002GB001894.

Criss, R. E. Principles of Stable Isotope Distribution (1999). New York, Oxford: Oxford University Press

Davis, Klarissa N., John A. Wolff, Michael C. Rowe, and Owen K. Neill. “Sulfur Release from Main-Phase Columbia River Basalt Eruptions.” *Geology* 45, no. 11 (November 1, 2017): 1043–46. https://doi.org/10.1130/G39371.1.

Derry, Louis A., and Christian France-Lanord. “Neogene Growth of the Sedimentary

Organic Carbon Reservoir." *Paleoceanography* 11, no. 3 (June 1996): 267–75. https://doi.org/10.1029/95PA03839.

Diester-Haass, Liselotte, Katharina Billups, Darren R. Gröcke, Louis François, Vincent Lefebvre, and Kay C. Emeis. "Mid-Miocene Paleoproductivity in the Atlantic Ocean and Implications for the Global Carbon Cycle: MID-MIOCENE PALEOPRODUCTIVITY." *Paleoceanography* 24, no. 1 (March 2009): n/a-n/a. https://doi.org/10.1029/2008PA001605.

Dürr, H. H., M. Meybeck, J. Hartmann, G. G. Laruelle, and V. Roubeix. "Global Spatial Distribution of Natural Riverine Silica Inputs to the Coastal Zone." *Biogeosciences* 8, no. 3 (March 7, 2011): 597–620. https://doi.org/10.5194/bg-8-597-2011.

Elderfield, H., and A. Schultz. "Mid-Ocean Ridge Hydrothermal Fluxes and the Chemical Composition of the Ocean." *Annual Review of Earth and Planetary Sciences* 24, no. 1 (May 1996): 191–224. https://doi.org/10.1146/annurev.earth.24.1.191.

Ellwood, Michael J., Michelle Kelly, William A. Maher, and Patrick De Deckker. "Germanium Incorporation into Sponge Spicules: Development of a Proxy for Reconstructing Inorganic Germanium and Silicon Concentrations in Seawater." *Earth and Planetary Science Letters* 243, no. 3 (March 30, 2006): 749–59. https://doi.org/10.1016/j.epsl.2006.01.016.

Evans, Matthew J, and Louis A Derry. "Quartz Control of High Germanium/Silicon Ratios in Geothermal Waters," 2002, 4.

Farrell, John W, Steven C Clemens, and L Peter Gromet. "Improved Chronostratigraphic Reference Curve of Late Neogene Seawater 87Sr/86Sr," 1995, 4.

Föllmi, K. B., B. Gertsch, J.-P. Renevey, E. De Kaenel, and P. Stille. "Stratigraphy and Sedimentology of Phosphate-Rich Sediments in Malta and South-Eastern Sicily (Latest Oligocene to Early Late Miocene)." *Sedimentology* 55, no. 4 (2008): 1029–51. https://doi.org/10.1111/j.1365-3091.2007.00935.x.

Foster, Gavin L., Caroline H. Lear, and James W.B. Rae. "The Evolution of PCO2, Ice Volume and Climate during the Middle Miocene." *Earth and Planetary Science Letters* 341–344 (August 2012): 243–54.

https://doi.org/10.1016/j.epsl.2012.06.007.

Froelich, Flip. “Was the Late Paleocene-Early Eocene Hot Because Earth Was Flat? An Ocean Lithium Isotope View of Mountain Building, Continental Weathering, Carbon Dioxide, and Earth’s Cenozoic Clima.” *Oceanography* 27, no. 1 (March 1, 2014): 36–49. https://doi.org/10.5670/oceanog.2014.06.

Froelich, P. N., V. Blanc, R. A. Mortlock, S. N. Chillrud, W. Dunstan, A. Udomkit, and T.-H. Peng. “River Fluxes of Dissolved Silica to the Ocean Were Higher during Glacials: Ge/Si In Diatoms, Rivers, and Oceans.” *Paleoceanography* 7, no. 6 (December 1992): 739–67. https://doi.org/10.1029/92PA02090.

Gaillardet, J., B. Dupré, and C. J. Allègre. “Geochemistry of Large River Suspended Sediments: Silicate Weathering or Recycling Tracer?” *Geochimica et Cosmochimica Acta* 63, no. 23 (December 1, 1999): 4037–51. https://doi.org/10.1016/S0016-7037(99)00307-5.

Goldner, A., N. Herold, and M. Huber. “The Challenge of Simulating the Warmth of the Mid-Miocene Climatic Optimum in CESM1.” *Climate of the Past* 10, no. 2 (March 13, 2014): 523–36. https://doi.org/10.5194/cp-10-523-2014.

Goldschmidt, V. M., *Geochemistry*, Oxford University Press, New York, 1958

Greenop, Rosanna, Mathis P. Hain, Sindia M. Sosdian, Kevin I. C. Oliver, Philip Goodwin, Thomas B. Chalk, Caroline H. Lear, Paul A. Wilson, and Gavin L. Foster. “A Record of Neogene Seawater Reconstructed from Paired Analyses on Benthic and Planktic Foraminifera.” *Climate of the Past* 13, no. 2 (February 24, 2017): 149–70. https://doi.org/10.5194/cp-13-149-2017.

Hammond, Douglas E., James McManus, and William M. Berelson. “Oceanic Germanium/Silicon Ratios: Evaluation of the Potential Overprint of Temperature on Weathering Signals: OCEANIC GERMANIUM/SILICON RATIOS.” *Paleoceanography* 19, no. 2 (June 2004): n/a-n/a. https://doi.org/10.1029/2003PA000940.

Hammond, Douglas E., James McManus, William M. Berelson, Charlotte Meredith, Gary P. Klinkhammer, and Kenneth H. Coale. “Diagenetic Fractionation of Ge and Si in Reducing Sediments: The Missing Ge Sink and a Possible Mechanism to Cause Glacial/Interglacial Variations in Oceanic Ge/Si.” *Geochimica et Cosmochimica Acta* 64, no. 14 (July 2000): 2453–65.

https://doi.org/10.1016/S0016-7037(00)00362-8.

Harrison, Kevin G. “Role of Increased Marine Silica Input on Paleo-PCO2 Levels.” *Paleoceanography* 15, no. 3 (2000): 292–98. https://doi.org/10.1029/1999PA000427.

Hein J. R., Yeh H-W., and Alexander E. Origin of iron-rich montmorillonite from the manganese nodule belt of the North Equatorial Pacific. *Clays and Clay Minerals* **27** (1979)**,** 185–194.

Hess, J., M. L. Bender, and J.-G. Schilling. “Evolution of the Ratio of Strontium-87 to Strontium-86 in Seawater from Cretaceous to Present.” *Science* 231, no. 4741 (February 28, 1986): 979–84. https://doi.org/10.1126/science.231.4741.979.

Hodell, David A., and Fay Woodruff. “Variations in the Strontium Isotopic Ratio of Seawater during the Miocene: Stratigraphic and Geochemical Implications.” *Paleoceanography* 9, no. 3 (June 1994): 405–26. https://doi.org/10.1029/94PA00292.

Holbourn, Ann, Wolfgang Kuhnt, Steven Clemens, Warren Prell, and Nils Andersen. “Middle to Late Miocene Stepwise Climate Cooling: Evidence from a High-Resolution Deep Water Isotope Curve Spanning 8 Million Years: MIOCENE BENTHIC ISOTOPES.” *Paleoceanography* 28, no. 4 (December 2013): 688–99. https://doi.org/10.1002/2013PA002538.

Holbourn, Ann, Wolfgang Kuhnt, Michael Schulz, José-Abel Flores, and Nils Andersen. “Orbitally-Paced Climate Evolution during the Middle Miocene ‘Monterey’ Carbon-Isotope Excursion.” *Earth and Planetary Science Letters* 261, no. 3–4 (September 2007): 534–50. https://doi.org/10.1016/j.epsl.2007.07.026.

Holland, H. D. “Sea Level, Sediments and the Composition of Seawater.” *American Journal of Science* 305, no. 3 (March 1, 2005): 220–39. https://doi.org/10.2475/ajs.305.3.220.

Hutchins, David A., and Kenneth W. Bruland. “Iron-Limited Diatom Growth and Si:N Uptake Ratios in a Coastal Upwelling Regime.” *Nature* 393, no. 6685 (June 1998): 561–64. https://doi.org/10.1038/31203.

Jeandel, Catherine, Bernhard Peucker-Ehrenbrink, Morgan T. Jones, Christopher R. Pearce, Eric H. Oelkers, Yves Godderis, François Lacan, Olivier Aumont, and Thomas Arsouze. "Ocean Margins: The Missing Term in Oceanic Element Budgets?" *Eos, Transactions American Geophysical Union* 92, no. 26 (June 28, 2011): 217. https://doi.org/10.1029/2011EO260001.

Kastner, M.J. "Diagenesis of Siliceous Oozes-4 Chemical Controls on the Rate of Opal-A to Opal-CT Transformation- an Experimental Study," n.d., 18.

Kender, Sev, Jimin Yu, and Victoria L. Peck. "Deep Ocean Carbonate Ion Increase during Mid Miocene CO2 Decline." *Scientific Reports* 4, no. 1 (May 2015). https://doi.org/10.1038/srep04187.

Kurtz, Andrew. "Ge/Si and Trace Element Studies of Silicate Weathering and Aerosol Deposition." (2000), PhD Thesis. Cornell Univiersity

Kurtz, Andrew C., Louis A. Derry, and Oliver A. Chadwick. "Germanium-Silicon Fractionation in the Weathering Environment." *Geochimica et Cosmochimica Acta* 66, no. 9 (May 2002): 1525–37. https://doi.org/10.1016/S0016-7037(01)00869-9.

Lacan, Francois, and Catherine Jeandel. "Neodymium Isotopes as a New Tool for Quantifying Exchange Fluxes at the Continent–Ocean Interface." *Earth and Planetary Science Letters* 232, no. 3–4 (April 2005): 245–57. https://doi.org/10.1016/j.epsl.2005.01.004.

Laruelle, G. G., V. Roubeix, A. Sferratore, B. Brodherr, D. Ciuffa, D. J. Conley, H. H. Dürr, et al. "Anthropogenic Perturbations of the Silicon Cycle at the Global Scale: Key Role of the Land-Ocean Transition: GLOBAL SI CYCLE." *Global Biogeochemical Cycles* 23, no. 4 (December 2009): n/a-n/a. https://doi.org/10.1029/2008GB003267.

Laskar, J., P. Robutel, F. Joutel, M. Gastineau, A. C. M. Correia, and B. Levrard. "A Long-Term Numerical Solution for the Insolation Quantities of the Earth." *Astronomy & Astrophysics* 428, no. 1 (December 1, 2004): 261–85. https://doi.org/10.1051/0004-6361:20041335.

Lear, Caroline H., Helen K. Coxall, Gavin L. Foster, Daniel J. Lunt, Elaine M. Mawbey, Yair Rosenthal, Sindia M. Sosdian, Ellen Thomas, and Paul A. Wilson. "Neogene Ice Volume and Ocean Temperatures: Insights from

Infaunal Foraminiferal Mg/Ca Paleothermometry: NEOGENE MG/CA PALEOTHERMOMETRY." *Paleoceanography* 30, no. 11 (November 2015): 1437–54. https://doi.org/10.1002/2015PA002833.

Lemarchand, D, J Gaillardet, É Lewin, and C. J Allègre. "Boron Isotope Systematics in Large Rivers: Implications for the Marine Boron Budget and Paleo-PH Reconstruction over the Cenozoic." *Chemical Geology*, Geochemistry of Crustal Fluids-Fluids in the Crust and Chemical Fluxes at the Earth's Surface, 190, no. 1 (October 30, 2002): 123–40. https://doi.org/10.1016/S0009-2541(02)00114-6.

Lugolobi, Festo, Andrew C. Kurtz, and Louis A. Derry. "Germanium–Silicon Fractionation in a Tropical, Granitic Weathering Environment." *Geochimica et Cosmochimica Acta* 74, no. 4 (February 15, 2010): 1294–1308. https://doi.org/10.1016/j.gca.2009.11.027.

Martin, J.-M., and M. Meybeck, Elemental mass balance of material carried by major world rivers, *Marine Chemistry*, 7, 173-206, 1979.

Maldonado, Manuel, Laura Navarro, Ana Grasa, Alicia Gonzalez, and Isabel Vaquerizo. "Silicon Uptake by Sponges: A Twist to Understanding Nutrient Cycling on Continental Margins." *Scientific Reports* 1, no. 1 (December 2011): 30. https://doi.org/10.1038/srep00030.

McManus, James, Douglas E. Hammond, Kathy Cummins, Gary P. Klinkhammer, and William M. Berelson. "Diagenetic Ge-Si Fractionation in Continental Margin Environments: Further Evidence for a Nonopal Ge Sink." *Geochimica et Cosmochimica Acta* 67, no. 23 (December 2003): 4545–57. https://doi.org/10.1016/S0016-7037(03)00385-5.

Michalopoulos, P., and R. C. Aller. "Rapid Clay Mineral Formation in Amazon Delta Sediments: Reverse Weathering and Oceanic Elemental Cycles." *Science* 270, no. 5236 (October 27, 1995): 614–17. https://doi.org/10.1126/science.270.5236.614.

Michalopoulos, Panagiotis, and Robert C Aller. "Early Diagenesis of Biogenic Silica in the Amazon Delta: Alteration, Authigenic Clay Formation, and Storage." *Geochimica et Cosmochimica Acta* 68, no. 5 (March 2004): 1061–85. https://doi.org/10.1016/j.gca.2003.07.018.

Miller, Kenneth G., Mark D. Feigenson, James D. Wright, and Bradford M. Clement. "Miocene Isotope Reference Section, Deep Sea Drilling Project Site 608: An Evaluation of Isotope and Biostratigraphic Resolution." *Paleoceanography* 6, no. 1 (February 1991): 33–52. https://doi.org/10.1029/90PA01941.

Miller, Kenneth G., James D. Wright, and Richard G. Fairbanks. "Unlocking the Ice House: Oligocene-Miocene Oxygen Isotopes, Eustasy, and Margin Erosion." *Journal of Geophysical Research: Solid Earth* 96, no. B4 (April 10, 1991): 6829–48. https://doi.org/10.1029/90JB02015.

Misra, S., and P. N. Froelich. "Lithium Isotope History of Cenozoic Seawater: Changes in Silicate Weathering and Reverse Weathering." *Science* 335, no. 6070 (February 17, 2012): 818–23. https://doi.org/10.1126/science.1214697.

Mortlock, Richard A., and Philip N. Froelich. "A Simple Method for the Rapid Determination of Biogenic Opal in Pelagic Marine Sediments." *Deep Sea Research Part A. Oceanographic Research Papers* 36, no. 9 (September 1989): 1415–26. https://doi.org/10.1016/0198-0149(89)90092-7.

Mortlock, Richard A., Philip N. Froelich, Richard A. Feely, Gary J. Massoth, David A. Butterfield, and John E. Lupton. "Silica and Germanium in Pacific Ocean Hydrothermal Vents and Plumes." *Earth and Planetary Science Letters* 119, no. 3 (September 1, 1993): 365–78. https://doi.org/10.1016/0012-821X(93)90144-X.

Mortlock, R. A., and P. N. Froelich, Determination of germanium by isotope dilution hydride generation inductively coupled plasma mass spectrometry, Anal. Chim. Acta, 332(2–3) (1996), 277–284, doi:10.1016/0003-2670(96)00230-9.

Mortlock, R. A., and Froelich, P. N. (1987). Continental weathering of germanium-Ge/Si in the global river discharge. *Geochim. Cosmochim*. Acta 51, 2075–2082. doi: 10.1016/0016-7037(87)90257-2

Murnane, Richard J., and Robert F. Stallard. "Germanium and Silicon in Rivers of the Orinoco Drainage Basin." *Nature* 344, no. 6268 (April 1990): 749. https://doi.org/10.1038/344749a0.

Mutti, Maria, André W. Droxler, and Andrew D. Cunningham. "Evolution of the Northern Nicaragua Rise during the Oligocene–Miocene: Drowning by Environmental Factors." *Sedimentary Geology,* Sedimentology in the 21st

Century - A Tribute to Wolfgang Schlager, 175, no. 1 (April 15, 2005): 237–58. https://doi.org/10.1016/j.sedgeo.2004.12.028.

Myrow, Paul M., Nigel C. Hughes, Louis A. Derry, N. Ryan McKenzie, Ganqing Jiang, A. Alexander G. Webb, Dhiraj M. Banerjee, Timothy S. Paulsen, and Birendra P. Singh. "Neogene Marine Isotopic Evolution and the Erosion of Lesser Himalayan Strata: Implications for Cenozoic Tectonic History." *Earth and Planetary Science Letters* 417 (May 2015): 142–50. https://doi.org/10.1016/j.epsl.2015.02.016.

Nelson, David M., Paul Tréguer, Mark A. Brzezinski, Aude Leynaert, and Bernard Quéguiner. "Production and Dissolution of Biogenic Silica in the Ocean: Revised Global Estimates, Comparison with Regional Data and Relationship to Biogenic Sedimentation." *Global Biogeochemical Cycles* 9, no. 3 (September 1995): 359–72. https://doi.org/10.1029/95GB01070.

Nesbitt, H. W., and G. M. Young. "Early Proterozoic Climates and Plate Motions Inferred from Major Element Chemistry of Lutites." *Nature* 299, no. 5885 (October 1982): 715. https://doi.org/10.1038/299715a0.

Odin G. S. and Frohlich F. Glaucony from the Kerguellen plateau (Southern Indian Ocean). In *Green Marine Clays* (1988) (ed. G. S.Odin), pp. 277–294. Elsevier, Amsterdam.

Oelkers EH, Gislason SR, Eiriksdottir ES, Jones M, Pearce CR, Jeandel C. "The Role of Riverine Particulate Material on the Global Cycles of the Elements." *Applied Geochemistry*. 26 (2011): 365–69. https://doi.org/10.1016/j.apgeochem.2011.03.062.

O'Neil, James R., and Hugh P. Taylor. "Oxygen Isotope Equilibrium between Muscovite and Water." *Journal of Geophysical Research (1896-1977)* 74, no. 25 (1969): 6012–22. https://doi.org/10.1029/JB074i025p06012.

Opfergelt, Sophie, and Pierre Delmelle. "Silicon Isotopes and Continental Weathering Processes: Assessing Controls on Si Transfer to the Ocean." *Comptes Rendus Geoscience* 344, no. 11–12 (November 2012): 723–38. https://doi.org/10.1016/j.crte.2012.09.006.

Oslick, Jeffrey S., Kenneth G. Miller, Mark D. Feigenson, and James D. Wright. "Oligocene-Miocene Strontium Isotopes: Stratigraphic Revisions and

Correlations to an Inferred Glacioeustatic Record." *Paleoceanography* 9, no. 3 (June 1994): 427–43. https://doi.org/10.1029/94PA00249.

Pagani, Mark, Michael A. Arthur, and Katherine H. Freeman. "Miocene Evolution of Atmospheric Carbon Dioxide." *Paleoceanography* 14, no. 3 (June 1999): 273–92. https://doi.org/10.1029/1999PA900006.

Paillard, D., L. Labeyrie, and P. Yiou, "Macintosh program performs time-series analysis", *Eos Trans, AGU* (1996), 77(39), 379, doi:10.1029/96EO00259.

Peucker-Ehrenbrink, B., and G. Ravizza. "The Marine Osmium Isotope Record." *Terra Nova* 12, no. 5 (2000): 205–19. https://doi.org/10.1046/j.1365-3121.2000.00295.x.

Rahman, S., R. C. Aller, and J. K. Cochran. "Cosmogenic ^{32} Si as a Tracer of Biogenic Silica Burial and Diagenesis: Major Deltaic Sinks in the Silica Cycle: Cosmogenic ^{32} Si Traces Biogenic Silica Burial." *Geophysical Research Letters* 43, no. 13 (July 16, 2016): 7124–32. https://doi.org/10.1002/2016GL069929.

Rahman, S., R. C. Aller, and J. K. Cochran. "The Missing Silica Sink: Revisiting the Marine Sedimentary Si Cycle Using Cosmogenic ^{32} Si: The Missing Sedimentary Silica Sink." *Global Biogeochemical Cycles* 31, no. 10 (October 2017): 1559–78. https://doi.org/10.1002/2017GB005746.

Rea, David K. "The Paleoclimatic Record Provided by Eolian Deposition in the Deep Sea: The Geologic History of Wind." *Reviews of Geophysics* 32, no. 2 (1994): 159. https://doi.org/10.1029/93RG03257.

Reusch, Douglas N, Greg Ravizza, Kirk A Maasch, and James D Wright. "Miocene Seawater 187Os/188Os Ratios Inferred from Metalliferous Carbonates." *Earth and Planetary Science Letters* 160, no. 1–2 (July 1998): 163–78. https://doi.org/10.1016/S0012-821X(98)00082-X.

Sayles F. L. and Bischoff. Ferromaganoan sediments in the equatorial east Pacific. *Earth and Planetary Science Letters* **19** (1973)**,** 330–336.

Shackleton, N.J., and J.P. Kenneff, "Paleotemperature history of the Cenozoic and the initiation of Antarctic glaciation: Oxygen and carbonisotope analyses in DSDP

sites 277, 279 and 281." *Initial Rep. Deep Sea Drilling Project* 29 (1975), 743-756.

Shemesh, A., R.A. Mortlock, R.J. Smith, and P.N. Froelich. "Determination of Ge/Si in Marine Siliceous Microfossils: Separation, Cleaning and Dissolution of Diatoms and Radiolaria." *Marine Chemistry* 25, no. 4 (December 1988): 305–23. https://doi.org/10.1016/0304-4203(88)90113-2.

Shemesh, A., R. A. Mortlock, and P. N. Froelich. "Late Cenozoic Ge/Si Record of Marine Biogenic Opal: Implications for Variations of Riverine Fluxes to the Ocean." *Paleoceanography* 4, no. 3 (June 1989): 221–34. https://doi.org/10.1029/PA004i003p00221.

Sosdian, S.M., R. Greenop, M.P. Hain, G.L. Foster, P.N. Pearson, and C.H. Lear. "Constraining the Evolution of Neogene Ocean Carbonate Chemistry Using the Boron Isotope PH Proxy." *Earth and Planetary Science Letters* 498 (September 2018): 362–76. https://doi.org/10.1016/j.epsl.2018.06.017.

Stallard, R. F., and J. M. Edmond. "Geochemistry of the Amazon: 3. Weathering Chemistry and Limits to Dissolved Inputs." *Journal of Geophysical Research* 92, no. C8 (1987): 8293. https://doi.org/10.1029/JC092iC08p08293.

Struyf, Eric, and Daniel J. Conley. "Emerging Understanding of the Ecosystem Silica Filter." *Biogeochemistry* 107, no. 1–3 (February 2012): 9–18. https://doi.org/10.1007/s10533-011-9590-2.

Struyf, Eric, and Daniel J. Conley. "Silica: An Essential Nutrient in Wetland Biogeochemistry." *Frontiers in Ecology and the Environment* 7, no. 2 (2009): 88–94. https://doi.org/10.1890/070126.

Super, James R., Ellen Thomas, Mark Pagani, Matthew Huber, Charlotte O'Brien, and Pincelli M. Hull. "North Atlantic Temperature and PCO2 Coupling in the Early-Middle Miocene." *Geology* 46, no. 6 (June 1, 2018): 519–22. https://doi.org/10.1130/G40228.1.

Sutton, Jill, Michael J. Ellwood, William A. Maher, and Peter L. Croot. "Oceanic Distribution of Inorganic Germanium Relative to Silicon: Germanium Discrimination by Diatoms." *Global Biogeochemical Cycles* 24, no. 2 (2010). https://doi.org/10.1029/2009GB003689.

Sutton, Jill N., Luc André, Damien Cardinal, Daniel J. Conley, Gregory F. de Souza, Jonathan Dean, Justin Dodd, et al. "A Review of the Stable Isotope Bio-Geochemistry of the Global Silicon Cycle and Its Associated Trace Elements." *Frontiers in Earth Science* 5 (January 30, 2018). https://doi.org/10.3389/feart.2017.00112.

Takahashi, K. 1981. *Vertical flux, ecology and dissolution of Radiolaria in tropical oceans: implications for the silica cycle*. PhD thesis. Woods Hole Oceanographic Institution and Massachusetts Institute of Technology

Tatzel, Michael, Friedhelm von Blanckenburg, Marcus Oelze, Jan A. Schuessler, and Gerhard Bohrmann. "The Silicon Isotope Record of Early Silica Diagenesis." Earth and Planetary Science Letters 428 (October 15, 2015): 293–303. https://doi.org/10.1016/j.epsl.2015.07.018.

Tian, Jun, Wentao Ma, Mitchell W. Lyle, and Julia K. Shackford. "Synchronous Mid-Miocene Upper and Deep Oceanic Δ13C Changes in the East Equatorial Pacific Linked to Ocean Cooling and Ice Sheet Expansion." *Earth and Planetary Science Letters* 406 (November 2014): 72–80. https://doi.org/10.1016/j.epsl.2014.09.013.

Tréguer, Paul J., and Christina L. De La Rocha. "The World Ocean Silica Cycle." *Annual Review of Marine Science* 5, no. 1 (January 3, 2013): 477–501. https://doi.org/10.1146/annurev-marine-121211-172346.

Treguer P, Nelson DM, van Bennekom AJ, DeMaster DJ, Leynaert A, Queguiner B. 1995. The balance of silica in the world ocean: a re-estimate. *Science* 268:375–79

Van Bennekom A. J. and Van Der Gast S. J. Possible clay structures in frustules of living diatoms. *Geochim. Cosmochim. Acta* **40** (1976), 1149–1152.

Vincent, Edith, and Wolfgang H. Berger. "Carbon Dioxide and Polar Cooling in the Miocene: The Monterey Hypothesis." In *Geophysical Monograph Series*, edited by E.T. Sundquist and W.S. Broecker, 455–68. Washington, D. C.: American Geophysical Union, 2013. https://doi.org/10.1029/GM032p0455.

Wang, L., M. Sarnthein, J.-C. Duplessy, H. Erlenkeuser, S. Jung, and U. Pflaumann. "Paleo Sea Surface Salinities in the Low-Latitude Atlantic: The δ^{18}O Record of *Globigerinoides Ruber* (White)." *Paleoceanography* 10, no. 4 (August

1995): 749–61. https://doi.org/10.1029/95PA00577.

Warny, Sophie, Rosemary A. Askin, Michael J. Hannah, Barbara A.R. Mohr, J. Ian Raine, David M. Harwood, Fabio Florindo, and the SMS Science Team. "Palynomorphs from a Sediment Core Reveal a Sudden Remarkably Warm Antarctica during the Middle Miocene." *Geology* 37, no. 10 (October 1, 2009): 955–58. https://doi.org/10.1130/G30139A.1.

Wheat, C. Geoffrey, and James McManus. "The Potential Role of Ridge-Flank Hydrothermal Systems on Oceanic Germanium and Silicon Balances." *Geochimica et Cosmochimica Acta* 69, no. 8 (April 2005): 2021–29. https://doi.org/10.1016/j.gca.2004.05.046.

Wollast R, Mackenzie FT. 1983. Global cycle of silica. In *Silicon Geochemistry and Biogeochemistry*, ed. SR Aston, pp. 101–42. London: Academic

Woodruff, Fay, and Samuel Savin. "Mid-Miocene Isotope Stratigraphy in the Deep Sea: High-Resolution Correlations, Paleoclimatic Cycles, and Sediment Preservation." *Paleoceanography* 6, no. 6 (December 1991): 755–806. https://doi.org/10.1029/91PA02561.

You, Y., M. Huber, R. D. Müller, C. J. Poulsen, and J. Ribbe. "Simulation of the Middle Miocene Climate Optimum." *Geophysical Research Letters* 36, no. 4 (February 19, 2009). https://doi.org/10.1029/2008GL036571.

Zachos, J. "Trends, Rhythms, and Aberrations in Global Climate 65 Ma to Present." *Science* 292, no. 5517 (April 27, 2001): 686–93. https://doi.org/10.1126/science.1059412.

Zachos, James C., Gerald R. Dickens, and Richard E. Zeebe. "An Early Cenozoic Perspective on Greenhouse Warming and Carbon-Cycle Dynamics." *Nature* 451, no. 7176 (January 17, 2008): 279–83. https://doi.org/10.1038/nature06588.

Zhang, Y. G., M. Pagani, Z. Liu, S. M. Bohaty, and R. DeConto. "A 40-Million-Year History of Atmospheric CO2." *Philosophical Transactions of the Royal Society A: Mathematical, Physical and Engineering Sciences* 371, no. 2001 (September 16, 2013): 20130096–20130096. https://doi.org/10.1098/rsta.2013.0096.